Universität Potsdam
Institut für Physik und Astronomie

Masterarbeit | Master Thesis

Photometric and Spectroscopic Variability of White Dwarfs Showing Ultra-High Excitation Lines

Verfasser:	Semih Filiz
Studiengang:	Institut für Physik und Astronomie
Matrikelnummer:	800573
Erstgutachter:	Prof. Dr. Dr. Stephan Geier
Zweitgutachter:	Prof. Dr. Katja Poppenhäger
Direkter Vorgesetzter:	Dr. Nicole Reindl
Ort, Datum:	Potsdam; November 15, 2021

"I will find something to quote here."

Abstract

Context: A group of freshly born white dwarfs are distinguished with absorption lines of ultra-highly excited (UHE) metals (e.g. O VIII) in their optical spectra. This is an unprecedented phenomenon among astrophysical objects and a link to He II line problem white dwarfs is strongly indicated. The occurrence of such lines in these stars' spectra still awaits an explanation since their formation requires temperatures on the order of a million K. A recent study speculated that the presence of a wind-fed circumstellar magnetosphere can explain the existence of these features. It has been also established that the UHE as well as the He II line problem white dwarfs show a high variability rate and their observed period distribution, light curve amplitudes and shapes can be described with both reflection effect binaries and the magnetosphere model.

Aims & Methods: This work aims to explicate which scenario favors the observed photometric and spectroscopic properties of these perplexing objects. Therefore, the light curves of six UHE white dwarfs have been investigated. Furthermore, a search for changes in the EWs of the UHE and He II lines was performed for seven UHE white dwarfs. Finally, the spectra of 12 UHE and seven He II line problem white dwarfs were inspected for RV variations.

Results: The light curve analysis of the UHE white dwarfs reveals that the amplitudes observed in different bands agree with each other as reported previously. Moreover, the EW variations of the UHE lines that were detected in the spectra of UHE white dwarf J0146+3236 is validated. However, no EW variations could be detected in the other objects due to their insufficient S/N spectra. Finally, the spectra of investigated objects do not exhibit significant RV variations.

Conclusions: The consistency of measured photometric amplitudes in the different bands and the non-detection of RV variations in the sample implies that the photometric variability, most likely, does not transpire as a result of stellar type close binarity. The hypothesis of encountering substellar companions around UHE white dwarfs is regarded as very unlikely due to the lack of irradiation effect signatures along with the discrepancies observed in the occurrence rates of two samples. Thus, weak magnetic fields still remain as the most viable option to explain observed photometric variability.

Contents

1

Introduction

Our comprehension of the cosmos advances each day and undoubtedly humankind's affinity for stars played a major role in this progress. Emanating light from the stars has been dazzling humankind with its stunning view, and raising also plenty of questions since the ancient times. A great deal about the stars were shrouded by mist; how far they are away, what they are made of, how many of them exist... Modern astrophysics has made remarkable headway in the effort to shed light on these questions and the advancements guided us to the discovery of a particular type of star with an intriguing nature: **white dwarfs**.

First detections of white dwarfs coincide to the mid-19$^{\text{th}}$ Century when the stellar parallax has just been demonstrated. Fascinatingly, those two breakthroughs were made by the same astronomer, Friedrich Bessel. In 1844, Bessel detected inconsistencies in the proper motion of Sirius, which he associated with an invisible companion that is attracted gravitationally, though, as expected, he was oblivious of the fact that the unseen companion was a white dwarf. It was 1862 when the companion of Sirius was observed visually by coincidence for the first time. Alvan Graham Clark was testing an 18.5-inch lens and he detected the small and faint companion, though he was neither aware of the companion being a white dwarf nor Bessel's conclusions regarding the irregularities in the proper motion of Sirius occurring due to the companion (Wendell, 1898).

The interesting nature of the white dwarfs was not known until the early 20$^{\text{th}}$ Century and was only possible to be revealed with the progress in stellar spectroscopy. The first two objects of which spectra were taken were 40 Eridani B and Sirius B. Adams (1915) reported that spectra of Sirius A and Sirius B exhibit almost the same features, and also coined the term "white dwarf". Spectral similarity suggested similar temperatures for Sirius B and A, however Sirius B was several orders of magnitudes fainter, which could be only explained by Sirius B having a much smaller radius. Because of the binary nature, the mass of Sirus B had been already calculated as nearly 1 $M_{\odot}$. However, it was confusing because with the calculated mass and radius this indicated a much higher density for Sirius B than other stars which induced a lot of speculations.

Eddington (1924) suggested that gravitational redshift of Sirius B's spectrum can confirm the calculated high density. According to Eddington's calculations, with the given parameters of spectral type F0 indicating an effective temperature of 8000 K, an absolute magnitude of 11.3 mag, a radius of 19 600 km and assuming a mass of 0.85 $M_\odot$ from the calculated mass range 0.75 to 0.95 $M_\odot$ for Sirius B, the gravitational redshift in the spectrum was predicted as 20 km/s. One year after, the prediction was confirmed by Adams (1925) and thereafter, the progress made on white dwarf research increased substantially[1]. In 1926, Fowler stated that white dwarfs must consist of degenerate matter which was explained by the Pauli principle. In the 1930s, Chandrasekhar made a breakthrough with his work on the mass-radius relation of white dwarfs. In 1945, Schatzman revealed that gravitational settling is responsible for white dwarfs with single element spectra. In 1952, Mestel pointed out that the evolution of white dwarfs can be explained as a cooling process. Between 1958 and 1970, large proper motion surveys aided to locate white dwarfs (Eggen & Greenstein, 1965, 1967; Greenstein, 1966; Sandage & Luyten, 1967; Sandage, 1969). From that time forward, photometric and spectroscopic studies conducted by many astronomers contributed to have a better comprehension of white dwarfs (Strittmatter & Wickramasinghe, 1971; Bern & Wramdemark, 1973; Greenstein & Sargent, 1974; Sion & Liebert, 1977; Green, 1980; Liebert et al., 1988).

[1]Following information has been collected from Koester (2013)

2

Stellar Evolution

2.1 The Hertzsprung-Russell Diagram

Stars observed in the night sky are in different evolutionary stages with distinct properties. For that reason, the Hertzsprung-Russel diagram (HRD) remains as an essential tool in astronomical research to inspect stellar evolution, which distributes stars according to their stellar spectral type (or effective temperature, hence colour) and luminosity (or absolute magnitude) (see Fig. 2.1). In the early 1900s, Ejnar Hertzsprung and Henry Norris Russell recognized the relation between color and the absolute magnitude of the stars. They identified that the stars clustered in distinct places on the diagram rather than being randomly distributed. Later, it was found out that the distribution of the stars in the HRD correspond to different evolutionary stages. Most of the stars reside on a strip, spanning the HRD from the bottom right corner to the upper left corner, called main sequence (MS). Additionally, other major groups consist of subgiants, giants, supergiants and white dwarfs. White dwarfs inhabit the bottom left corner of the HRD and when the first HRD was constructed (1910-1915) only 3 objects were placed in this region (Koester, 2013).

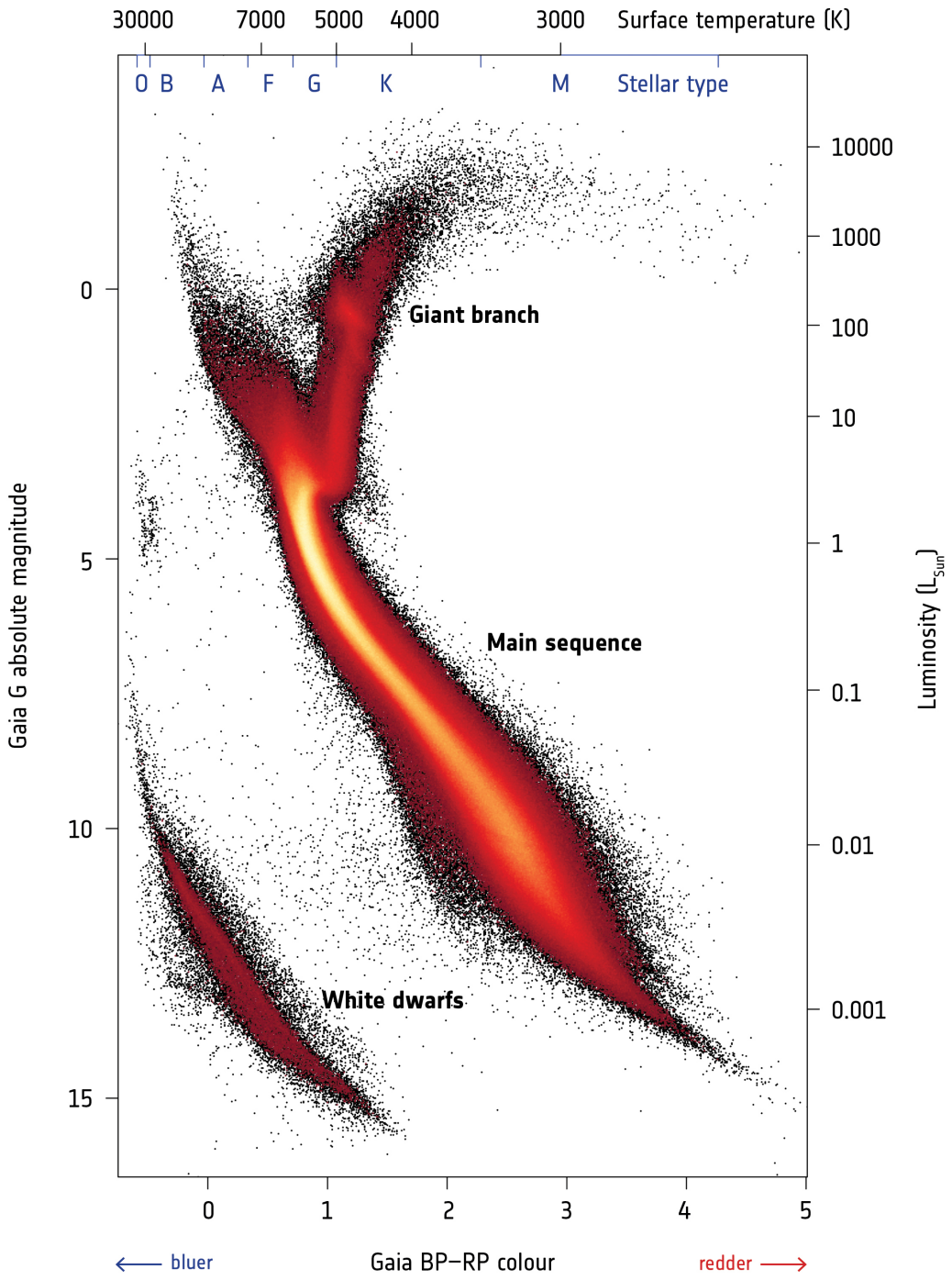

Figure 2.1: Observational Herztsprung-Russel Diagram constructed with the European Space Agency's (ESA) Gaia satellite mission. The vertical axis indicates absolute magnitude (or luminosity) and the horizontal axis indicates color (or temperature). As illustrated most of the stars lie on the main sequence. White dwarfs representing the final stage of stellar evolution reside on the bottom left corner. Copyright: ESA/Gaia/DPAC, CC BY-SA 3.0 IGO

2.2 Stellar Evolution of Low and Intermediate Mass Stars

Stars form in the stellar nurseries called molecular clouds. These low-temperature interstellar gas clouds have enough mass (10^3 - 10^6 $M_\odot$) to collapse under the influence of their own gravity, which leads to the formation of protostars. The central temperature of newly formed protostar is not high enough for hydrogen fusion and its energy source is gravitational energy. If the protostar can't accrete enough mass, it will become a brown dwarf, a failed star. Brown dwarfs are massive enough ($\sim$0.01 - 0.08 $M_\odot$) to support deuterium-burning for a short while.

If the protostar continues to accrete material from its surroundings, it contracts further. Once the mass ($\sim$ 0.08 $M_\odot$ H- burning limit), the central density and temperature of the protostar are high enough, it starts fusing hydrogen to helium and at this point the star enters to the zero age main sequence (ZAMS). As long as hydrogen burning continues in the core, the star is on the MS. How much time the star will spend on the MS depends on its initial mass and it can be estimated with

$$t_{MS} \approx 10^{10} \, (M_i[\mathrm{M}_\odot])^{-2} \, \text{years}, \tag{2.1}$$

which means that stars with higher initial masses spend less time on the MS than lower mass stars.

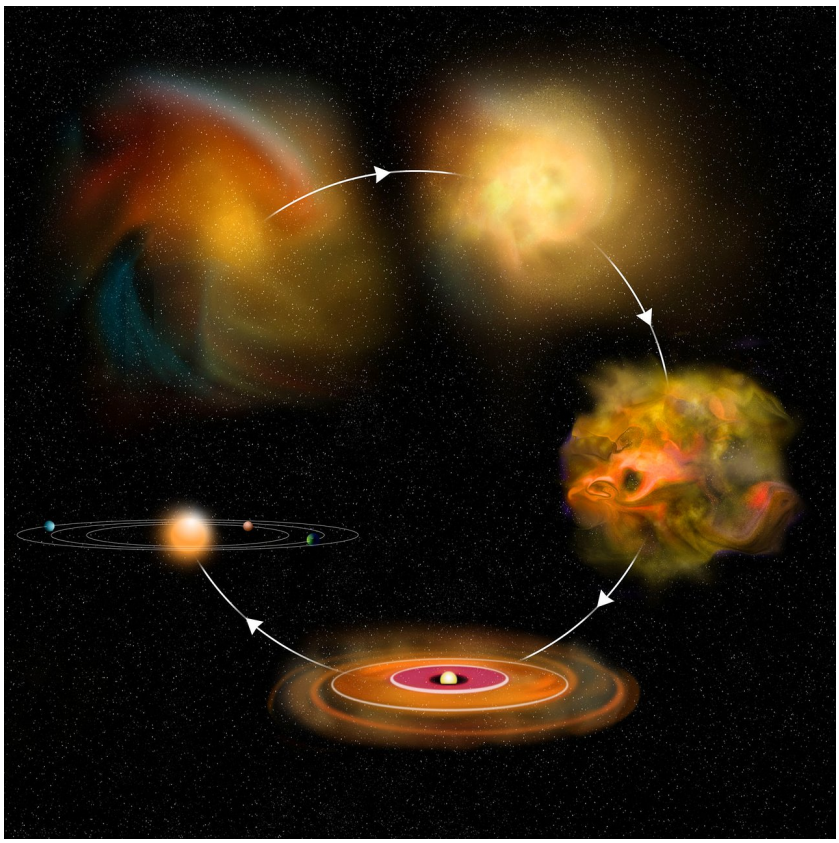

Figure 2.2: Artist impression of stellar evolution starting from a molecular cloud to a planetary system. Image Credit: Bill Saxton/NRAO/AUI/NSF

The evolution of the stars on the MS is highly affected by inner convection. Stars with $M_i < 1.15\ M_\odot$ do not have convection in their interiors. Without the convection, the fused He clumps together in the center due to its high mean molecular weight. When the He core becomes massive enough, the central fusion stops and it smoothly transitions to H shell burning. The absence of the convection leads to an intact He core which is isothermal. These objects follow a smooth transition from H shell burning MS objects to red giant branch stars (See Fig. 2.3). Stars with $M_i > 1.15\ M_\odot$, on the other hand, have convection in their interiors. Due to convection, core material mixes with the envelope material, therefore H rich material is transferred to the core. This results in more fusion and an increase in core temperature, hence the luminosity increases. When the He core reaches $0.5\ M_\odot$ of He mass, H fusion in the core suddenly stops which leads to core temperature decrease and further contraction of the core. After this point the star enters the terminal age main sequence (TAMS). Because of contraction, the outer edges of the He core show a temperature increase, which heats up the surroundings to start H shell burning. The evolution of the H shell burning depends on the initial mass.

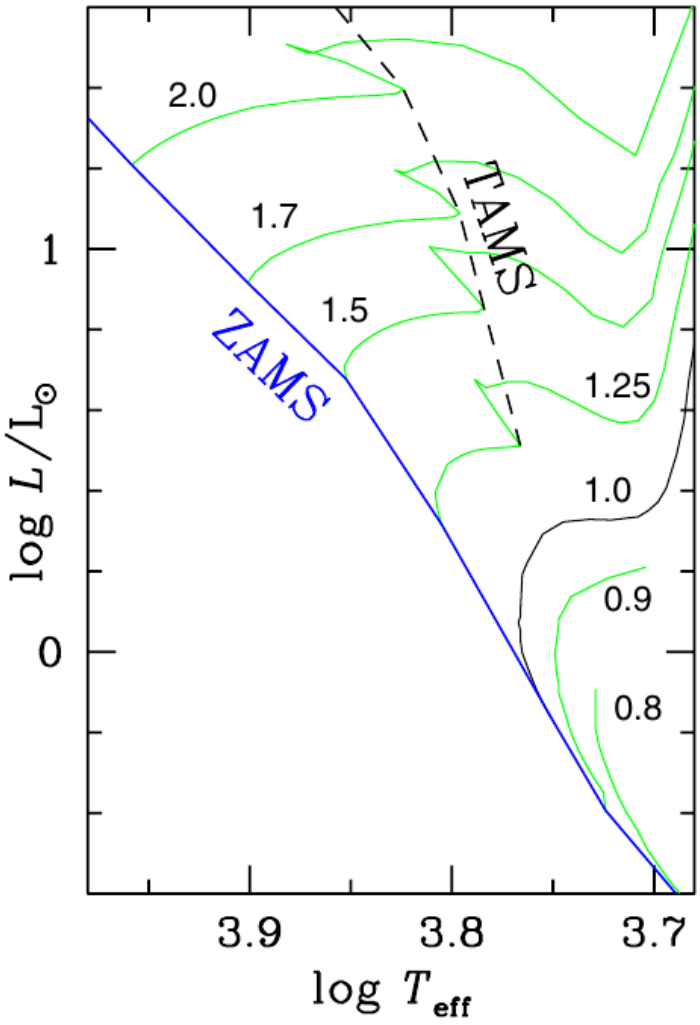

Figure 2.3: Locations of the zero-age main sequence (ZAMS, blue line) and the terminal-age main sequence (TAMS, black dashed line) on the log $T_{\rm eff}$ - log L diagram overplotted with evolutionary tracks (green and black solid lines) from Schaller et al. (1992). Taken from de Boer & Seggewiss (2008).

The non-degenerate He core of a intermediate mass star ($2\ M_\odot \leq M_i \leq 8\ M_\odot$) continues to grow as the H shell burning carries on, until it reaches the Schöneberg-Chandrasekhar limit which corresponds to a core mass limit ≈ 10 % of the stellar mass. Since H fusion in the core already ceased to exist, the core can not withstand the gravitational pressure and contracts further. This results in an expansion of the envelope and the star enters the red giant branch (RGB). After further H shell burning on the RGB, the He core reaches a temperature of $\sim 10^8$ K, which is high enough to start He fusion. To reach the thermal equilibrium, the core expands and the luminosity drops with the contracting envelope. At this point the star reaches the blue loop core He burning stage.

For the low mass stars ($M_i \leq 2\ M_\odot$), the He piles up in the core as the H shell burning continues. When the star enters the RGB phase, its core has already become degenerate and can not expand to cool down. The degenerate matter cools by neutrino emission which is most effective in the central region of the core. In other words a shell around the center will have higher temperatures. Ultimately, the outer regions of the He core (shell) will reach temperatures ($T \approx 10^8$) high enough to allow He fusion. However the He fusion does not continue for a long time and it produces a flash of energy called He flash. This brief energy outburst is comparable to what is emitted by the entire galaxy ($L = 10^{10}\ L_\odot$). The increase in temperature causes the degeneracy to vanish and until the degeneracy is lifted in the entire core these flashes continue. When He core burning starts and the star stabilizes, it reaches the horizontal branch (HB). Only objects with a horizontal branch mass $\geq 0.52\ M_\odot$ advance to the asymptotic giant branch (AGB).

Once He core burning ends, He fusion continues in the shell and the star enters the AGB. Events in this phase proceed similar to the end of the MS. In addition to He shell burning, the AGB star at the same time maintains H shell burning. In the final stages of the AGB phase, He shell burning is nearly exhausted. But H shell burning adds more He to the core. This generates an increase in the core temperature and, consequently, causes He burning to occur as flashes which happen rapidly (thermal pulses). The thermal pulses and the increased luminosity induces heavy mass loss in this stage. Later, the star further contracts to a post-AGB star. Due to contraction, the T_{eff} of the star increases substantially and if the star reaches $T_{\text{eff}} \sim 30$ kK, it ionizes the shed material, becoming a central star of a planetary nebula (CSPN). Ultimately, fusion stops and the star enters the white dwarf cooling sequence.

3

White Dwarfs

With Gaia, approximately 359 000 high-confidence white dwarf candidates were identified in the Milky Way (Gentile Fusillo et al., 2021) and more than 37 000 white dwarfs have been spectroscopically confirmed (Kepler et al., 2021). They are the most common end products of the stellar evolution and all stars with initial masses < 8 - 10 $M_\odot$ will end up as white dwarfs (Dobbie et al., 2006). Estimations show that it corresponds to approximately 97 % of all stars in the Milky Way (Fontaine et al., 2001). Apart from their substantial numbers, also their unique physical state that can not be achieved in any laboratory on Earth makes them viable objects for research (Koester, 2013). A typical white dwarf has a mass of 0.6 $M_\odot$ (see Fig. 3.1), but its size is comparable to a planet. In this dense environment, quantum mechanical effects become the dominant factor for the electrons, which as a result form a degenerate electron gas. According to the Pauli principle, as the volume decreases, electrons go up to higher momentum states which serves as a basis of the mass-radius relation for fully degenerate zero-temperature white dwarfs established by Chandrasekhar. In order for the star to stay in hydrostatic equilibrium, the pressure produced by the gravitational force (Eq. 3.1)[1] should be stabilized by the degenerate electron pressure since nuclear reactions have already ceased to exist.

$$P_\mathrm{c} \propto \frac{GM^2}{R^4} \tag{3.1}$$

In the non-relativistic limit, it translates to

$$P_\mathrm{c} \propto \left(\frac{\rho_c}{\mu_e}\right)^{5/3} \propto \left(\frac{M}{\mu_e R^3}\right)^{5/3} \tag{3.2}$$

and hence

$$R \propto {\mu_e}^{-5/3} M^{-1/3} \tag{3.3}$$

In other words, Eq. 3.3 can be rephrased as the well known property: the more massive the white dwarf, the smaller its size. On the other hand, relativistic degeneracy leads to another property, the Chandrasekhar mass (~ 1.4 $M_\odot$), which is the maximum mass that a white dwarf can possess.

[1] Equations are taken from Koester (2013).

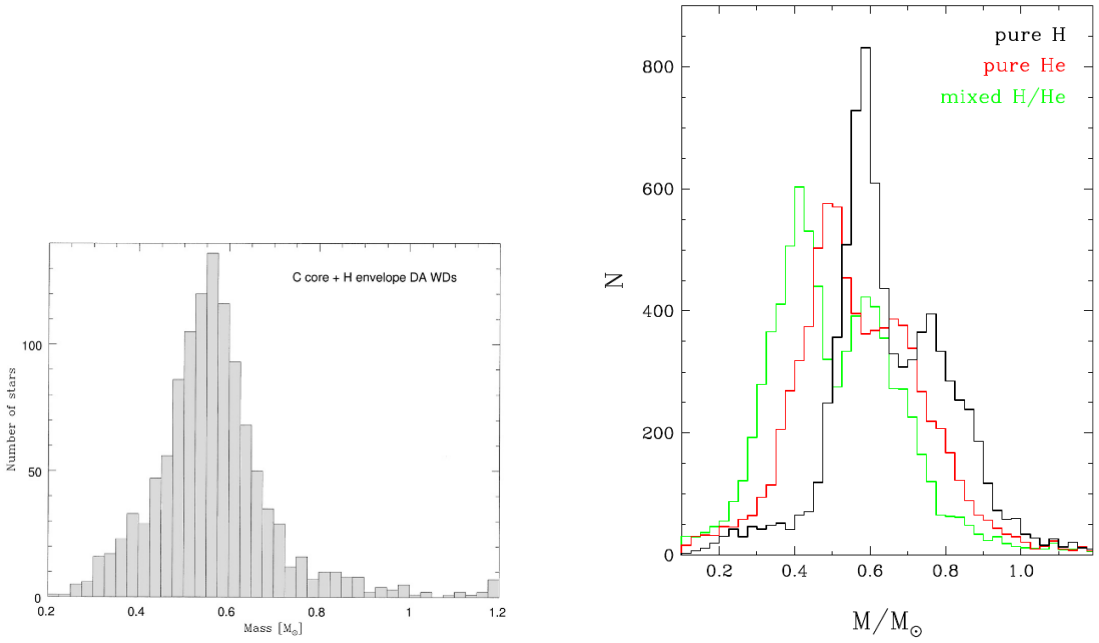

(a) Taken from Madej et al. (2004)

(b) Taken from Bergeron et al. (2019)

Figure 3.1: Observed mass distribution of white dwarfs from two different studies. In both of them, the mass distribution centers around $\sim 0.6\ M_\odot$ and extends to low-mass and high-mass ends decreasingly. It is believed that binary interaction is responsible for the low-mass end of the mass distribution since low-mass progenitors would need more than a Hubble time to reach the white dwarf stage (Fontaine et al., 2001; Althaus et al., 2010).

White dwarfs provide an insight into the final stages of stellar evolution for low and intermediate mass stars. With the initial-final mass relation (IFMR), it is possible to constrain the masses of the white dwarf progenitors when they entered the main sequence. This relation is not only important for stellar evolution, but also for the evolution of the galaxy, since it is the only viable method to learn how much mass is lost from the main sequence to the white dwarf stage. With this valuable information, the mass returned to the interstellar medium can be estimated, which is important for the star formation rate (Koester, 2013). White dwarfs can also be used to determine ages of the different galactic populations. Fontaine et al. (2001) states that the oldest white dwarfs in the solar neighborhood can be utilized to predict the age of the galactic disk. Since white dwarfs are progenitors of type Ia supernovae, they represent an essential element for cosmology (Perlmutter et al., 1998; Weinberg et al., 2013) as well.

3.1 White Dwarf Classification and Spectral Types

White dwarf spectral types can be divided into two basic categories: hydrogen rich and hydrogen deficient of which the occurrence ratio is approximately 4:1 (Hügelmeyer et al., 2006). Several processes that take place in the atmospheres generate the unique spectra of white dwarfs. Due to **gravitational settling** of heavy elements, most of the white dwarf spectra show only spectral lines of one element: either hydrogen or helium. Moreover, a strong radiation field can transfer momentum to trace metals in the atmosphere. This process is named as **radiative levitation** and it supports heavier elements against the gravitational settling, driving them upward into the atmosphere. In addition, as the white

dwarfs cool down, in a certain temperature range the atmospheres become **convective** which results in dredge up of elements (see section 3.1.4). Furthermore, because of gravitational settling heavy elements are expected to sink in the atmosphere, which should make them undetectable in the spectra. However, many white dwarfs show additional metal lines in their spectra, which indicates ongoing accretion of metals (Vauclair et al., 1979). For the white dwarfs in which the dominant mechanism is expected to be gravitational settling (meaning no radiative levitation or dredge up), the general consensus is that the metals originate from **accreted planetesimals** (Farihi et al., 2010; Jura & Young, 2014).

White dwarf spectral classification is affected by temperature. As the star cools down, a change in the spectral type can be observed depending on the initial composition and with the effect of arising aforementioned processes. The temperature of a white dwarf is an important parameter which allows to determine luminosity and age of the object when combined with the spectroscopically derived surface gravity log g and the evolutionary models. Therefore, a temperature index described as 10 $\times\theta_{\rm eff}$ ($= 50400/T_{\rm eff}$) was introduced (Sion et al., 1983). Finally, the main WD spectral and sub-spectral types are listed in Table 3.1 and 3.2, respectively.

Spectral Type	Main Characteristics	Spectral Lines
DA	H-rich	H I
DO	He-rich ($T_{\rm eff} \geq 80\,000$ K)	He II
	He-rich ($45\,000$ K $\leq T_{\rm eff} \leq 80\,000$ K)	He II + He I
DB	He-rich ($T_{\rm eff} \leq 45\,000$)	He I
DQ	Cool DQs: He-dominated ($T_{\rm eff} \leq 13\,000$)	Molecular and/or atomic C, He I
	Hot DQs: C-rich ($18\,000$ K $\leq T_{\rm eff} \leq 24\,000$ K)	C II, C I, O I
DZ	Metal Lines	e.g. Ca II, Mg, I
DS	O-rich	O I, O II, metal lines
DC	Featureless spectrum	No lines

Table 3.1: Main white dwarf spectral types.

Sub-spectral Type	Characteristic
H	Magnetic (shows Zeeman splitting)
V	Variable
UHE	Ultra-high excitation absorption lines
Z	Indicating metal lines
E	Emission lines
+MS	Composite spectrum (WD + Main sequence star)
x	Peculiar or unclassifiable spectrum
?	Uncertain assigned classification

Table 3.2: White dwarf sub-spectral types.

3.1.1 DA White Dwarfs

Hydrogen rich white dwarfs form the spectral type DA. They are observed in a broad effective temperature range from 4 500 K to 170 000 K (Sion, 2011) and constitute $\sim$ 80 %

of all white dwarfs (Eisenstein et al., 2006a). DA white dwarfs can be classified conveniently, because Balmer lines of hydrogen can be detected in a wide temperature range from 4 000 K $\leq T_{\rm eff} \leq$ 120 000 K. However, as the temperature increases or decreases, the Balmer lines become weaker since most of the H is ionized or in the ground state, respectively. For the estimation of $T_{\rm eff}$ and log g of the hot DAs in addition to Balmer lines, the Lyman series in UV can be utilized as well.

3.1.2 DO White Dwarfs

DO white dwarfs show He rich spectra in a broad temperature range (45 000 K $\leq T_{\rm eff}$ $\leq$ 200 000 K). Depending on their temperature, these objects show He I and He II lines ($T_{\rm eff} \geq$ 45 000 K) or only He II lines ($T_{\rm eff} \geq$ 80 000 K). Kepler et al. (2021) report 137 spectroscopically confirmed DO white dwarfs. The dearth of DOs can be explained because the early stages of white dwarf cooling happen in only 2 Myr (Althaus et al., 2009).

PG 1159 Stars

PG 1159 stars are observed in a vast temperature interval (75 000 K $\leq T_{\rm eff} \leq$ 200 000 K; see Fig. 3.2). These H-deficient objects additionally show C- and O-rich spectra and are regarded as progenitors of DO white dwarfs (Werner et al., 2014). DOZ white dwarfs (log $g \geq 7$) with C abundances C/He $\geq$ 0.02 (by number) may be classified as PG 1159 stars (Werner et al., 2014). On the other hand, PG 1159 stars with log $g < 7$ are actually post AGB stars and their H deficiency is more likely due to (very) late thermal pulses (Werner & Herwig, 2006).

3.1.3 DB White Dwarfs

DB type white dwarf spectra are composed of neutral helium which is the product of recombined He II as the DO white dwarf cools down (Althaus et al., 2010) which requires $T_{\rm eff} \leq$ 45 000 K. Most of the DB white dwarfs are observed in a $T_{\rm eff}$ range from 30 000 K to 12 000 K (Sion, 2011). The lack of the objects in this transition phase is named as DB gap and only a few objects have been reported in this region (Eisenstein et al., 2006b; Kleinman et al., 2013). However, the idea of the DB gap being an empty hole with boundaries was later discarded since in this region objects have been found and the hotter boundary of this region does not show a clear cut (Bédard et al., 2020).

3.1.4 DQ White Dwarfs

DQ white dwarfs show carbon dominated spectra which can be identified with the C_2 molecules (Swan band) or atomic C. According to their temperature, they are divided into two sub-categories: cool (normal) DQs and hot DQs. Normal DQs are recognized with the Swan bands. Most of the objects with $T_{\rm eff} \leq$ 10 000 K are believed to have He dominated atmospheres, however this element can not be spectroscopically detected. It is acknowledged that the spectra of cool DQs are produced due to dredge-up of carbon in

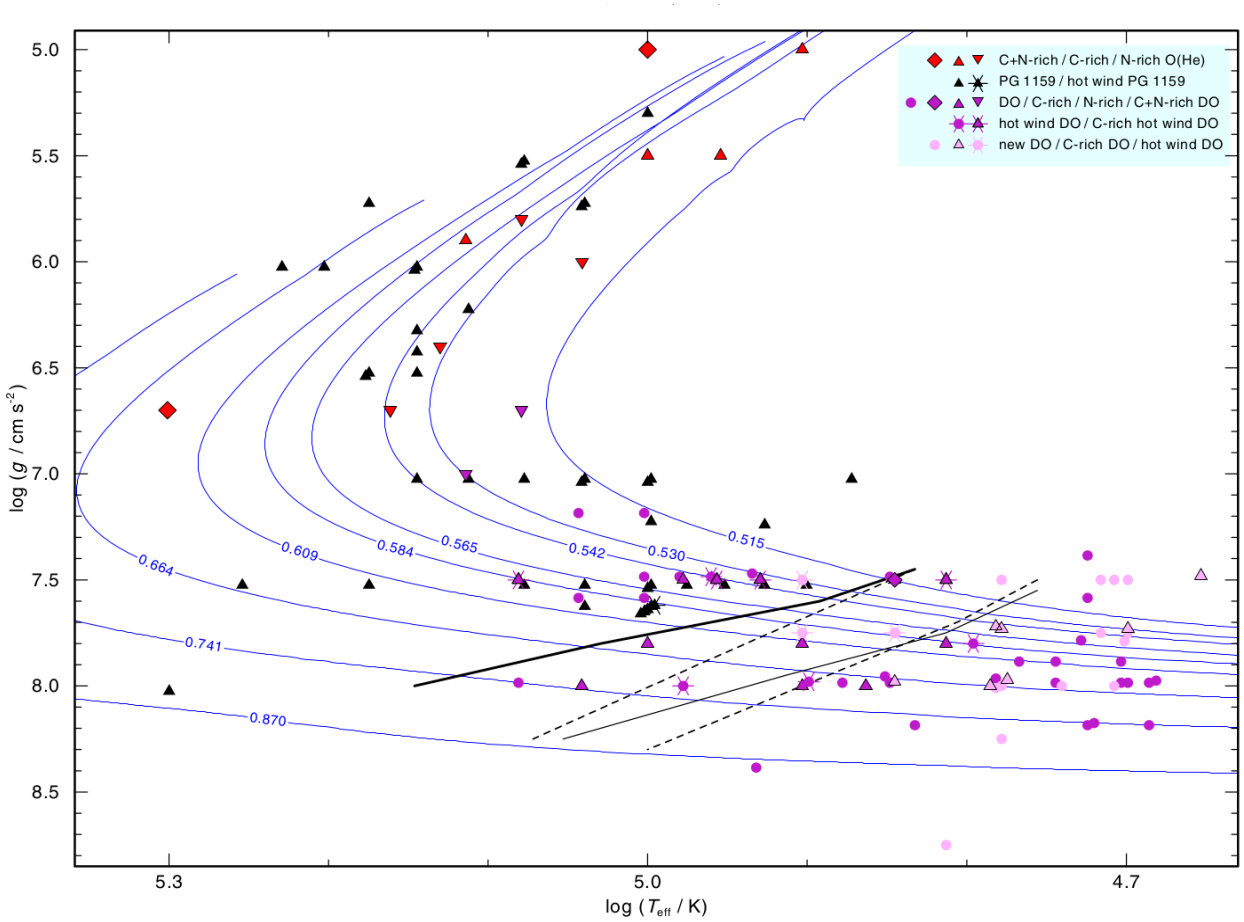

Figure 3.2: Locations of PG 1159 stars (black triangles) and DO white dwarfs (purple circles, diamonds and triangles) in the Kiel diagram with the evolutionary tracks from Althaus et al. (2009). Taken from Reindl et al. (2014)

the convective He atmosphere (Koester et al., 1982). Cool DQ white dwarfs have similar masses as DA and DB white dwarfs. Hot DQs, however, are completely different from cool DQs with masses above 0.9 $M_{\odot}$ (Koester et al., 2020). It is believed that these objects are merger products of two white dwarfs (Dunlap & Clemens, 2015). Hot DQs are observed in an effective temperature interval from 18 000 K to 24 000 K, but do not exhibit any H or He lines in their optical spectra (Sion, 2011).

3.1.5 DZ White Dwarfs

In the recent years, many metal polluted white dwarfs have been detected (Gänsicke et al., 2012; Manser et al., 2016; Dennihy et al., 2018). However, due to gravitational settling it is expected that heavy elements such as Ca, Mg and Fe should not be detectable in the spectra since the expected diffusion timescales are shorter than the evolutionary timescales of the white dwarfs (Koester, 2009). This indicates that the metals must be accreted on the white dwarf from an external source. DZ white dwarfs only exhibit metallic lines in their spectra and their atmospheres are believed to be helium dominated. Therefore, these objects must have cooled down below a certain temperature ($T_{\rm eff} \leq 12\,000$ K) since He lines are not present (Hollands et al., 2017).

3.1.6 DS White Dwarfs

DS white dwarfs show oxygen dominated spectra and so far only four objects have been detected (Kepler et al., 2021). Gänsicke et al. (2010) reported a peculiar object with a $T_{\rm eff} \approx 8\ 000$ K that exhibits a highly O-rich atmosphere as well as weak H-α and H-β lines. Also Kepler et al. (2016) presented a unique object that shows dominantly O I, in addition to O II and Mg II lines. They state that no He or H lines are present contrary to what is expected. Later it was suggested that oxygen rich objects can be categorized as DS white dwarfs (Williams et al., 2019).

3.1.7 DC White Dwarfs

DC white dwarfs exhibit featureless spectra which indicates that these objects must have cooled below a certain temperature. If the $T_{\rm eff} \geq 5\ 000$ K, it is assumed that these white dwarfs have He dominated atmospheres since above 5 000 K H lines should be still present in the spectra.

3.1.8 Sub-spectral Types

The symbols in 3.2 describe any peculiarities that are present in the white dwarf spectra. Letter "H" denotes magnetic white dwarfs showing Zeeman splitting in the spectra. Letter "V" indicates photometric variability. Sub-types such as DOV, DBV, and DAV represent the pulsating white dwarfs on the cooling sequence. "UHE" indicates white dwarfs showing ultra highly excited metals in the optical spectra. If the spectra exhibit metal lines, in addition to the main element, letter "Z" added to the main spectral type (e.g. DOZ, DBZ, DAZ). "E" indicates that the white dwarf spectrum contains emission lines. The "+MS" symbol represents a composite spectrum which shows the spectral signature of a main sequence star in addition to the spectral lines of a white dwarf. "x" indicates that the spectrum is peculiar or unclassifiable and "?" denotes an uncertain classification.

4

Photometric Variability in Hot Stars

Brightness changes can unveil ongoing processes in the stars. These variations are studied via their light curves which not only can inform about their internal properties but also interactions with their surroundings. Stars that show periodic flux changes are called variable stars and can be categorized in 2 main groups:

- Intrinsic variable stars
- Extrinsic variable stars

Intrinsic variability occurs due to the star's internal mechanisms whereas extrinsic variables are affected by external sources such as a companion. In this chapter, some of the intrinsic and extrinsic variability types detected in hot stars are discussed.

4.1 Extrinsic Variables

4.1.1 Ellipsoidal Deformation & (Over-)Contact Binaries

In a close detached binary system (stars staying within their Roche lobes), one star with strong tidal forces may influence its companion gravitationally causing it to have a deformed shape. This leads to sinusoidal variations in the light curve with the half orbital period of the system (Wilson & Vaccaro, 1997). In other words, the light curves of such systems show two maxima and minima in one orbital period (see Fig. 4.2). Ellipsoidal deformation is commonly observed in sdB + WD binaries (Geier et al., 2007, 2008, 2015; Bloemen et al., 2011) and may confirm tidal synchronisation in binaries (Geier et al., 2008).

(Over)-Contact binaries are formed when both of the components (over-)fill their Roche lobes. This causes recurrent variations in the light curves which show extended maxima and two uneven minima (Drake et al., 2014). Such systems are also sometimes observed with V-shaped light curves (see Fig. 4.1). The evolution of the components in such systems is affected by the mass transfer and the tidal interactions and follows a different path than single stellar evolution.

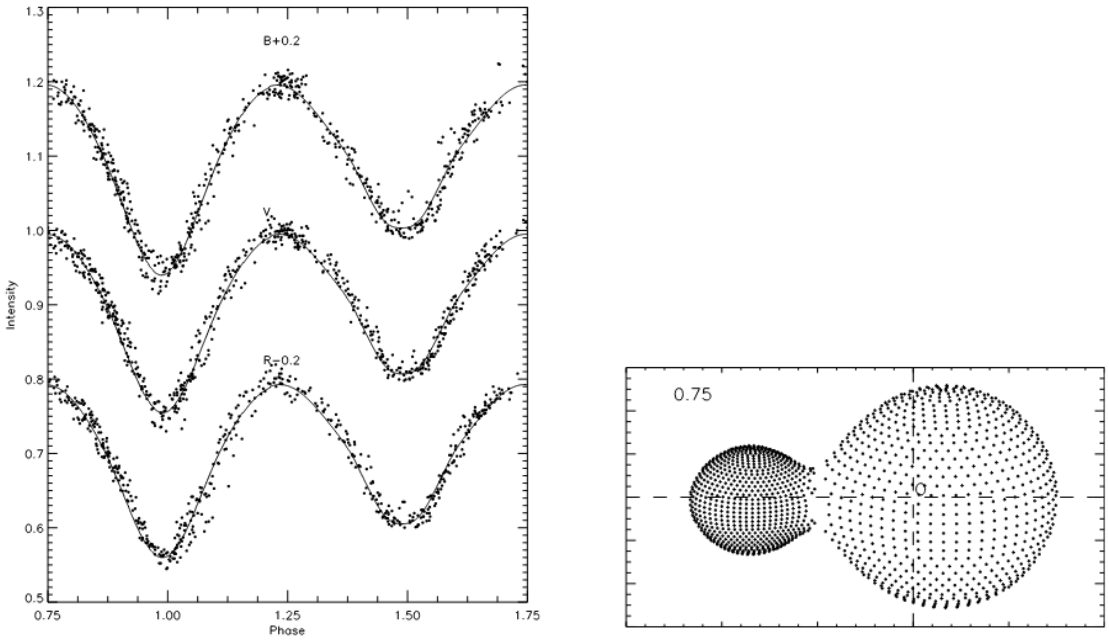

(a) (b)

Figure 4.1: Example of an over-contact binary. Panel (a) a shows multi-band light curve of V2388 Oph. Panel (b) shows the 3-D representation of V2388 Oph at phase 0.75. Taken from Yakut et al. (2004)

4.1.2 Reflection Effect Binaries

Reflection (irradiation) effect binaries are composed of a hot primary and a cool companion. In these close binary systems, the cool companion is expected to be synchronized to the primary. Therefore, one side of the cool companion is constantly heated by the primary which is detected in the light curves as a periodic flux variation as the orbital configuration of the system changes. The amplitudes of the reflection effect light curves depend on the temperature difference, radii and orbital separation of the components (Wilson, 1990; Budaj, 2011). So, for binaries with similar radii, smaller orbital separation and higher temperature difference, the observed light curve amplitudes are larger (Schaffenroth et al., 2018). Multi-band photometry of objects might point out to reflection effect systems, in case the observed light curve amplitude is larger in the redder wavelengths than in the blue. This is simply because the day side of the cool companion will have a more prominent contribution in the redder bands. Moreover, the inclination angle i of a reflection effect system can be constrained with light curve modelling, which remains as an integral part to determine the masses of the binary components. For systems with a low inclination angle ($i \approx 10°$), the light curve varies sinusoidal (see Fig. 4.2), whereas larger inclination angles result in narrower maxima and flat minima. Eclipses become visible for the binaries with high inclination.

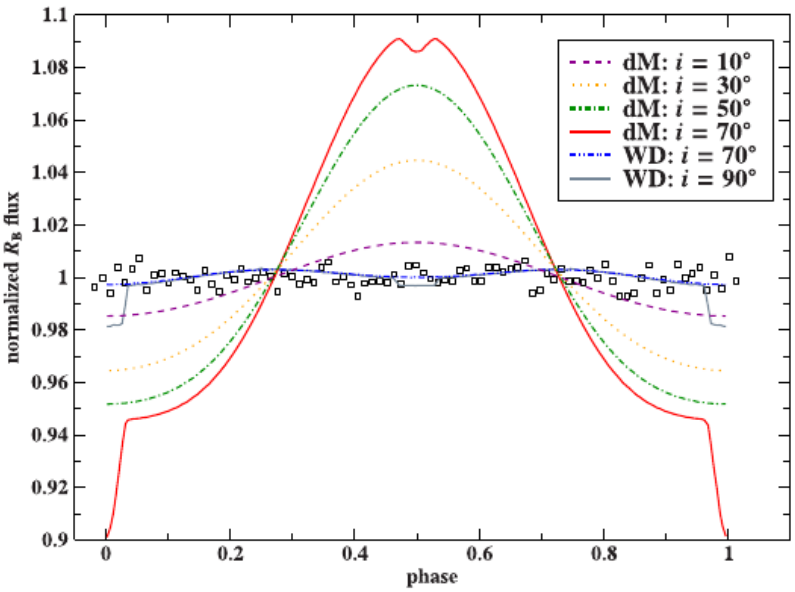

Figure 4.2: A comparison of reflection effect and ellipsoidal deformation light curve models for a given orbital period and several inclination angles (i) of sdB binaries. Models marked with "dM" indicate a reflection effect system (sdB binary with low-mass stellar or substellar companion). As i increases, eclipses become visible ($i = 70°$). Models designated with "WD" represent a sdB binary system with a low mass WD (ellipsoidal deformation). Amplitudes measured from reflection effect models are much larger than ellipsoidal deformation models for the same period. Taken from Schaffenroth et al. (2018)

4.2 Intrinsic Variables

4.2.1 Pulsations

Pulsations are important mechanisms to probe the interior structure of the stars and are observed in many regions on the HRD (see Fig. 4.3). Parameters such as sound speed and density can be determined for a set of quantum numbers (Bellinger et al., 2021). Oscillations that occur due to radial expansion and contraction of the star's atmosphere are named as radial pulsations. On the contrary, non-radial pulsations describe the oscillations which are generated because of irregular inward and outward movements of the stellar surface. GW Vir and sdBV types are examples for hot non-radial oscillating stars (Christensen-Dalsgaard, 2008).

4.2.2 Spots

Spots on the stellar surface may produce photometric variability due to rotational modulation of the star which is commonly observed in MS stars (Sundqvist et al., 2012; Sikora et al., 2019). Unlike the cool stars e.g. the Sun on which the spots are observed as cooler regions and hence, cause a decrease in brightness, spots produced on hot stars are expected to be generated by magnetic fields and have higher temperatures than the stellar surface (Cantiello & Braithwaite, 2011). Depending on the observed waveband and element distribution, such regions may induce brightness increase or decrease in the light curves (Krtička et al., 2018). It is proposed that magnetic fields are also responsible

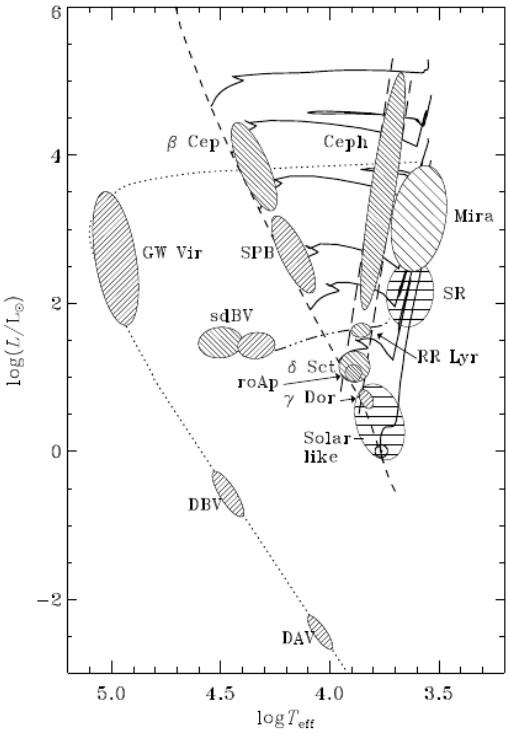

Figure 4.3: Location of pulsating stars on the HR diagram. Taken from Christensen-Dalsgaard (2008).

for the creation of spots on white dwarf surfaces via accumulation of metals around the magnetic poles (Hermes et al., 2017).

4.2.3 Magnetosphere

Magnetospheres are formed when the radiation driven stellar wind of the star is confined by the closed magnetic loops. Magnetic OB type stars commonly exhibit properties of such magnetospheres and several projects were conducted to better comprehend the combined effects of the magnetism and stellar winds in hot stars (Wade et al., 2011, 2012; Sundqvist et al., 2012; Petit et al., 2014). It has been hypothesized that the photometric variability observed in the magnetic O-type stars is caused by magnetospheric electron scattering (Munoz et al., 2020). As the star rotates, the projected area of the magnetosphere changes if the rotation axis is tilted with respect to the magnetic axis. This results in flux variations. Munoz et al. (2020) modelled synthetic light curves of magnetic O-type stars with several parameters. Inclination angle i, magnetic obliquity angle β, mass-feeding rate $\dot{M}_{B=0}$, dipolar magnetic field strength B_d, terminal wind velocity v_∞, and smoothing length δ. It has been shown that variations in geometric angles i and β affect the light curve shapes, whereas the latter four parameters change the amplitudes (see Fig. 4.4).

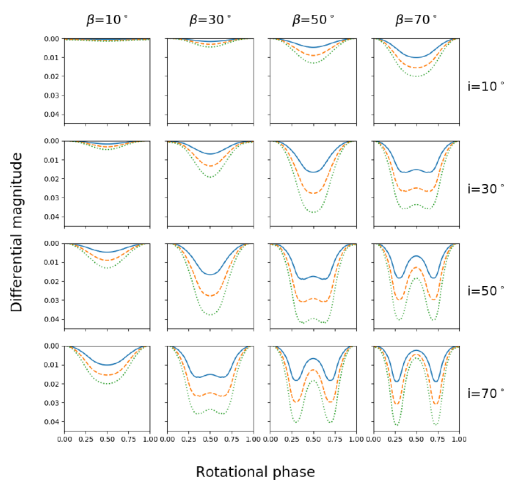

(a) Blue, orange and green lines represent values of $\dot{M}_{B=0} = \{1.0, 2.0, 3.0\} \times 10^{-6}$ $M_\odot$ yr^{-1}, respectively.

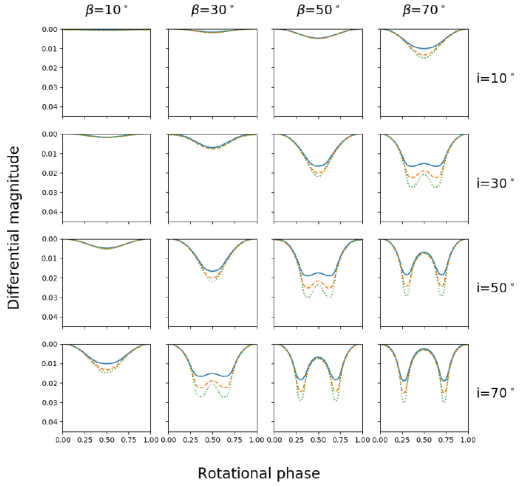

(b) Blue, orange and green lines represent values of $B_d = \{2.5, 5.0, 7.5\}$ kG, respectively.

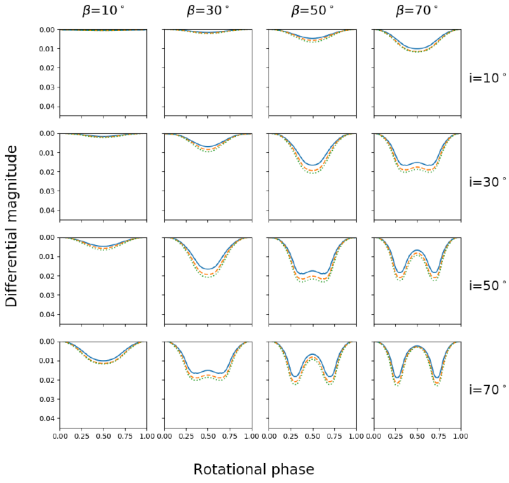

(c) Blue, orange and green lines represent values of $v_\infty = \{1500, 2500, 3500\}$ km s^{-1}, respectively.

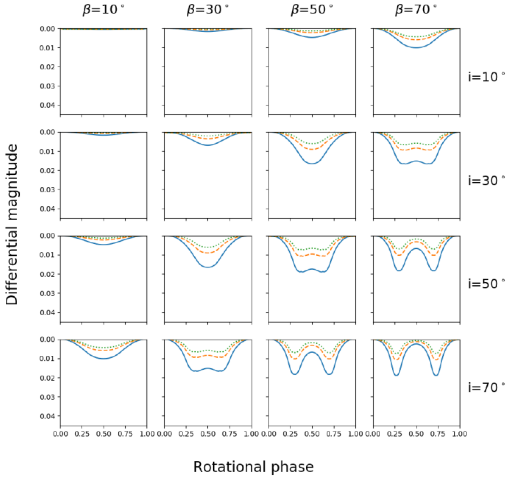

(d) Blue, orange and green lines represent values of $\delta/R_* = \{0.1, 0.3, 0.5\}$, respectively.

Figure 4.4: Grid of model light curves as a function of inclination i, and obliquity β. Panel (a), (b), (c), and (d) show varying stellar parameters. In each panel only one parameter changes and remaining values are based on HD 191612. Taken from Munoz et al. (2020).

5

White Dwarfs Showing Ultra-High Excitation Lines & He II Line Problem White Dwarfs

5.1 State of the Art

5.1.1 Origin of Ultra-High Excitation Lines

Combined X-Ray, UV and optical studies revealed many exotic objects, however, a particular type that reside among the hottest white dwarfs conceals an interesting yet perplexing phenomenon: white dwarfs showing ultra-highly excited (UHE) metals (e.g. C V, C VI/N VI, N VII/O VII, O VIII, Ne IX, and Ne X) in their optical spectra. These enigmatic objects were discovered nearly three decades ago by Werner et al. (1995) in the Hamburg-Schmidt objective prism surveys (Wisotzki, 1994; Hagen et al., 1994) and previous to that these features have never been observed in any other astrophysical object.

Considering the fact that the maximum observed white dwarf temperatures do not exceed 250 000 K (Werner & Rauch, 2015), it is puzzling to encounter UHE absorption features in a white dwarf spectrum. UHE line formation requires temperatures on the order of a million K (Werner et al., 1995) which surpasses the stellar effective temperatures. This temperature range would also not allow to detect Balmer/He II lines, therefore the possibility of UHE lines originating from the photosphere can be rejected. Because of the asymmetrical shapes of the line profiles, it was suggested that UHE features stem from an optically thick, hot stellar wind (Werner et al., 1995). Therefore, these objects are also commonly known as ***hot wind white dwarfs***. Furthermore, due to their high temperatures and indications of mass loss, a search for planetary nebulae around hot wind white dwarfs was also attempted. However, it resulted in non-detection (Werner et al., 1997).

The Balmer/He II line problem was known to be inherited by hot wind white dwarfs which exhibit broader and deeper aforementioned spectral lines than the models predict (Werner et al., 1995; Dreizler et al., 1995). Additionally, Werner et al. (2004) reported an unusual DO white dwarf without the presence of UHE features but exhibiting strong He II lines that can not be fitted by any model (see Fig. 5.2). Previous to that, the

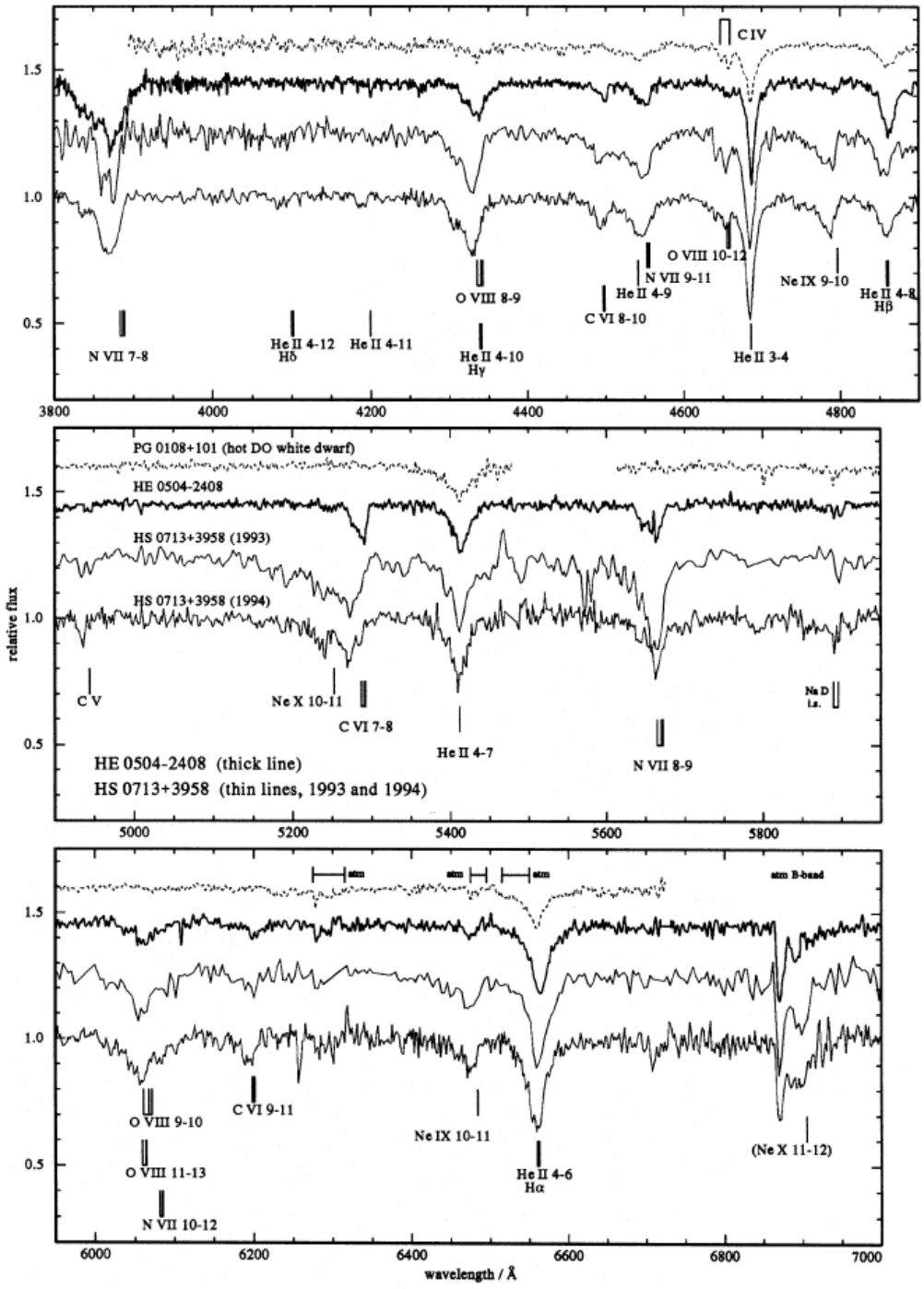

Figure 5.1: Normalized spectra of the first discovered UHE white dwarfs HE 0504-2408 and HS 0713+3958 as well as the DO white dwarf PG 0108+101. UHE lines are marked as C, N, O, and Ne ions. Taken from Werner et al. (1995).

so-called Balmer line problem had been already encountered in DA white dwarf spectra (Napiwotzki, 1993) and was shown to occur due to improper inclusion of metal opacities in the models (Werner, 1996). However, this solution remains ineffective in some cases for the DAs showing the Balmer line problem (Werner et al., 2018b, 2019) and for all the DOs showing the He II line problem (Werner et al., 2018a). Werner et al. (2014) suggested that UHE and DO white dwarfs showing the He II line problem are affected by the same unknown mechanism which, however, fails to produce UHE lines in the He II line problem white dwarf spectra.

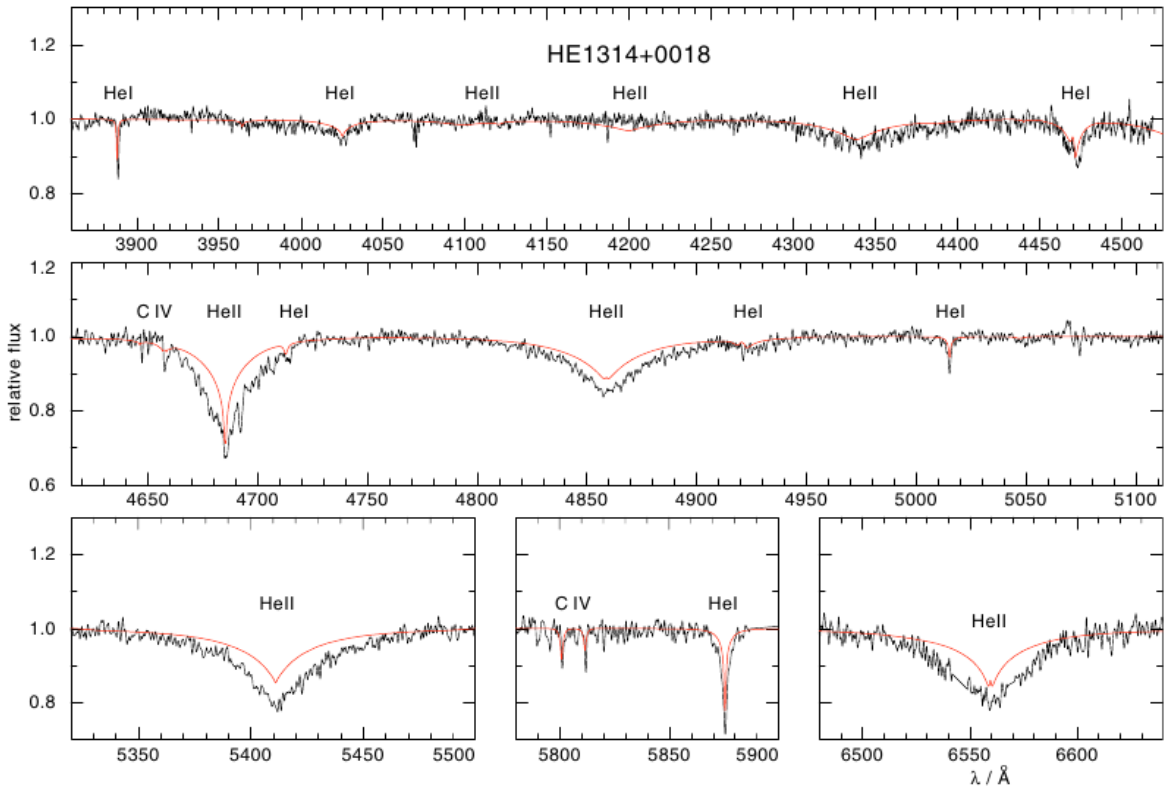

Figure 5.2: Normalized UVES spectrum of the first detected DO white dwarf showing the He II line problem. Red lines represent a model with $T_{\rm eff}$ = 60 000 K. log g = 7.5, and C/He =0.001. He II lines can not be fitted precisely. Taken from Werner et al. (2004).

A proper assessment of parameters such as $T_{\rm eff}$, log g and mass highly depends on the correct employment of the model atmospheres, for which H and He lines are fitted. However, the Balmer/He II line problem complicates the accurate determination of these parameters. For that reason, Werner et al. (2018a) analyzed UV spectra of 3 UHE white dwarfs by constraining the $T_{\rm eff}$ range with H and/or He models and utilizing several ionization stages of UV metals. They reported $T_{\rm eff}$ values similar to what was inferred from optical spectra, except for one object. In addition, they did not encounter indications of ongoing mass loss in the UV spectra, however, they reported that this was not surprising considering the mass-loss rates anticipated by radiation-driven wind theory (Unglaub & Bues, 2000) are too low to be spectroscopically identified from the studied metal lines in UV.

Werner et al. (2018a) argued that the "superionization" process responsible for the occurrence of UHE lines could be frictional heating in multi-component radiation driven

winds which was explained as radiation pressure accelerating only metal ions, but He and/or H remaining static. It is predicted that the static material (H and He) builds a cloud around the star which could be the forming region of both UHE and H/He II lines, yet UHE lines arising due to frictionally heated metals (Werner et al., 2018a). Fig. 5.3 shows a $T_{\rm eff}$ - *log g* diagram including a narrow band where frictionally heated multi-component winds are theorized to happen (Krtička & Kubát, 2005). This narrow band could clarify the reason behind the observed $T_{\rm eff}$ range (65 000 to 120 000 K) of UHE white dwarfs (Werner et al., 2018a). However, the frictionally heated wind model is unable to justify why not every hot white dwarf in this band exhibits the UHE phenomenon (Reindl et al., 2021). Reindl et al. (2021) also argued that the multi-component wind model is insufficient to describe the observed photometric and spectroscopic variability of the bright UHE white dwarf J0146+3236.

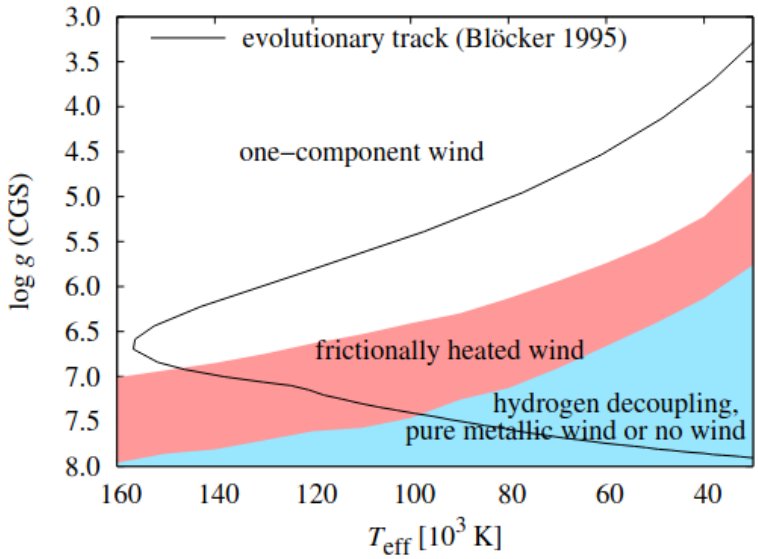

Figure 5.3: $T_{\rm eff}$ - log g diagram showing different type of stellar winds with models derived for 0.6 $M_\odot$ stars. The black line represents the evolutionary track (Bloecker, 1995). The pink region where frictional heating in the winds is expected to occur coincides with the same region in $T_{\rm eff}$ - log g at which hot wind white dwarfs are observed (Werner et al., 2018a; Reindl et al., 2021). Taken from Krtička & Kubát (2005).

Reindl et al. (2019) reported the analysis of the hot wind white dwarf J0146+3236, which shows changing equivalent widths (EWs) of UHE features as well as photometric variability. Strikingly, the recurrent variations of both, the EWs of the UHE line at 6060 Å and the light curve of the object, correspond to the same phase (see Fig. 5.4). Fig. 5.5 shows the spectra of J0146+3236 taken at different phases in which the drastic changes of the EWs of the UHE lines (especially at 6060 Å) can be noticed even visually. The EWs of UHE features reach their maximum at $\Phi \approx 0$ and their minimum at $\Phi \approx 0.5$, with some of the lines completely fading away at this phase.

Assuming the photometric period to be the rotational period of the star, Reindl et al. (2019) suggested that a spot on the surface can explain photometric variability. Since stellar atmospheres are highly radiative in this temperature range ($T_{\rm eff} \approx 100$ kK), they discarded the possibility of convection generating the spots and argued that spots should be

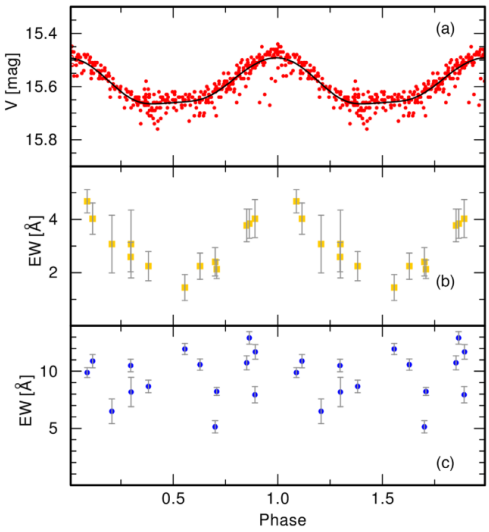

Figure 5.4: (a) Phase folded light curve of J0146+3236 including a bright spot model (black line). The model assumes an inclination angle of $i = 50°$ and 125 % spot brightness relative to the stellar surface. Panel (b) and (c) display equivalent width variations of the UHE line at 6060 Å and the He II line at 6560 Å, respectively. Taken from Reindl et al. (2019).

created by magnetic fields. However, none of the UHE white dwarfs including J0146+3236 exhibit Zeeman splitting, which constrains the magnetic field strength to an upper limit of 100 kG (Reindl et al., 2019). Nevertheless, the occurrence of the spots has been encountered on white dwarfs even with magnetic field strengths less than 10 kG (Hermes et al., 2017).

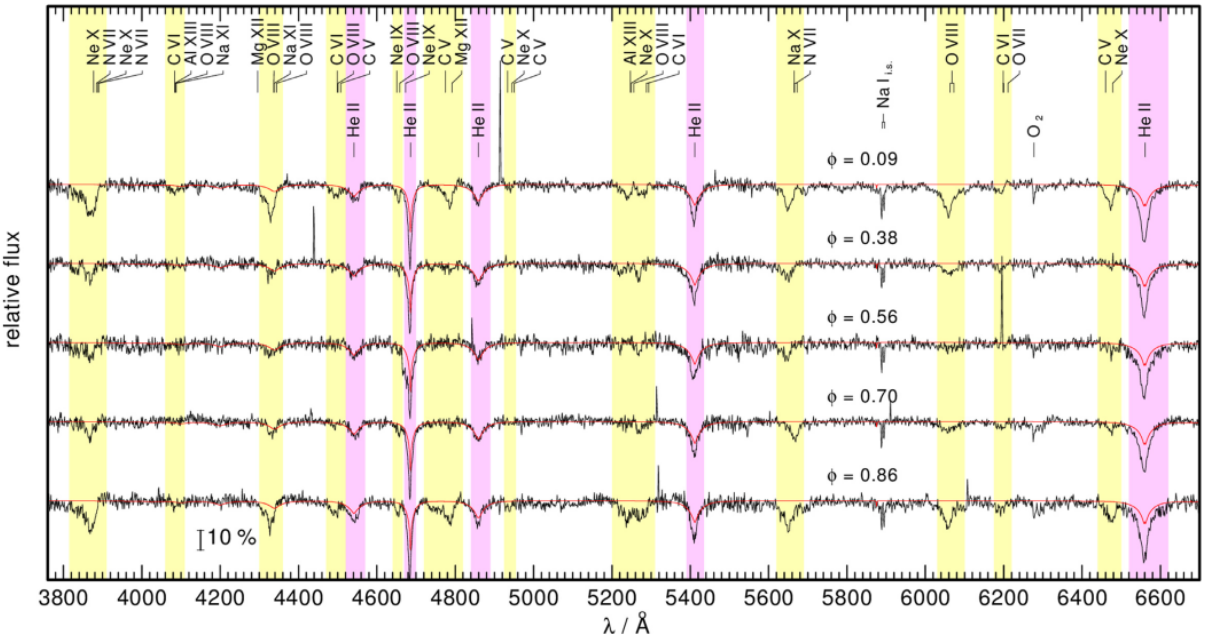

Figure 5.5: Normalized TWIN spectra (grey) of J0146+3236 including a pure He TMAP model with $T_{\rm eff} = 100\,000$ K and $\log g = 7.5$ (red). UHE features and He II lines are highlighted in yellow and pink, respectively. Taken from Reindl et al. (2019).

Reindl et al. (2019) showed that a wind fed circumstellar magnetosphere and a possible bright spot on the stellar surface can explain the photometric variability and spectro-

scopic variations of UHE features as well as their presence. Circumstellar magnetospheres are formed when the star's radiatively driven wind material is trapped inside the closed magnetic loops, which are commonly detected around massive O and B type stars with magnetic fields more than 1 kG (Owocki et al., 2016). As the wind material is channeled along the opposite parts of closed magnetic loops, flows from both sides collide in the equator, creating magnetically confined wind shocks (MCWS) (Babel & Montmerle, 1997; ud Doula & Nazé, 2016). MCWSs can increase the temperature to order of a million K (ud Doula & Nazé, 2016; Wade et al., 2015) which is necessary for the occurrence of UHE features (Reindl et al., 2019).

Reindl et al. (2019) explained the occurrence of variable UHE lines and photometric variability that were observed in J0146+3236 with rotational modulation of our viewing angle of the star and the circumstellar magnetosphere, if the magnetic axis is tilted by 45° with respect to the rotation axis. As the star rotates, the amount of seen shock-heated plasma changes, hence the line strengths of the UHE lines and the brightness of the system varies (see Fig. 5.6). It is predicted that the UHE lines originate from higher latitudes of the magnetosphere which is less dense, but hotter compared to lower latitudes and too deep and strong He II lines likely stem from cooler parts of the magnetosphere (Reindl et al., 2019).

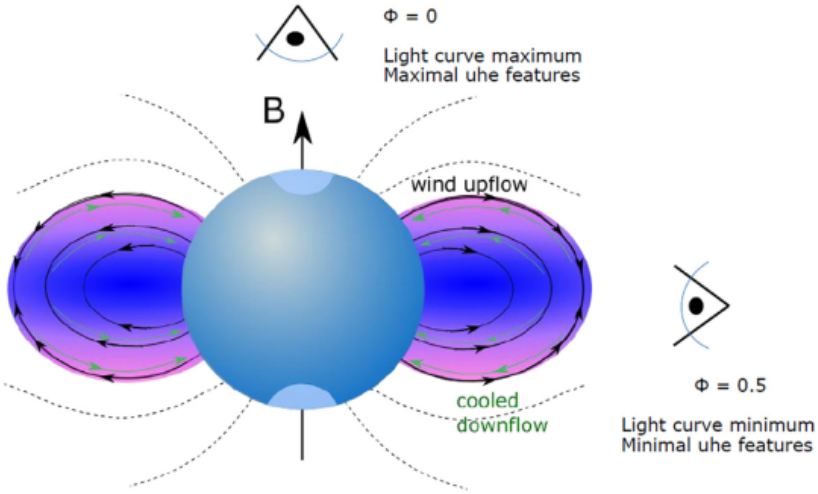

Figure 5.6: Illustration of J0146+3236 with the magnetosphere. The star is represented in blue and the magnetosphere is represented in blue, purple, and magenta. Spots on the magnetic poles are shown in light blue. The angle between magnetic axis and rotation axis is assumed to be 45°. At $\Phi = 0$ the system is viewed magnetic pole-on and the entire magnetosphere as well as a possible bright spot are visible. Hence, the UHE features and the light curve have their maximum. At $\Phi = 0.5$, the system is seen edge-on. The magnetosphere is occulted by the star and the amount of shock heated plasma decreases. Therefore, both the UHE features and the light curve diminish. Image taken from Reindl et al. (2019).

Magnetospheres are categorized by the rotation speed of the star (Petit et al., 2013). But before the characterization of the magnetospheres, several parameters should be defined. Whether the dipole magnetic field can deflect the stellar wind is described by the *magnetic wind confinement parameter*,

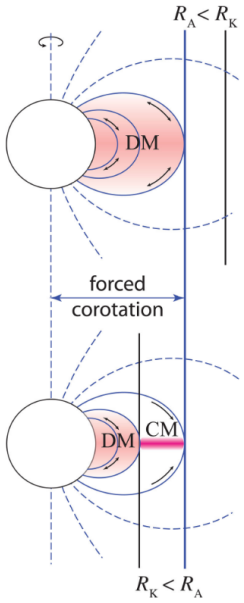

Figure 5.7: Illustration of two different types of magnetospheres: dynamical magnetosphere (DM) and centrifugal magnetosphere (CM). The top panel depicts a DM for slow rotators ($R_A < R_K$) of which the Alfvén radius (R_A) lies beneath the Kepler rotation radius R_K. The bottom panel illustrates the CM of rapidly rotating stars which is supported by the centrifugal force ($R_A > R_K$). In this case, the Alfvén radius (R_A) is located beyond the Kepler rotation radius R_K. Image taken from Petit et al. (2013).

$$\eta_* = \frac{B_{eq}^2 R_*^2}{\dot{M}_{B=0} v_\infty}, \tag{5.1}$$

where $B_{\rm eq}$ is the field strength at the magnetic equatorial surface radius (R_*), $\dot{M}_{B=0}$ is the mass-loss rate and v_∞ is the terminal wind speed which the star would show without a magnetic field (ud Doula & Owocki, 2002; Ud-Doula et al., 2008). For $\eta_* > 1$, the wind is confined within the Alfvén radius (R_A), resulting in the formation of a magnetosphere. R_A is the point where the magnetic energy density is equal to the wind kinetic energy density (ud-Doula et al., 2006). In other words, magnetic loops reaching beyond R_A stay open and the ones remain within R_A stay closed (Petit et al., 2013). Another essential parameter is the *Kepler corotation radius* (R_K) which is defined as the point where the centrifugal force due to corotation is equal to the local gravitational force of the star (ud-Doula et al., 2006).

Fig. 5.7 illustrates the formation requirements of two kinds of magnetospheres, namely dynamical and centrifugal (rigidly rotating) magnetosphere (DM and CM). The top panel illustrates the condition $R_A < R_K$ which is valid for slowly rotating stars. In this case (DM), magnetically confined wind material falls back to the star on a dynamical time-scales (Sundqvist et al., 2012; Petit et al., 2013). On the other hand, the bottom panel shows the condition, $R_A > R_K$, for fast rotating stars. Here, the wind material trapped between R_A and R_K is supported by the centrifugal forces, which generates a rigidly rotating magnetosphere (CM) (Townsend & Owocki, 2005). However, regions within the R_K are still characterized as DM even for the fast rotators (Petit et al., 2013).

5.1.2 Photometric Variability

UHE and He II line problem white dwarfs reside on a narrow region in the HRD (see Fig. 5.8). Both are clearly separated from the hot subdwarf cloud and located on the top of the white dwarf cooling track. Other than their shared location in the HRD, both show a photometric variability rate of 75 % (Reindl et al., 2021). In addition, their period distribution, light curve shapes and amplitudes are similar. Due the to aforementioned reasons it was concluded that UHE and He II line problem white dwarfs are related (Reindl et al., 2021).

Reindl et al. (2021) showed that the period distribution of UHE and He II line problem white dwarfs is consistent with the orbital period distribution of post-common envelope binaries. Furthermore, they explained that the period distribution of their sample could be still in agreement with the rotational period distribution of magnetic white dwarfs, if it is considered that the white dwarfs in the sample are at the top of the white dwarf cooling track and as they cool down their radius will shrink further (Althaus et al., 2009). As a result of conservation of the angular momentum, the rotational speed of the stars will increase, which leads to a statistically meaningful agreement with the rotational period distribution of magnetic white dwarfs.

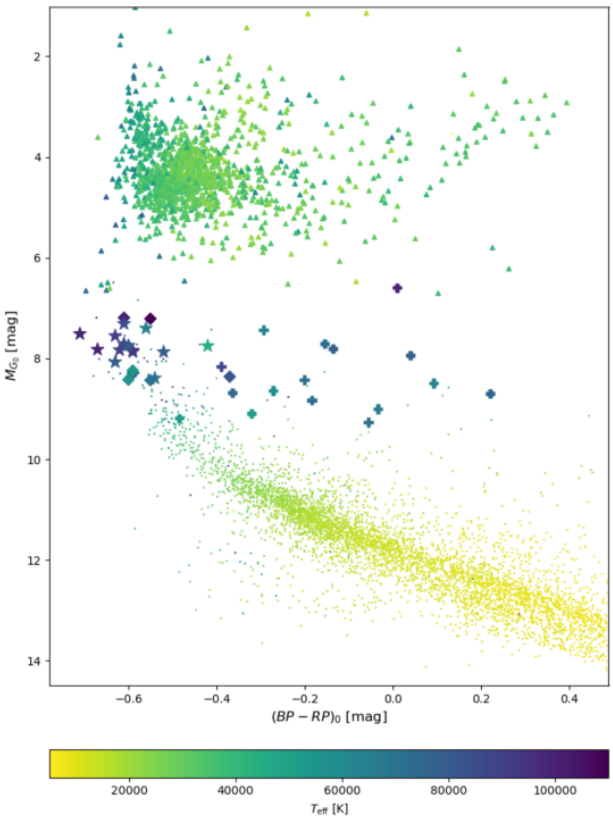

Figure 5.8: Location of the UHE white dwarfs (star symbols) and white dwarfs showing the He II line problem (diamonds) in the *Gaia* HRD. Triangle, dot, and plus symbols represent hot subdwarfs, SDSS white dwarfs, and hot white dwarfs ($T_{\rm eff} \geq 50\,000$ K) + main sequence binaries, respectively. Color coding shows the effective temperature of the stars. Taken from Reindl et al. (2021).

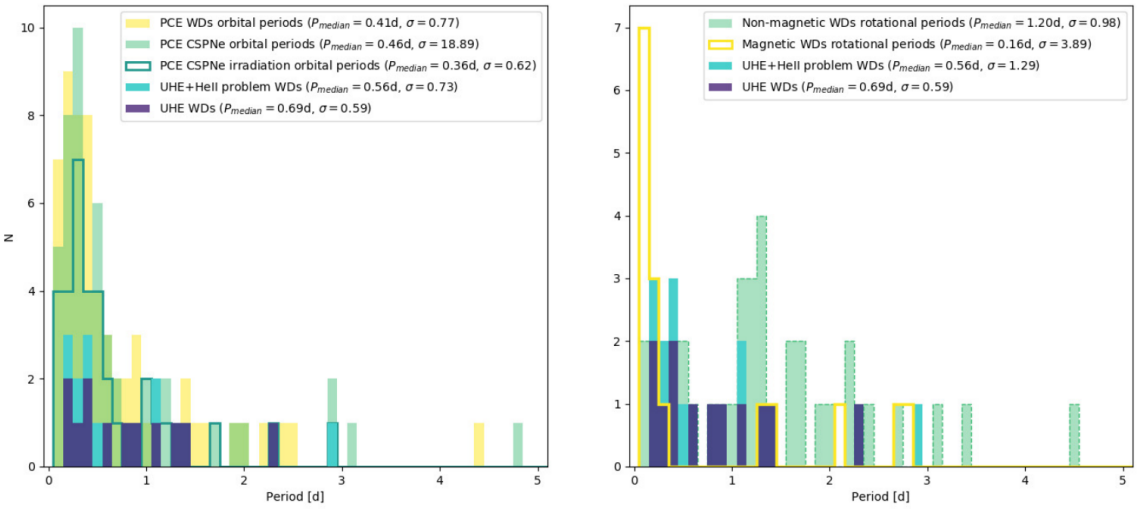

Figure 5.9: Period distribution of UHE and He II line problem white dwarfs compared to post-common envelope binaries, magnetic and non-magnetic white dwarfs. Taken from Reindl et al. (2021).

Since the photometric period of UHE and He II line problem white dwarfs are longer than nonradial g-mode pulsations that are observed in PG 1159 stars, Reindl et al. (2021) concluded that because of the good agreement with the period distributions, photometric variability should either be induced by magnetic fields or transpire as a result of binarity. They further explored reflection effect binaries as the source of the photometric variability. However, none of the objects in the sample shows an amplitude increase towards redder wavelengths in the light curve (Reindl et al., 2021). Furthermore, none of the sample spectra exhibit emission lines originating from the heated side of the cool companion, which was observed in reflection effect systems that consist of a hot white dwarf ($T_{\rm eff} \geq 60\,000$ K) and a cool companion (Reindl et al., 2021).

Reindl et al. (2019) have already demonstrated that the photometric variability of J0146+3236 can be explained with a bright spot model (see Fig. 5.4). In addition, the observed relatively large amplitude variations in the light curves can be described with chemical spots (Reindl et al., 2021) which were shown to be generated by magnetic fields and to cause periodic variations of spectral lines and light curves (Krtička et al., 2018, 2020). Finally, the theoretical light curves presented by Munoz et al. (2020) illustrated that the photometric variability observed in magnetic O-type stars can be explained with corotating circumstellar magnetospheres that are tilted with respect to the rotation axis (see Chapter 4.2.3). In fact, the synthetic light curves generated by these latter authors for the intermediate inclination and magnetic obliquity angles ($i \approx \beta \approx 50°$) can explain almost flat minima that were encountered in the light curves of seven of the stars in the sample of Reindl et al. (2021). Considering all of the aforementioned statements, Reindl et al. (2021) concluded that the photometric variability is most likely caused by weak magnetic fields and not binaries, however further investigations are needed.

5.2 The Goal of This Thesis

The goal of this thesis is to investigate the multi-band BUSCA light curves of some known UHE white dwarfs and archival light curves of two newly discovered objects, and to check their spectra for changes in the equivalent widths (EWs) and radial velocities (RVs) in order to provide more constraints on the mysterious nature of these objects. With the aforementioned methods, whether binarity or magnetic fields are the driving mechanism can be further explored. For the former scenario, it would be expected to detect larger amplitudes in the light curves for the redder bands compared to the bluer ones. In addition, close binarity can be revealed with statistically significant RV variations. For the latter scenario, the amplitudes measured in the light curves of different bands should be comparable to each other. Furthermore, it would be expected to detect EW variations only for photometrically variable objects and these EW variations would be expected to be correlated with their respective light curves.

6

Photometry

From the times when the naked eye was the primary optical instrument to modern days, the starlight has been the main source of information for the stargazers. Photometry is the technique that deals with the incoming light from the stars and traditionally it refers to visible light. Variable stars are discovered and studied by time-resolved photometry that allows us to inspect the brightness changes of the star over a period of time.

Photometry can be divided into two main categories: absolute and differential. By performing absolute photometry, the actual brightness of the object can be measured, whereas with the differential photometry, the relative flux of the object with respect to a comparison object can be obtained. However, absolute photometry is challenging because it requires a series of separate calibrations (first and second order extinction coefficient, transformation coefficient, zero point), therefore differential photometry is frequently employed.

To perform differential photometry, the target star and a few comparison stars are observed over a period of time (typically at least one full photometric period) with the same instrument and filter simultaneously. Then, dividing the light curve of the target by the ones of the comparison stars (see Fig. 6.1) results in the relative brightness variations of the target, which also corrects for the atmospheric effects.

While choosing the comparison stars, care must be taken though. Primarily, the comparison stars must not be variable since they can induce false variability to the target. Furthermore, it is desired that target and comparison stars are affected by the same air-mass and atmospheric conditions (clouds etc.). Since the target and the comparison stars are observed with the same exposure all at once, a substantial brightness difference may cause saturation. Also, different color indices might induce false variability since filters are used during the observation and different wavelengths are affected by the atmosphere diversely. However, the target stars in this study are amongst the bluest known stars and those are rare compared to redder stars. Hence, it is challenging to find comparison stars as blue as our targets.

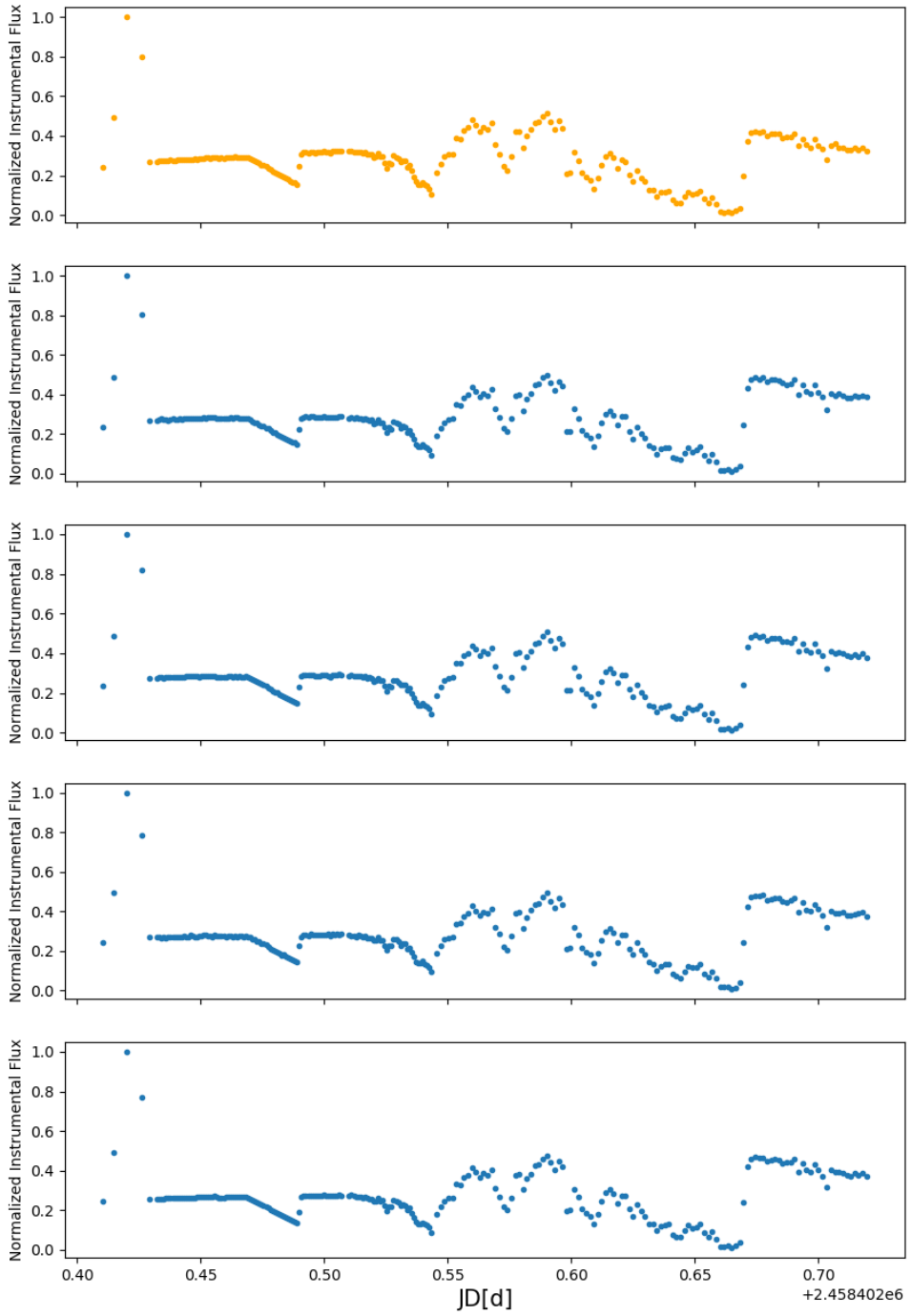

Figure 6.1: In the top panel the light curve of the target star (HS 0158+2335) is shown in orange. Below the light curves of the four comparison stars are shown in blue. The dips and scatters in the light curves are caused by the dominant atmospheric effects.

6.1 Observations

The objects HS 0727+6003, HS 0158+2335, HS 0713+3958, SDSSJ121523.08+120300.7, as well as the comparison stars, were observed using the Bonn University Simultaneous Camera (BUSCA; Reif et al., 1999) at the 2.2 m telescope of the Calar Alto Observatory. The beamsplitters of BUSCA (see Fig. 6.2) allow us to collect visible light simultaneously in four different bands namely U_B, B_B, R_B, and I_B. Due to technical problems with BUSCA, no data in I_B for the objects HS 0727+6003 and HS 0158+2335 could be obtained. In Table 6.1 observation dates as well as observing conditions are listed. In addition, archival data (Catalina Sky Survey, TESS, ATLAS, and ZTF; Larson et al., 2003; Ricker et al., 2015; Tonry et al., 2018; Masci et al., 2019) of two newly discovered objects J0706+6134 and J0702+0514 were analysed in this study.

Calar Alto BUSCA Observations			
Name	Exposure Time	Observation Date	Comment On Observation
HS 0158+2335	60s, 120s, 180s	10.10.2018	Partly cloudy
HS 0158+2335	120s	21.12.2018	A few cirrus
HS 0158+2335	120s	22.12.2018	Cirrus and moonlight diffusion
HS 0727+6003	100s	21.12.2018	A few cirrus
HS 0727+6003	80s	22.12.2018	Cirrus and moonlight diffusion
HS 0713+3958	150s	14.01.2019	Thin cirrus, affected by time of opportunity program
HS 0713+3958	250s, 300s, 400s	15.01.2019	Thin cirrus, affected by time of opportunity program
J1215+1203	840s	14.01.2019	Thin cirrus, affected by time of opportunity program
J1215+1203	600s, 840s	15.01.2019	Thin cirrus, affected by time of opportunity program

Table 6.1: Observing conditions of the targets.

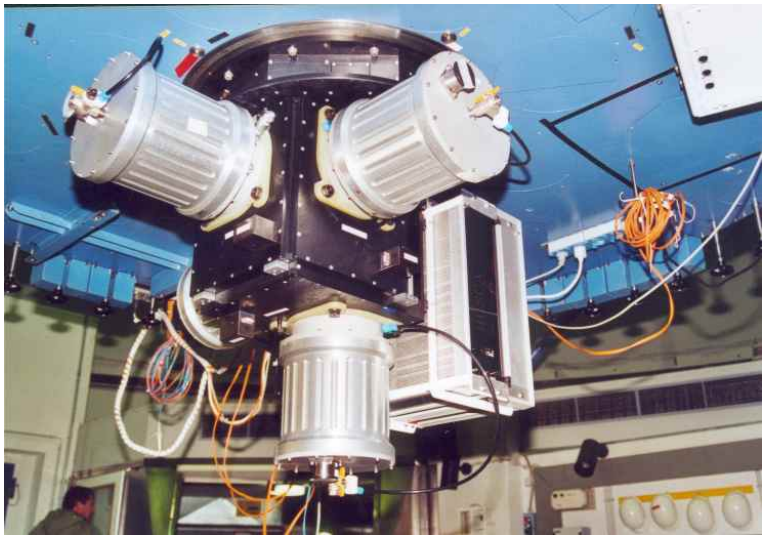

Figure 6.2: BUSCA with its four CCD systems mounted at the mirror cell of the 2.2m telescope. Copyright: CAHA

6.2 Data Reduction

Raw images come along with defects that cause noise in the data. In this regard noise is any unwanted signal that is embedded in the image caused by the electronic instrument, imperfections in the optics, and cosmic rays. For this purpose, the Image Reduction and Analysis Facility (IRAF) is an important tool that was developed by the National Optical Astronomy Observatories (NOAO). IRAF supplies a range of data reduction and photometric analysis tools for astronomical data, though it was also used in other scientific fields for the purpose of general image processing. This software runs in the terminal and consists of different software packages. Additional packages can be installed in form of scripts dependent on the purpose of the study.

Bias Correction

A CCD is an electronic detector that consists of photosensitive cells called "pixels". Ideally, each photon that strikes a pixel should produce an electron which can be counted by an *analog-to-digital converter* (ADC). However, it is not the case in practice. Random fluctuations in the readout electronics introduce a type of noise called *readout noise*. This means that even if every pixel in the CCD accommodates the same amount of electrons, due to readout noise, the number of electrons can be different. This can be solved by applying a constant bias voltage before analog-to-digital conversion. However, this must be corrected before doing photometry. A bias frame is a 0-s exposure, with the shutter closed. In that case, the camera goes to a read cycle without being exposed to any light. Therefore, any noise due to the reading process can be measured. It is advised to take multiple bias images and average or median combine them in order to eliminate any readout discrepancy and cosmic ray influence. For this purpose IRAF's *zerocombine* task can be utilized, creating a *masterbias* frame. Then this masterbias frame is subtracted from raw images to discard the noise.

Dark Correction

CCD pixels are semi-conductor capacitors and generally produced from silicon. If the silicon in the CCD is much above the absolute zero i.e room temperature, it will generate *thermal noise* or *dark current* due to atoms in the material colliding with each other and creating free electrons. Cooling down the instrument cause the atoms to move slowly and decrease the collision between atoms, hence less free electrons and less thermal noise. In order to discard any noise due to the dark current, dark frames are used. However dark frames can not eliminate all the noise generated by the dark current, because the thermal noise is not a fixed value. A dark frame is taken shutter closed, at the same temperature and with the same exposure time as raw science frames. Multiple dark frames should be taken. Then the set of images can be average or median combined into *masterdark* frame by using IRAF's *darkcombine* task. Masterdark image should be subtracted from raw science images as it was done with masterbias.

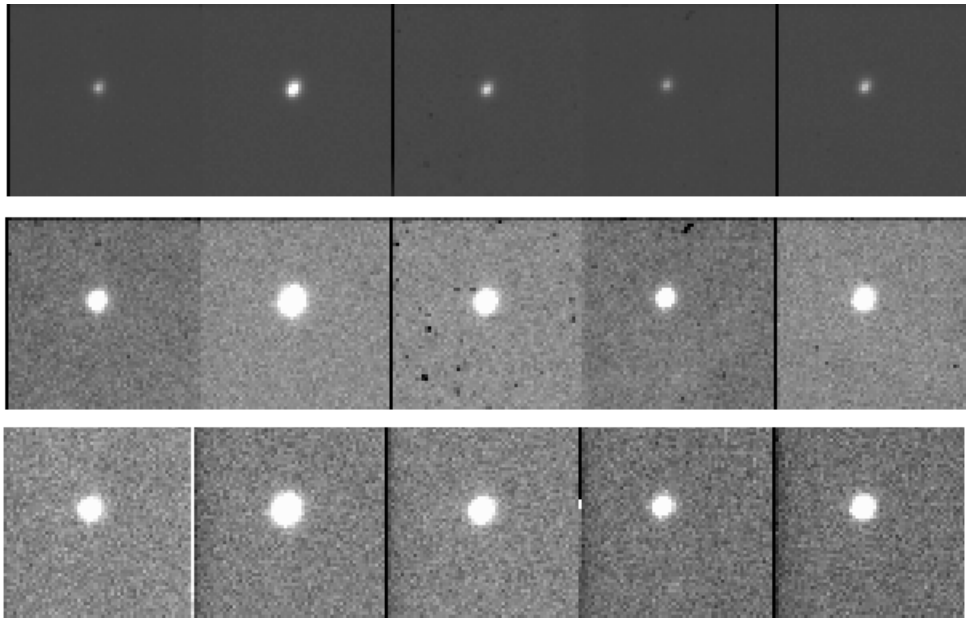

Figure 6.3: The top panel shows raw science images, the middle panel shows bias corrected science images and the bottom panel shows bias and flat corrected science images.

Flat Correction

Not all pixels can be manufactured evenly. Some pixels can be more or less sensitive than others. In addition, problems in the optical path such as dust particles on the filter or camera, nonuniform illumination of pixels due to the telescope aperture being circular and arrays being rectangular should be corrected as well. This can be solved to some extent by taking a flat frame. Multiple flat frames should be taken while the camera is exposed to uniform light. For this purpose, flat frames are taken in twilight (sky flats) or by lighting inside of the telescope dome (dome flats) when the dome is closed. Due to flat frames being affected by the bias voltage, they need to be first bias-corrected. Then, bias-corrected flat frames can be combined by using IRAF's *flatcombine* task. Unlike bias and dark correction, bias-corrected science frames should be divided by the obtained *masterflat* frame.

All of the aforementioned reduction processes except dark reduction [1] have been performed by using a pipeline as an external package for IRAF.

6.3 Aperture Photometry

Aperture photometry is a simple yet important technique. It is done by setting an aperture (approximately 3-4 times the full width half maximum (FWHM) of the point spread function (PSF)) around the target, with the aim of collecting as much light from the target as possible. However, by summing all the signal in this area, the pixels within the set aperture, not only the signal from the target but also the signal from the sky background is collected. To avoid the background signal, a *sky annulus* is set and the signal is measured. Then, the measured pixel value in the annulus is subtracted from the

[1] Because of the efficient nitrogen cooling of BUSCA dark frames were not needed.

measured pixel value in the aperture. In that way, the background-corrected flux from the source can be calculated.

For the aperture photometry of target and the comparison stars, IRAF's *phot* task in the *daophot* package was utilized. The *phot* task comes with default parameter values. In order to use the *phot* task with the desired parameters, parameters should be edited with the *datapars*, *centerpars*, *fitskypars* and *photpars* tasks that are included in the *daophot* package. To correct all stars for the effects of atmospheric disturbance in a similar way, differential photometry was performed. In order to obtain the target flux without the effects of the atmosphere, the target flux was divided by the sum of the comparison star fluxes. Then the target flux was normalized by dividing each data point by the mean value of the target flux. By using IRAF's *hedit* command, the observation time was extracted as *Julian Date* from the FITS file headers.

6.4 Light Curve Analysis with VARTOOLS

VARTOOLS (Hartman & Bakos, 2016) is a command line program that is used for time-series data, mainly for light curves. This software supports the processing of light curves i.e. signal identification, filtering, light curve manipulation, time conversions, modeling and simulating of light curves.

First of all, the obtained Julian Dates (JDs) were converted to Heliocentric Julian Dates (HJDs) by using the *-converttime* command. This conversion is necessary to correct for differences in the Earth's position with respect to Sun. In addition, to phase all data together the *-phase* command was used. Moreover, by using the *-killharm* command a harmonic series of the form

$$m_0 + \sum_{i=1}^{N_P} a_{i,1} \sin(2\pi f_i t) + b_{i,1} \cos(2\pi f_i t) \tag{6.1}$$

was fitted to each phased light curve and a harmonic series of the form

$$m_0 + \sum_{i=1}^{N_P} \Big\{ a_{i,1} \sin(2\pi f_i t) + b_{i,1} \cos(2\pi f_i t) + \sum_{k=2}^{N_{harm,i}+1} [a_{i,1} \sin(2\pi k f_i t) + b_{i,1} \cos(2\pi k f_i t)] \Big\} \tag{6.2}$$

was fitted to the light curve of HS 0158+2335 to achieve a better fit. The peak-to-peak amplitudes for all the light curves were calculated as the difference between the maximum and minimum of the fit. The uncertainties on the amplitudes were estimated by calculating the standard deviation via $std = \sqrt{(observed - fit)^2}$. To determine the period, a generalized Lomb-Scargle search (Zechmeister & Kürster, 2009) was performed. With the *-LS* command periodic sinusoidal signals were searched. If more than one significant period were detected, the original data were whitened by removing the most significant signal and the periodogram was recalculated. The false alarm probability (FAP) is the probability to detect a primary signal even though there is no signal. In that sense smaller values of the FAP refer to more accurate detections of the primary signal. If log(FAP) is $\leq$ -4, the object is classified as significantly variable.

6.5 Results

6.5.1 HS 0158+2335

In Fig. 6.4 the fitted light curves of HS 0158+2335 are shown. The observations of HS 0158+2335 do not cover a full photometric period. Nonetheless, the maximum and the minimum of the light curve could be recorded. The amplitudes and standard deviation of the target object for the U_B, B_B, R_B are calculated as 0.267 ± 0.010 mag, 0.211 ± 0.010 mag and 0.193 ± 0.011 mag, respectively. In Fig. 6.4, it can be clearly seen that U_B-band observations are affected by the air-mass. While the flux levels in the B_B- and R_B-band increases after HJD 258402.671856, the U_B-band flux level remains constant. Thus, the U_B-band amplitude must not be trusted. The amplitudes measured in the B_B- and R_B-band agree with what is reported by (Reindl et al., 2021) from the ATLAS, CSS, and ZTF light curves.

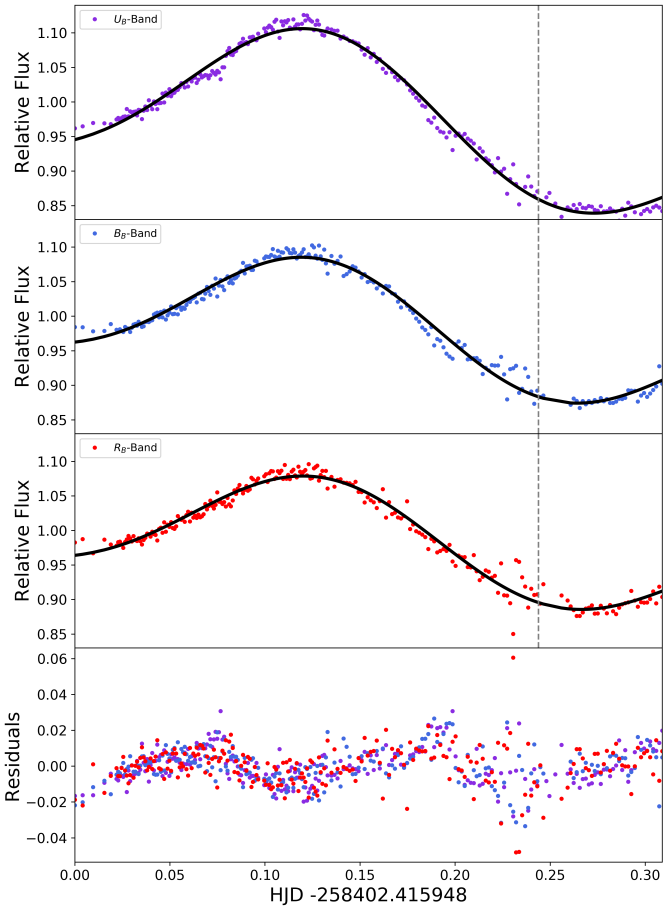

Figure 6.4: Fitted light curves of HS 0158+2335 for U_B, B_B, and R_B-band. The grey dashed lines indicate after which time the air mass exceeded 1.3

6.5.2 HS 0727+6003

HS 0727+6003 was observed covering almost two photometric phases and it is the only object that was observed more than once. In Fig. 6.5, the heliocentric corrected and fitted light curves of HS 0727+6003 are shown. The data taken in the shaded regions where the air mass exceeds 1.3 were excluded from the phased light curves, since in Fig. 6.5 it can be clearly recognized that the observation conditions became worse when the air mass exceeded 1.3. In Fig. 6.9, the phase-folded and fitted light curves of HS 0727+6003 are shown. A generalized Lomb-Scargle (LS) search for periodic sinusoidal signals was performed for HS 0727+6003 (See Fig. 6.6, 6.7, 6.8). The periods from the U_B, B_B, and R_B light curves were calculated as 0.218811, 0.221077 and 0.221577 d, respectively. Fitting a harmonic series to the phase-folded light curve, amplitudes of 0.128 ± 0.014 mag, 0.131 ± 0.008 mag and 0.128 ± 0.011 mag are obtained for U_B, B_B, and R_B respectively. The amplitudes from the different bands agree with each other.

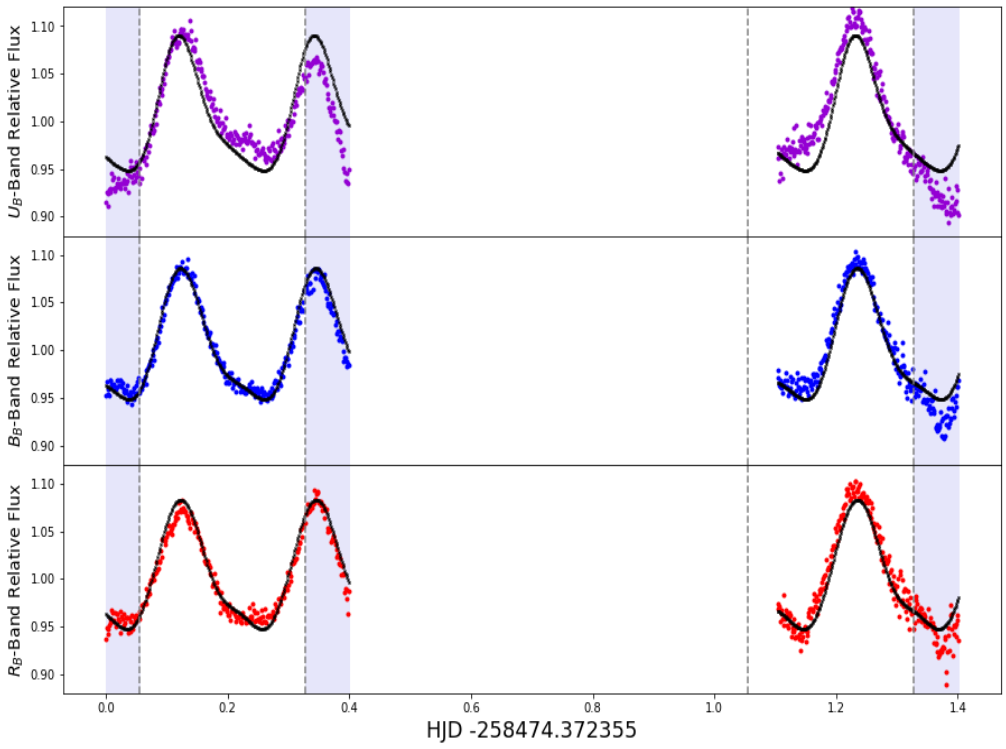

Figure 6.5: Light curves of HS 0727+6003 for the U_B, B_B, and R_B-band. The shaded regions indicate an air mass more than 1.3.

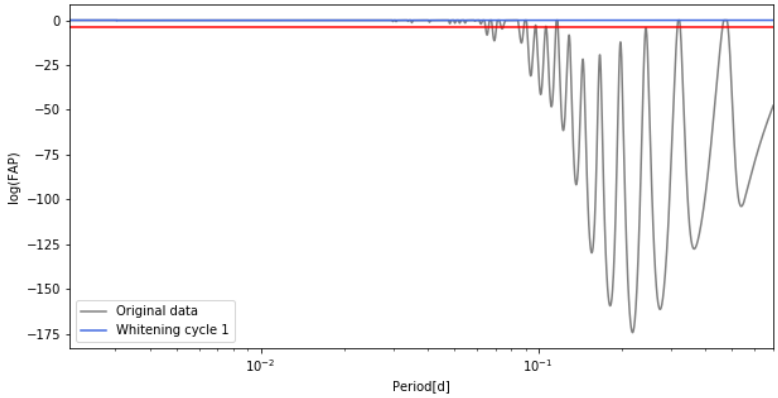

Figure 6.6: U_B-band Lomb-Scargle Periodogram of HS 0727+6003. The grey lines show the periodogram of the original data, whereas the blue lines represent the data after the first whitening cycle. The red line corresponds to log (FAP) =-4.

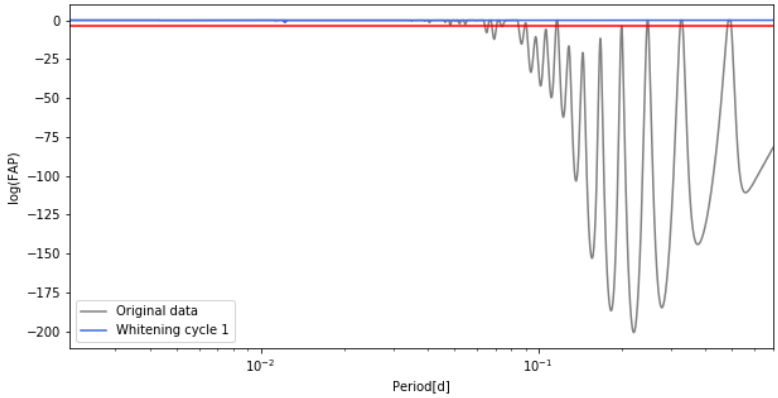

Figure 6.7: B_B-band Lomb-Scargle Periodogram of HS 0727+6003. The grey lines show the periodogram of the original data, whereas the blue lines represent the data after the first whitening cycle. The red line corresponds to log (FAP) =-4.

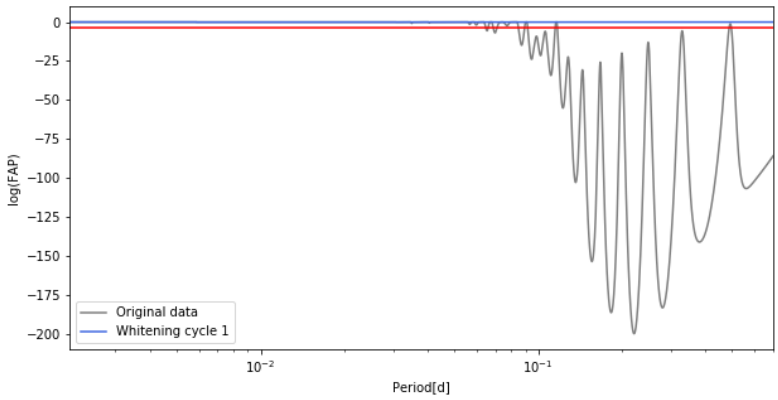

Figure 6.8: R_B-band Lomb-Scargle Periodogram of HS 0727+6003. The grey lines show the periodogram of the original data, whereas the blue lines represent the data after the first whitening cycle. The red line corresponds to log (FAP) =-4.

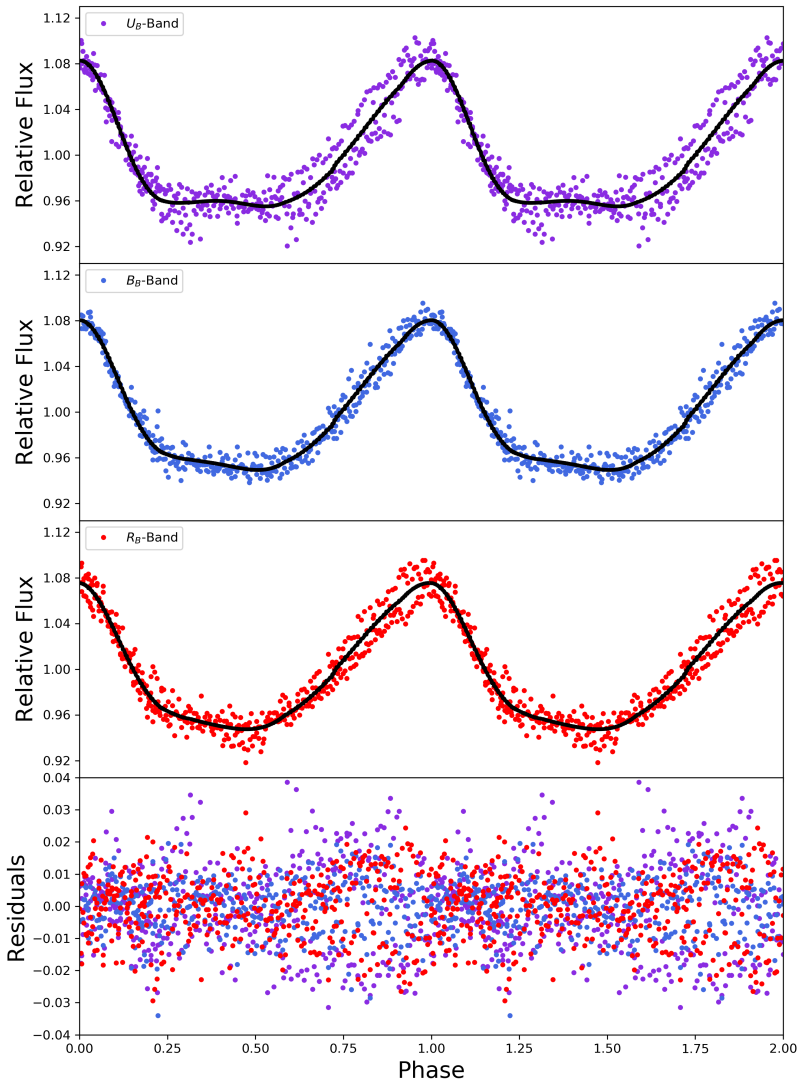

Figure 6.9: Phase folded and fitted light curves of HS 0727+6003 in the U_B, B_B, and R_B-bands.

6.5.3 HS 0713+3958 & J1215+1203

The observations of HS 0713+3958 and J1215+1203 in January were affected by a "Time of Opportunity" program, therefore not enough data points could be collected to acquire a meaningful light curve. In that case, the amplitude calculation was not possible for those two stars.

6.5.4 J0706+6134

J0706+6134 was observed with TESS, ATLAS, ZTF and CSS (see Fig. 6.10 and 6.11). The periodogram of the TESS light curve shows the strongest peak around 0.37 d. The periods from ATLAS o, ZTF g , ZTF r- band periodograms agree with the TESS results. All of the aforementioned light curves were phase-folded according to their respective periods. The CSS periodogram shows the strongest peak around 0.07 d. However, the second strongest signal is nearly as strong as the first one and is around 0.37 d. After the first whitening cycle, the second strongest signal vanishes which implies that the 0.07 d period is an alias of the 0.37 d period. For that reason, CSS light curves were phased according to the second strongest signal which is in agreement with the other light curves. ATLAS c-band observations do not have sufficient data points, thus it was not possible to acquire a significant signal. That being the case, the ATLAS c-band light curve was phased according to the TESS period. The calculated amplitudes and periods are listed in Table 6.2. All of the amplitudes agree with each other except the ATLAS c-band, but this could be due to insufficient data points of the ATLAS c-band light curves.

J0706+6134		
Band	Period [d]	Amplitude [mag]
ATLAS c	-	0.017 ± 0.010
ATLAS o	0.37356692	0.051 ± 0.011
CSS	0.37374771	0.034 ± 0.014
ZTF g	0.37375853	0.036 ± 0.017
ZTF r	0.37375390	0.041 ± 0.011
TESS	0.37372668	0.038 ± 0.011

Table 6.2: Periods and amplitudes of the respective light curves of J0706+6134.

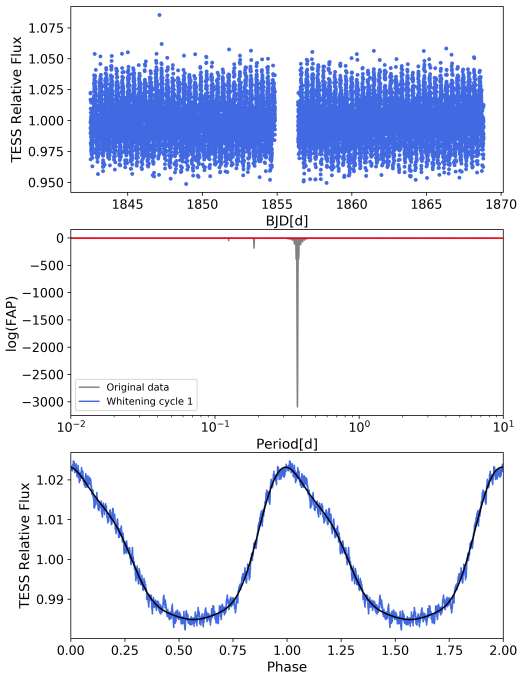

(a) TESS

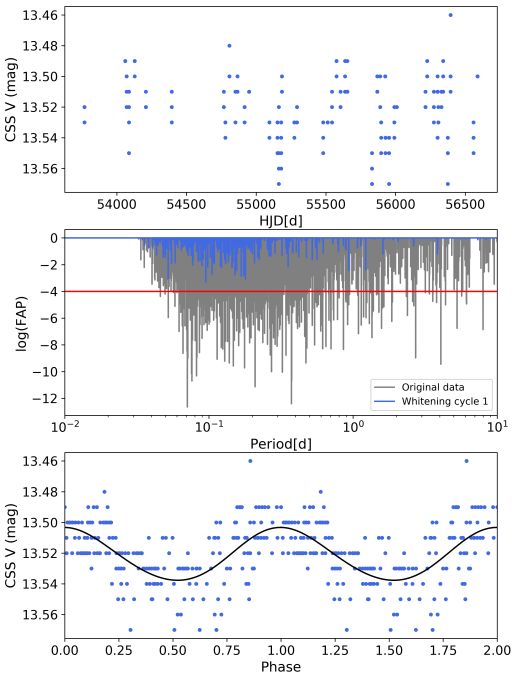

(b) CSS

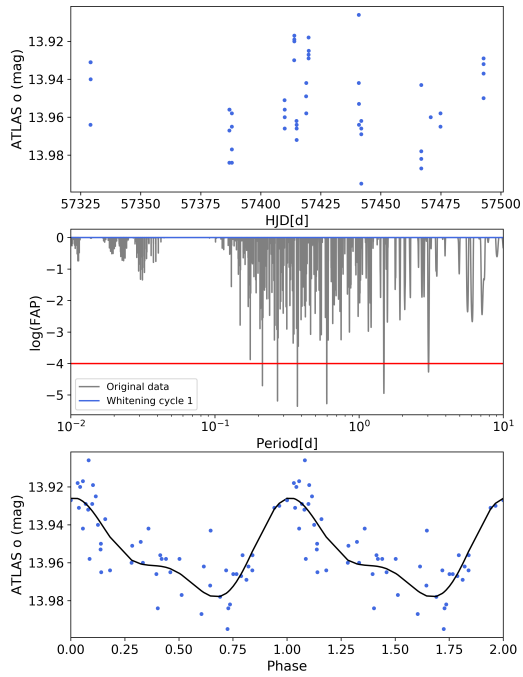

(c) ATLAS o

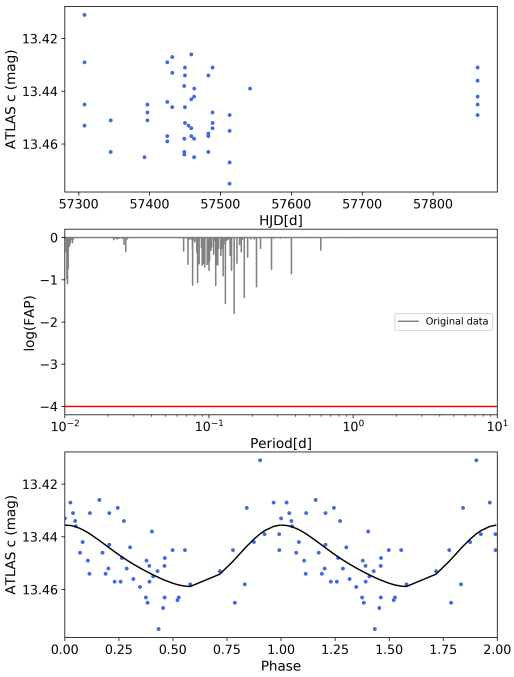

(d) ATLAS c

Figure 6.10: Original data (top panel), periodograms (middle panel) and phase-folded light curves (bottom panel) of the UHE WD J0706+6134. The red line in the middle panel indicates log(FAP) = -4.

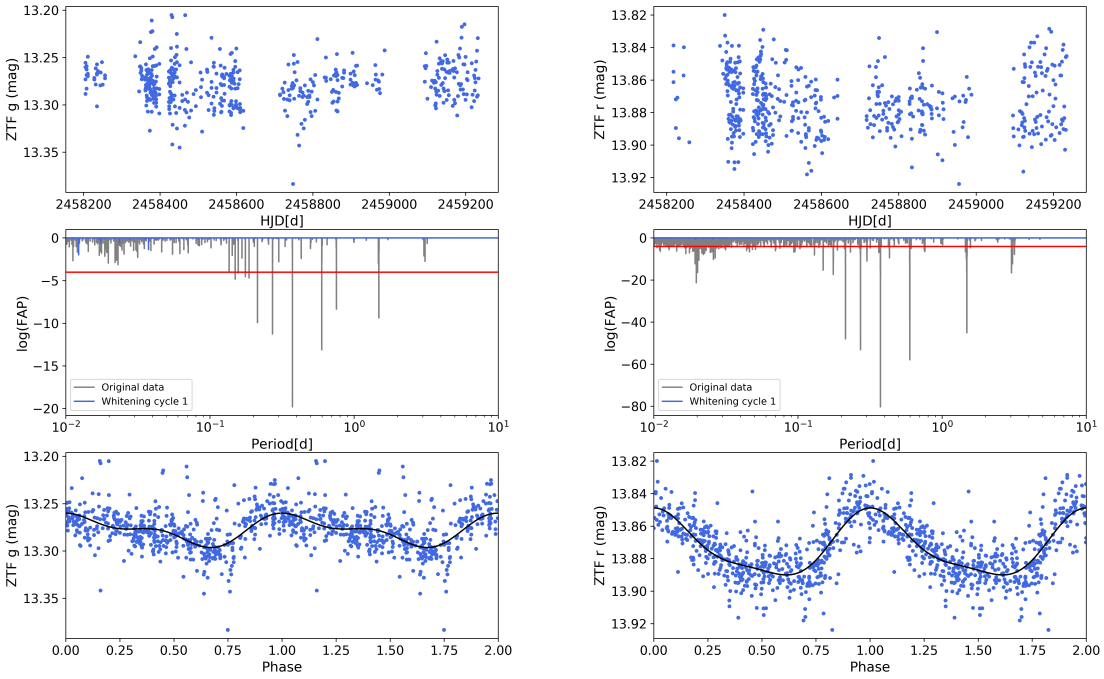

(a) ZTF g (b) ZTF r

Figure 6.11: Original data (top panel), periodograms (middle panel) and phase-folded light curves (bottom panel) of the UHE WD J0706+6134. The red line in the middle panel indicates log(FAP) = -4.

6.5.5 J0702+0514

J0702+0514 was observed with TESS, ATLAS, and ZTF (see Fig. 6.12 and 6.13). The periodogram of the TESS light curve shows the strongest signal around 0.598 d (see Fig. 6.12). The periods obtained in the ATLAS c, ATLAS o, ZTF g , ZTF r- bands agree with the TESS result. All of the aforementioned light curves are phase-folded according to their respective periods. In addition, calculated peak to peak amplitudes from different bands agree witch each other. Calculated amplitudes and periods are listed in Table 6.3.

J0702+0514		
Band	Period [d]	Amplitude [mag]
ATLAS c	0.59761885	0.079 ± 0.037
ATLAS o	0.59760948	0.089 ± 0.032
ZTF g	0.59761314	0.081 ± 0.016
ZTF r	0.59759873	0.082 ± 0.011
TESS	0.59771361	0.092 ± 0.007

Table 6.3: Periods and amplitudes of the respective light curves of J0702+0514.

6.6 Discussion

The light curve analysis of several UHE white dwarfs in the sample revealed different light curve shapes. The light curves of HS0727+6003 and J0702+0514 show almost flat photometric minima which could be explained with both the reflection effect and the circumstellar magnetosphere with an intermediate inclination and magnetic obliquity angle ($i \approx \beta \approx 50°$). However, for none of the objects in the sample, the amplitudes measured in different bands do increase towards redder wavelengths which would indicate reflection effect systems. On the other hand, no amplitude change in different bands is expected for the magnetosphere model. In addition, the TESS light curve of J0706+6134 reveals an asymmetrical light curve shape which can not be explained with binarity. Whereas, a deformed or asymmetrical magnetosphere can explain the observed asymmetry in the light curve.

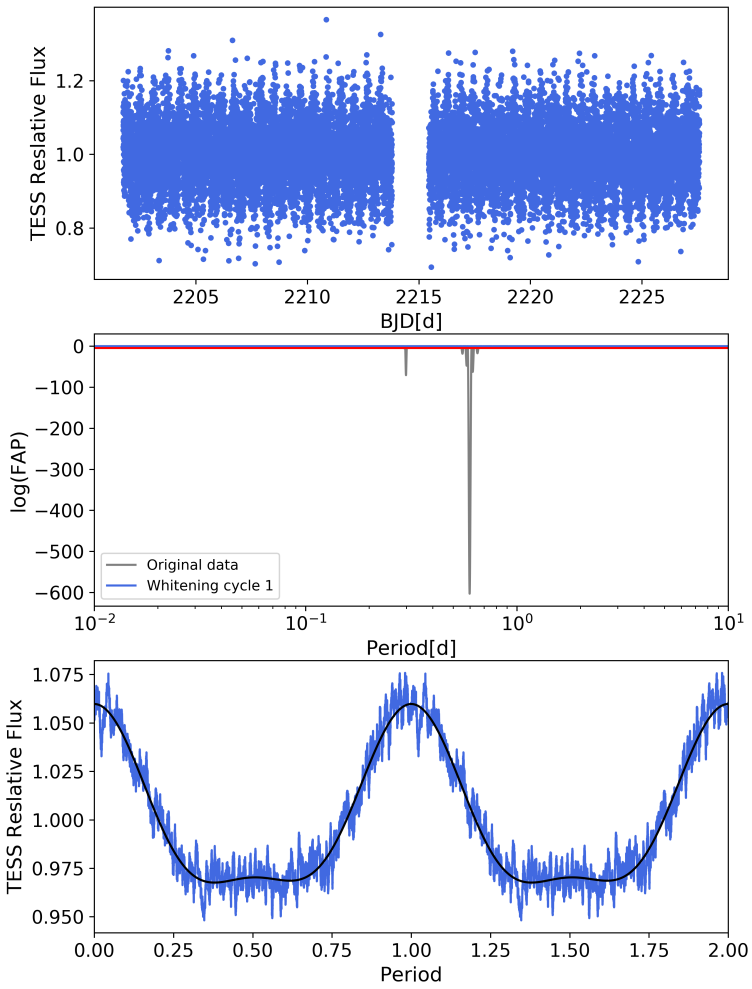

Figure 6.12: TESS Original data (top panel), periodogram (middle panel) and phase-folded light curve (bottom panel) of the UHE WD J0702+0514. The red line in the middle panel indicates log(FAP) = -4.

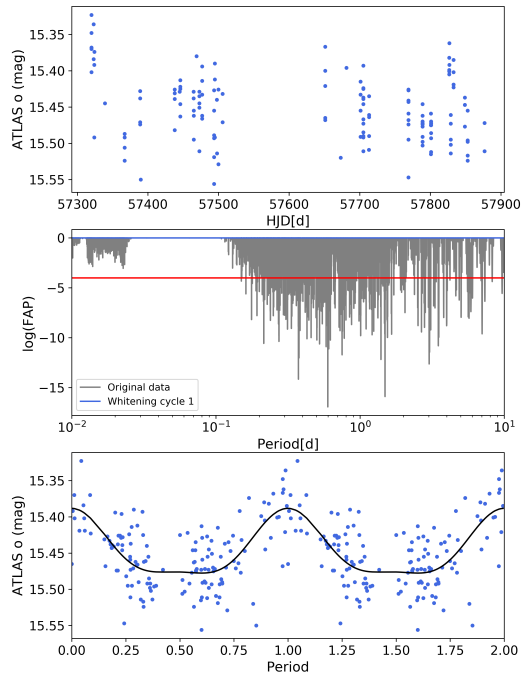

(a) ATLAS o

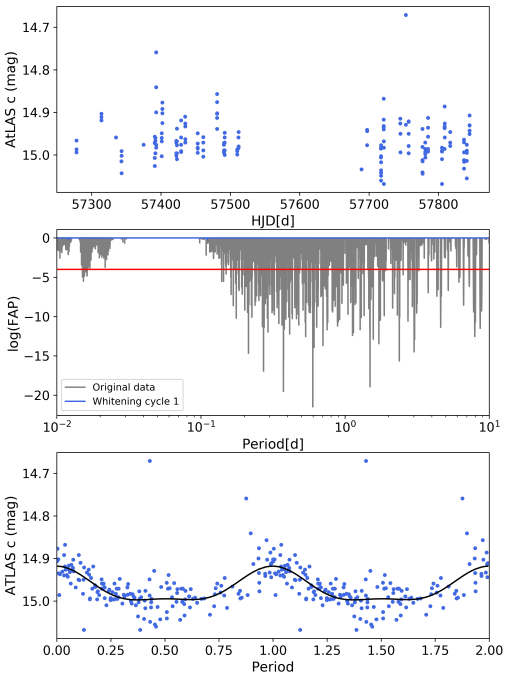

(b) ATLAS c

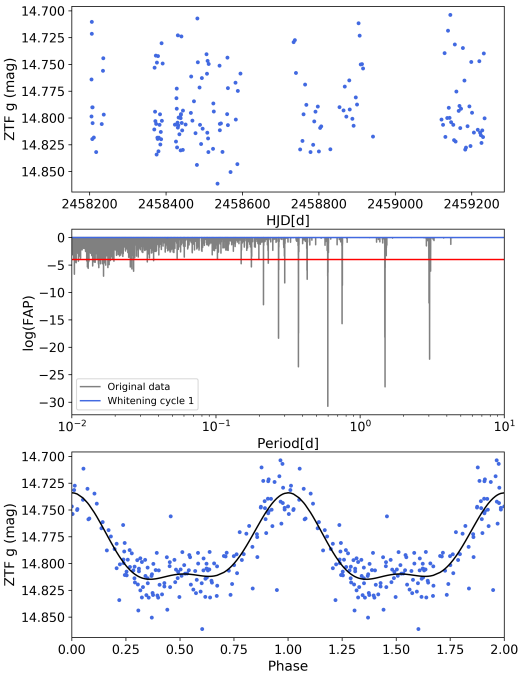

(c) ZTF g

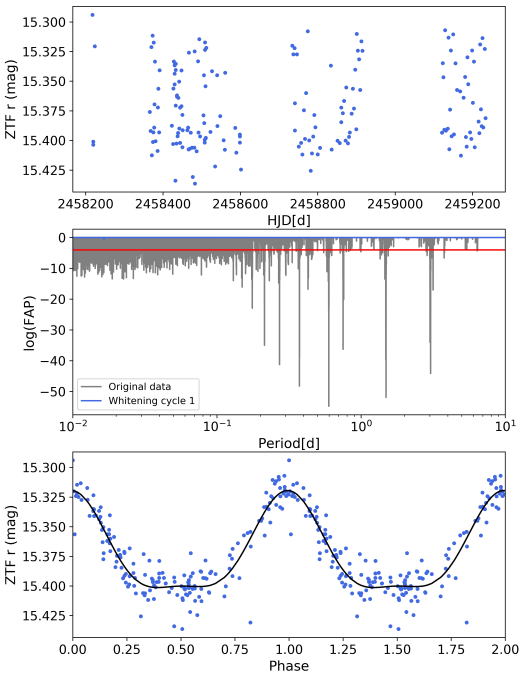

(d) ZTF r

Figure 6.13: Original data (top panel), periodograms (middle panel) and phase-folded light curves (bottom panel) of the UHE WD J0702+0514. The red line in the middle panel indicates log(FAP) = -4.

7

Equivalent Width Inspection

As mentioned in section 6, the incoming light from a star is the main information source of that object. Although a great deal about the stars can be studied with photometry, in order to determine the physical parameters such as surface gravity and temperature spectroscopy is needed. Moreover, spectroscopy is the only tool that allows us to study element abundances of a star as well as measuring the radial velocity. Spectroscopic data require the same reduction processes as photometric data, however, in addition a wavelength calibration is essential which is done with a calibration (i.e. Th/Ar) lamp. Flux calibration of the spectra is also performed when necessary. For the spectral observations, exposure times are usually of the order of several minutes so that a sufficient signal to noise ratio (S/N) can be achieved.

The energy radiated by the stars is not the same in all parts of the electromagnetic spectrum. This results in a peak in the continuum which is determined by the surface temperature of the star. Since our target stars are among the hottest known white dwarfs ($T_{\text{eff}} > \sim 60$ kK), their continuum peak lies in the UV range of the electromagnetic spectrum.

With the circumstellar magnetosphere model, it would be expected to see a similar correlation between the light curves and equivalent widths (EWs) of the photometrically variable objects which was observed in J0146+3236. Reindl et al. (2019) remarked that strength changes in the UHE lines are only expected if the magnetic axis of the star is inclined to the rotation axis. However, if the magnetosphere is not obliquely rotating, neither photometric nor EW variations are expected to be observed, meaning that the photometrically non-variable objects are not expected to show EW changes. Thus, in this chapter the potential variation of the equivalent widths of selected UHE lines and their correlation to their respective light curves are investigated.

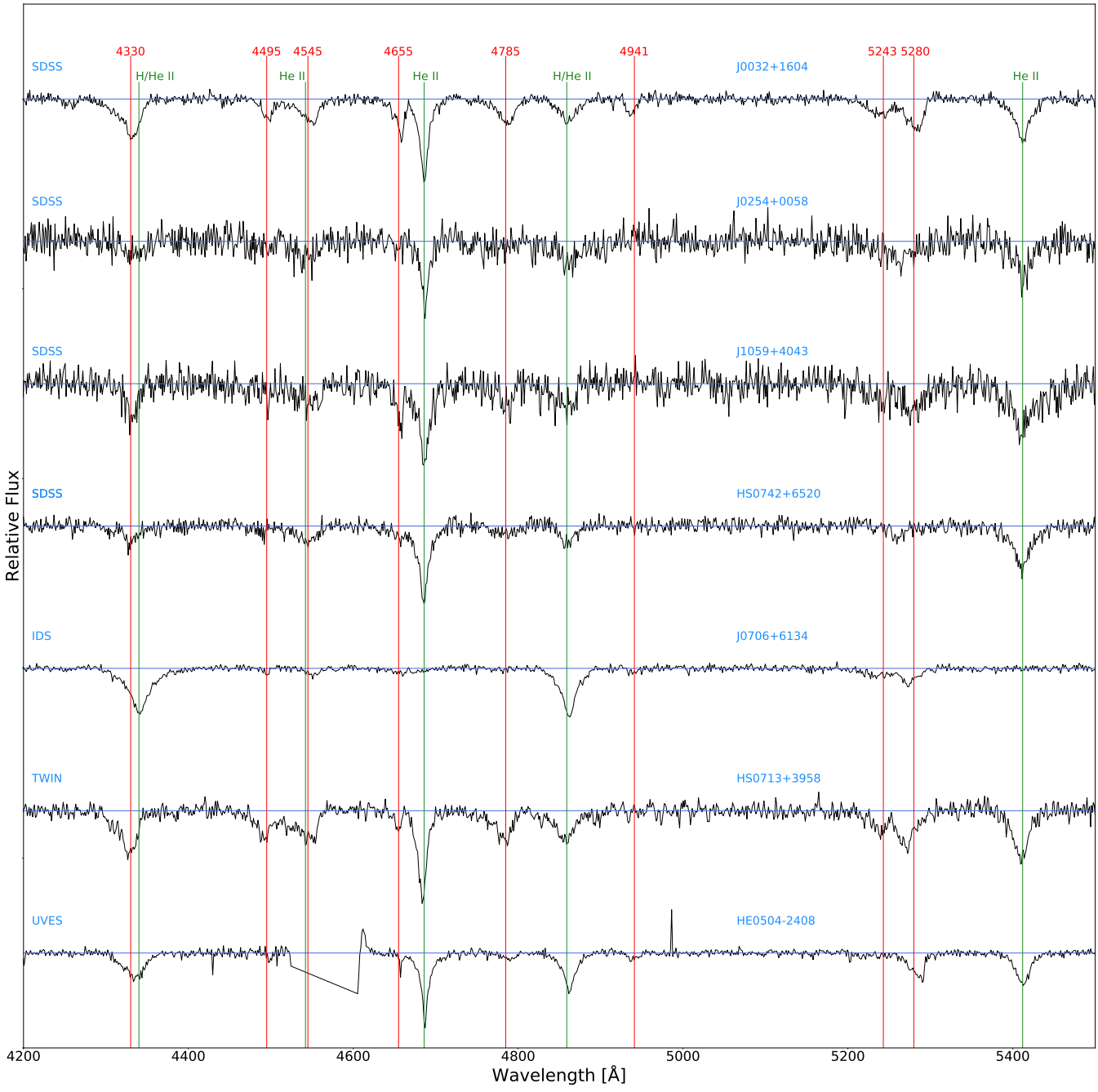

Figure 7.1: Selected normalized spectra of UHE white dwarfs. Red lines represent the ultra-high excitation lines. Green lines indicate H and/or He II lines.

7.1 Observations & Data

The UHE white dwarfs HS 0158+2335, HS 0713+3958, HS 0727+6003, J0146+3236 and HE 1314+0018 were observed using The Cassegrain Twin Spectrograph (TWIN) at the Calar Alto 3.5m telescope (R≈3000). J0706+6134 and J0702+0514 were observed with the Intermediate Dispersion Spectrograph (IDS) at the Cassegrain Focal station of the 2.5m Isaac Newton Telescope and the spectra have a resolving power of R≈1452. Furthermore, archival spectra (R≈1800) from the Sloan Digital Sky Survey (SDSS; Smee et al., 2013; Alam et al., 2015) were used for this study. SDSS spectra consist of several subspectra which were taken with a typical exposure time of 900 s. WD0101-0182 and HE 0504-2408 were observed within the SPY survey (Napiwotzki et al., 2001) and the spectra (R≈18500) were taken with the Ultraviolet and Visual Echelle Spectrograph (UVES; Dekker et al., 2000) mounted on the Very Large Telescope (VLT) located at the Nasmyth B focus of the Unit Telescope 2 (UT2). All spectroscopic observations of the UHE and He II line problem white dwarfs are listed in Tables 9.1 and 9.2 with the object name, the file name of the spectroscopic observation, spectrograph, mid exposure Barycentric Julian Day (BJD) of the observation, exposure time, and S/N.

The data reduction processes of the TWIN and UVES spectra were explained in Reindl et al. (2021). The IDS spectra were reduced with IRAF. After the bias and flat correction, 2D images were converted to 1D spectra and a wavelength calibration were performed by using the arc lamp exposures. Since SDSS spectral data are kept in vacuum wavelengths ($\lambda_{\rm vac}$), they needed to be converted to air wavelengths ($\lambda_{\rm air}$). For this calculation the International Astronomical Union (IAU) conversion from air to vacuum wavelengths published by Morton (1991) was used.

$$\lambda_{\rm air} = \frac{\lambda_{\rm vac}}{1.0 + 2.735182 \times 10^{-4} + \left(\frac{131.4182}{\lambda^2_{\rm vac}}\right) + \left(\frac{2.76249\times10^8}{\lambda^4_{\rm vac}}\right)} \tag{7.1}$$

7.2 Line Identifications

UHE absorption lines are considered as Rydberg lines of ionized metals in ionization stages V-X, with α and β transitions between Rydberg states $n - n'$ (Werner et al., 2018a). It is not possible to exactly identify which element generated a particular UHE line, however, UHE lines probably originate from C, N, O and Ne (Werner et al., 1995). In Table 7.1, all of the UHE features that are present in the spectra of our sample are shown.

Table 7.1: UHE features in the sample. y/n/p indicates whether the line is present or not, ? indicates that the S/N of the observation is too low to judge, and - indicates that the spectroscopic observation do not cover this wavelengths range.

Name / λ / Å	3872	4082	4330	4495	4545	4655	4785	4941	5243	5280	5655	6060	6198	6477	6901	7610	7717	7915	8192
J0032+1604	y	y	y	y	y	y	y	y	y	y	y	y	y	y	y	y	y	y	y
WD0101-182	y	n	y	-	-	y	y	n	y	y	-	p	n	n	-	-	-	-	-
J0146+3236	y	y	y	y	y	y	y	y	y	y	y	y	?	y	-	-	-	-	-
HS 0158+2335	y	n	n	n	n	?	n	n	x	x	y	n	?	n	n	n	?	n	?
J0254+0058	y	n	y	y	y	y	y	n	x	x	y	y	n	y	n	y	?	y	?
HE 0504-2408	y	n	y	y	y	y	y	y	n	y	y	y	y	y	-	-	-	-	-
HS 0713+3958	y	y	y	y	y	y	y	y	y	y	y	y	y	y	?	y	y	y	y
HS 0727+6003	y	n	y	n	n	?	n	n	?	y	y	n	n	y	-	-	-	-	-
HS 0742+6520	y	n	y	n	n	y	?	n	x	x	y	y	y	y	n	y	y	y	y
J0900+2343	n	n	n	?	?	n	n	n	y	y	y	?	?	?	?	?	?	?	?
J1059+4043	y	y	y	y	y	y	y	n	y	y	y	y	?	y	n	y	y	y	y
J1215+1203	y	n	y	y	y	y	y	?	y	y	y	y	?	y	n	y	y	y	?
J1257+4220	n	n	n	n	?	n	n	?	p	y	y	n	n	n	?	?	?	?	?
J1510+6106	n	n	n	n	n	n	n	n	?	?	n	n	n	n	n	n	n	n	n
HS 2027+0651	y	n	n	y	n	y	n	n	y	y	y	y	n	n	n	n	y	n	n
HS 2115+1148	y	n	n	y	y	y	n	y	y	y	y	n	y	y	-	-	-	-	-
WDJ0706+6134	y	n	n	y	y	y	n	y	y	y	y	y	y	n	y	-	-	-	-
WDJ0702+0514	y	n	y	y	y	n	y	n	y	y	y	y	n	y	y	-	-	-	-
J0821+1739	n	n	n	n	n	n	n	n	x	x	n	n	n	n	n	y	y	?	?
J0827+5858	n	n	n	?	n	n	n	?	x	x	y	n	n	n	n	n	n	n	n
J0947+1015	n	n	n	n	n	n	n	?	x	x	?	n	n	n	n	n	n	n	n
J1029+4043	n	n	n	n	n	n	n	n	?	?	n	n	n	n	n	n	n	n	n
HE 1314+0018	n	n	n	n	n	n	n	n	?	?	n	n	n	n	n	n	n	n	n
HS 1517+7403	n	n	n	n	n	n	n	n	n	n	n	n	x	n	n	n	n	n	n
J1512+0651	n	n	n	n	n	n	n	n	?	?	n	n	n	n	-	-	-	-	-

7.3 Continuum Normalization

A continuous spectrum represents mainly thermal radiation of a star in all wavelengths without any opacity sources (i.e absorption lines). Besides the continuous spectrum, actual stellar spectra contain other elements like absorption and emission lines, noise caused by the instrument and artifacts like cosmic rays.

The continuum normalization process can be described as bringing the observed spectrum to unity via dividing it by the observed continuum. However, care must be taken during this process since the contaminants near the target line i.e cosmic rays, noise and too weak absorption lines might complicate predicting where the actual continuum/spectral line starts and ends. Continuum normalization can be employed with polynomial interpolation of the estimated continuum which means basically fitting a suitable order of a polynomial and dividing the data set by it. Considering the fact that stellar spectra data sets are not perfect mathematical functions, utilizing polynomial interpolation would generate higher error margins. Another method that can be utilized is spline interpolation of the data set. In this method, spline functions composed of lower order polynomials are fitted to small intervals of data points. As a result, the overall data set is better represented mathematically.

In order to normalize the obtained spectra, spline interpolation of the data points was employed and the data set was divided by a spline fit by using Python. All of the known absorption lines were excluded from this interpolation so that only the continuum could be brought to unity and the spectral lines could be maintained unaffected. This procedure was applied to all of the the target stars and an example of the normalization process for J0032+1604 is shown in Fig. 7.2.

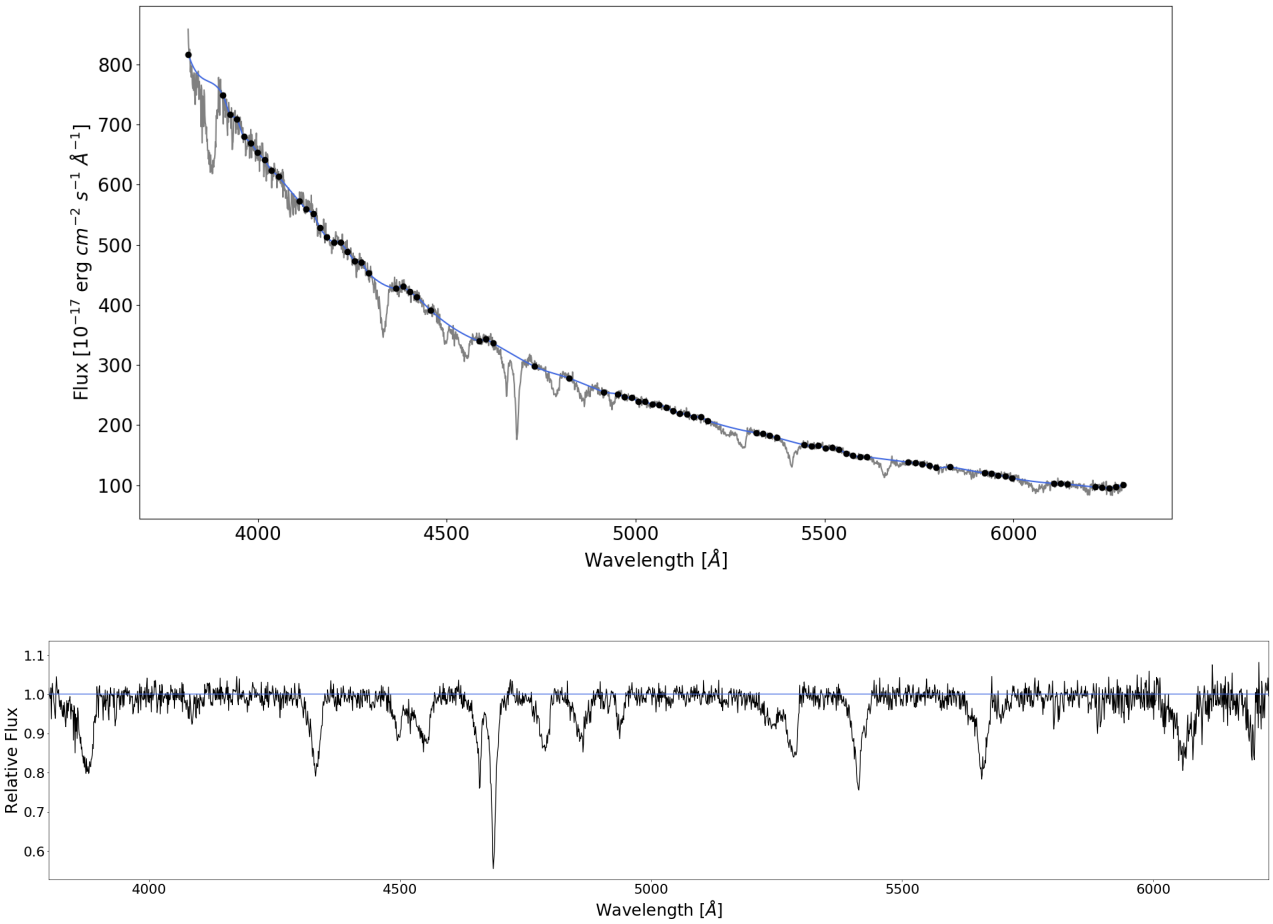

Figure 7.2: The top panel shows spline interpolated (blue) SDSS spectrum (grey) of J0032+1604. Black dots represent spline anchors. The bottom panel shows normalized SDSS spectrum of J0032+1604

7.4 Equivalent Width Calculation

The equivalent width (EW) of a spectral line - in the most simple way - can be explained by forming a hypothetical rectangle with an area A that has the same area as the spectral line and equal length to the continuum flux F_0. As a result the width of this rectangle gives the EW in wavelength units (see Fig. 7.3).

$$A = F \times EW \tag{7.2}$$

EWs are measured to analyse chemical abundances of stars. Moreover, with time resolved spectroscopy one can gain insight into variations of a particular spectral line. However, the determination of the continuum influences the measurement of the EWs. Hence, correct continuum normalization is crucial for this process. It has been observed that positioning of anchor spline points has a definite effect on the determination of the line strength and as a consequence the EW. Hence, it should be determined carefully. However, it has been noted that low S/N spectra in this case give poor results and the calculated EWs are not reliable.

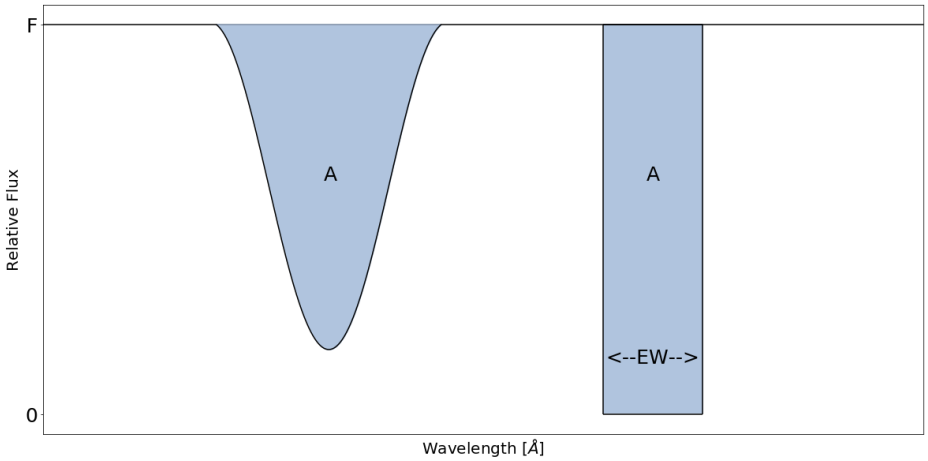

Figure 7.3: Equivalent Width

The EWs W_λ of the UHE lines 4785 Å, 5243+5380 Å, 5655 Å and 6060 Å as well as the He II lines 5412 Å[1] and 6560 Å[2] were calculated by using the definition

$$W_\lambda = \int_{\lambda_1}^{\lambda_2} \frac{F_c(\lambda) - F(\lambda)}{F_c(\lambda)}\, d\lambda \tag{7.3}$$

where W_λ, $F_c(\lambda)$, and $F(\lambda)$ are the equivalent width, flux in the continuum and flux in the line, respectively. Aforementioned UHE and He II lines were chosen since they're not blended with nearby lines. Vollmann & Eversberg (2006) show that Eq. 7.3 can be written as

$$W_\lambda \approx \Delta\lambda \cdot \left[1 - \frac{\overline{F}}{\overline{F_c}}\right] \tag{7.4}$$

where $\Delta\lambda = \lambda_2$ - λ_1.

First of all, a prominent region ($\Delta\lambda$) for each absorption line was chosen (see Fig. 7.4). Then $\overline{F}$ and $\overline{F_c}$ were determined for each spectrum by using Python's *NumPy* package and W_λ was calculated with Eq. 7.4 for the selected absorption lines. Reindl et al. (2019) used Voigt profile models to calculate UHE and He II lines of J0146+3236. However, UHE lines are not well represented with Voigt profiles due to their asymmetrical shapes. The He II lines of J0146+3236 (especially the He II line at 5412 Å) show that Voigt profiles are not a good fit either for the He II lines of UHE white dwarf spectra. For that reason, calculating EWs with measurable quantities like $\overline{F}$ and $\overline{F_c}$ gives more reliable results.

[1] Not present in DA type white dwarf spectra
[2] Hα for DA type white dwarfs

The standard deviation $\sigma(W_\lambda)$ for the EW measurement (Vollmann & Eversberg, 2006) was calculated with

$$\sigma(W_\lambda) = \sqrt{1 + \frac{\overline{F_c}}{\overline{F}}} \cdot \frac{(\Delta\lambda - W_\lambda)}{S/N} \tag{7.5}$$

where S/N is the signal to noise ratio. The S/N of the spectra were calculated by using DER_SNR: A simple and general spectroscopic signal-to-noise measurement algorithm developed by Felix Stoehr, ESO.

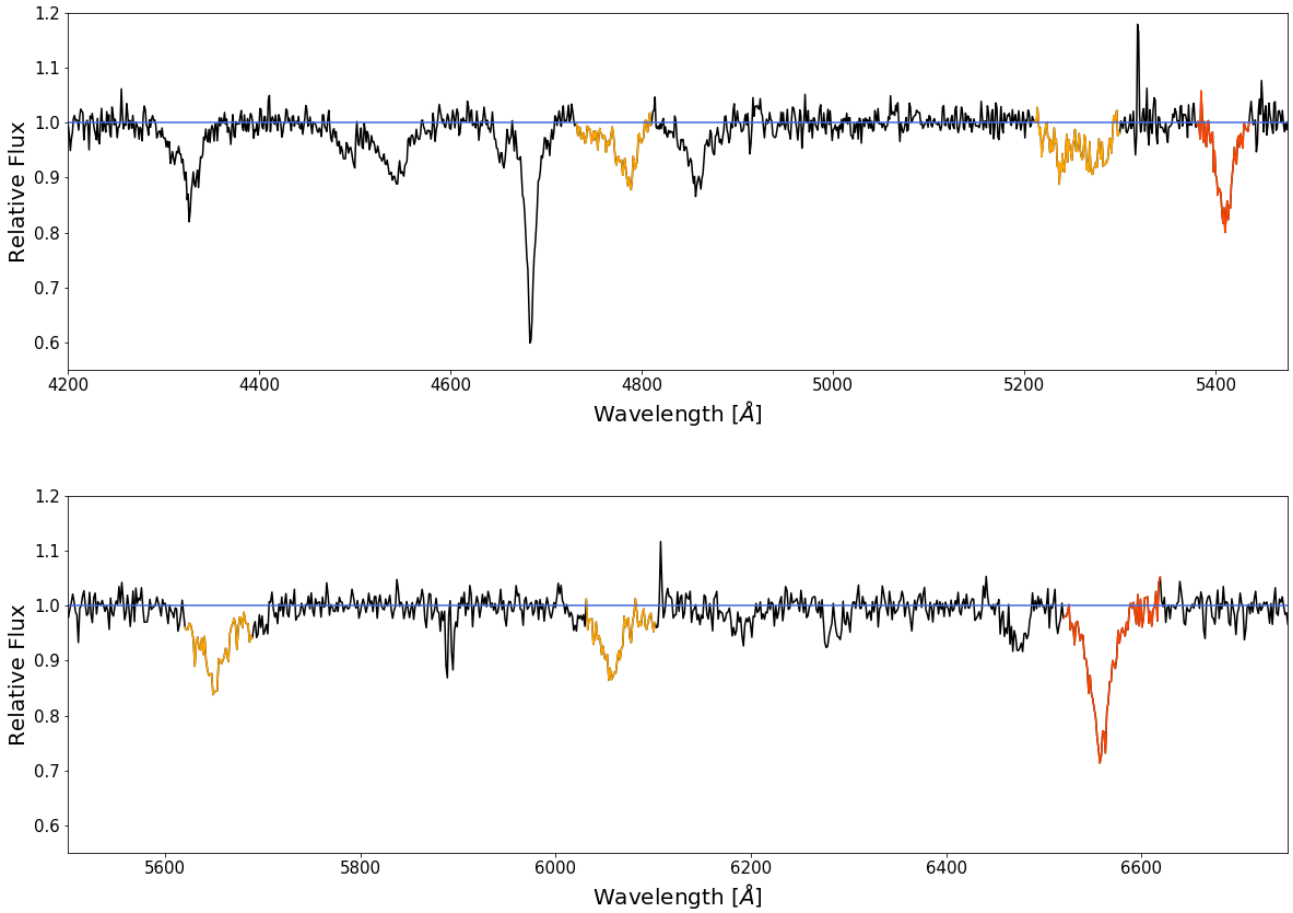

Figure 7.4: Selected regions for the UHE lines (orange) at 4785 Å, 5243+5280 Å, 5655 Å, 6060 Å and the He II lines (red) at 5412 Å and 6560 Å in one of the TWIN spectra of J0146+3236.

7.5 Equivalent Width Variation

Most of the SDSS spectra have a very low S/N and as a consequence, the calculated EWs are not reliable especially for the weak lines. Therefore, the EWs were not measured for five of the stars with multiple but poor quality spectra. In addition, most of the spectroscopic data sets of a particular star do not cover a full phase. That being the case, the EW variations of only HS 0742+6520 are shown from the SDSS spectra, however the red SDSS sub-spectra for this object still have very low S/N. To examine the changes of the EWs and the correlations with their light curves, the mid-observation Julian Dates (JDs)

of the spectra were barycentrically corrected (BJD). For this purpose the *Astropy* package in Python was utilized. After acquiring the BJDs, a Lomb-Scargle search for periodic signals with *-LS* command of VARTOOLS was employed. This procedure was applied to EW variation curves of each selected UHE and He II line of the photometrically variable objects for which we have a good phase coverage (J0146+3236, HS 0713+3958 and HS 0158+2335). Among the three selected objects, only the periodogram of J0146+3236 shows a significant peak (P = 0.242530 d, log(FAP) = -4.434) for only the EW variation of the UHE features at 6060 Å which agrees with the photometric period (P = 0.242037 d) reported by Reindl et al. (2021). Since for only one object and only one line a significant period could be found, the EW variation curves of J0146+3236, HS 0713+3958 and HS 0158+2335 were phased to the photometric periods that were published by Reindl et al. (2021) with the *-phase* command of VARTOOLS.

The EW variations of the selected lines as a function of the photometric phase are shown in Figs. 7.5, 7.6, and 7.7 for J0146+3236, HS0713+3958, and HS0158+2335, respectively. Furthermore, the UVES and IDS spectra of the variable objects WD0101-182 and J0706+6134 do not have a good phase coverage. Therefore, phasing these objects was not possible and the EW changes of these object were plotted by number of spectra (see Figs. 7.9, and 7.8). The same procedure was employed for the non-variable objects HS 0742+6520 and HE 0504-2408 (see Figs. 7.10, 7.11, respectively).

Reindl et al. (2019) reported a correlation between the photometric period and EW changes of J0146+3236. In Fig. 7.5, the same correlation for J0146+3236 is reproduced as well. The variation of the UHE features at 6060 Å shows a clear similarity with the light curve of this object. In addition, a similar correlation can be seen for the UHE lines at 4785 Å and 5655 Å. However, no significant variations in the EWs of the He II lines are detected.

Although changes in the EWs for HS 0713+3958 are expected because it is a photometrically variable object, it is not possible to infer a correlation with its light curve because the variations are statistically not significant (see Fig. 7.6). Moreover, more than seven spectra were affected by cosmics on the UHE lines which contributes to the uncertainty of the EW variations. The calculated error bars are too high due to low S/N spectra.

HS 0158+2335 (see Fig. 7.7) shows EW variations. However, these variations are not statistically significant. The spectra of HS 0158+2335 have one of the lowest S/N among the shown objects and as a consequence come with the largest error bars. With better S/N, variations of the UHE and the He II lines of HS 0158+2335 can be more accurately explored further.

No significant changes in the EWs of J0706+6134 are detected (see Fig. 7.8). However, this could have been arisen due to the first three consecutive spectroscopic observations of J0706+6134 being performed within just about 60 min and a possible overlap with the phase of final observation (2 nights later). WD0101-182 (see Fig. 7.9) shows no significant

changes in the EWs, however there are only two spectra for this object. Hence it is not possible to reach a conclusion.

For HS 0742+6520 (see Fig. 7.10), no significant EW changes can be seen. This could be due to HS 0742+6520 having one of the lowest S/N spectra. HE 0504-2408 also does not show a significant EW variation. However, in Fig. 7.11 it can be seen that EWs calculated from the first spectrum of HE 0504-2408 have quite high error bars due to its poor S/N. As expected from the photometrically non-variable objects, no significant changes in the EWs of HS 0742+6520 and HE 0504-2408 are detected.

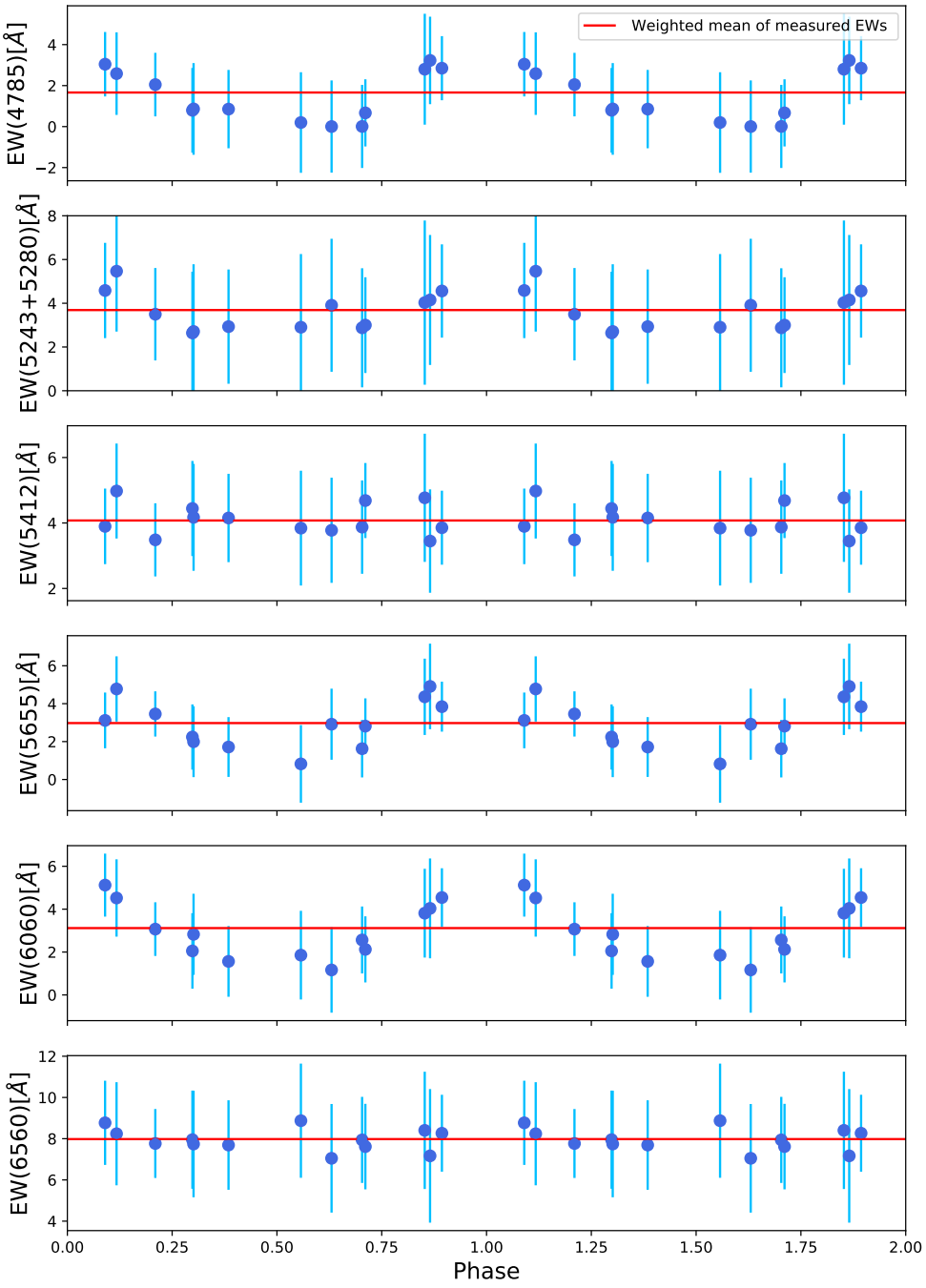

Figure 7.5: EW variations of J0146+3236 as a function of photometric phase. Blue dots, light blue lines, and red lines represent the EW, the standard deviation in EW measurements, and the weighted mean of the EW values for the respective line, respectively.

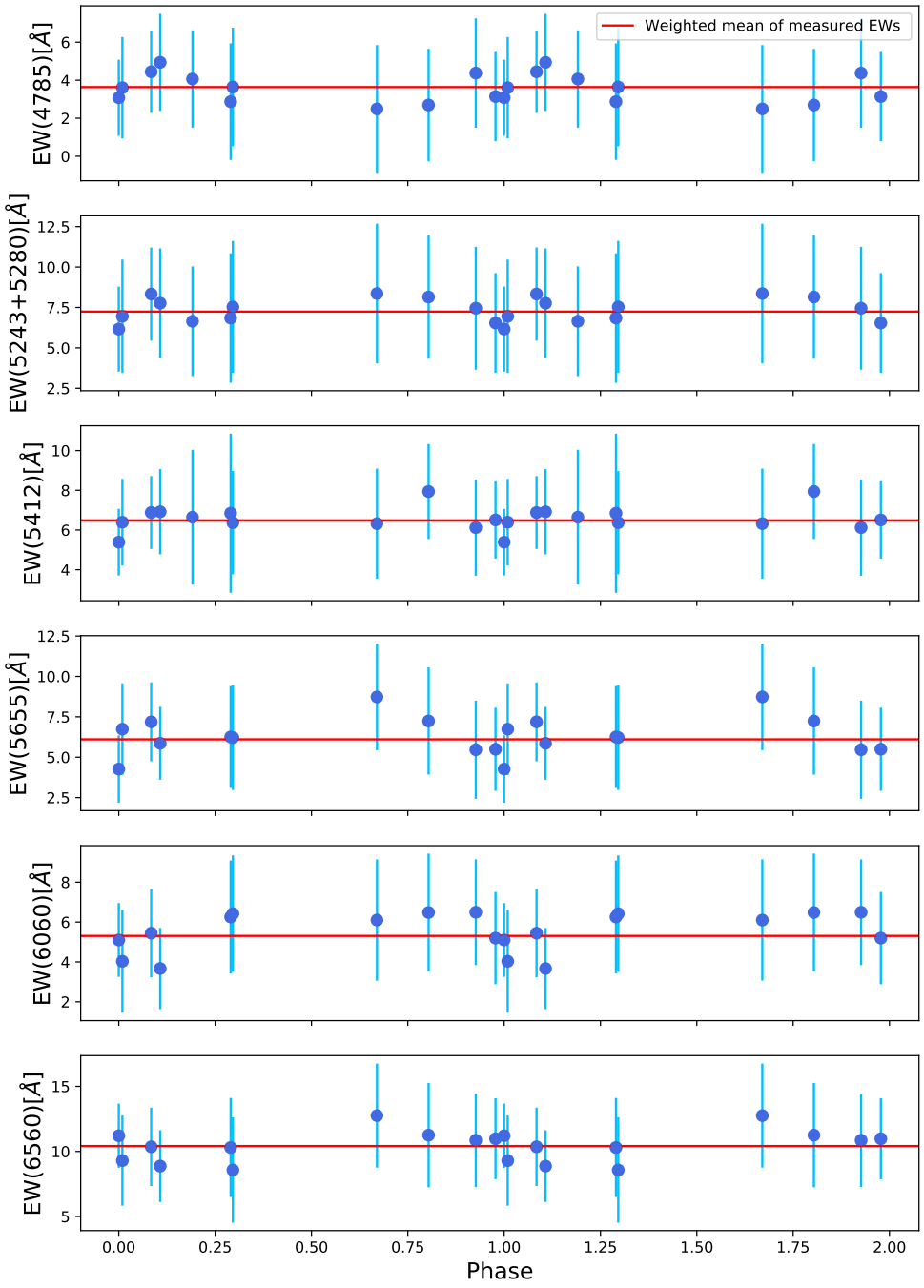

Figure 7.6: EW variations of HS 0713+3958 as a function of photometric phase. Blue dots, light blue lines, and red lines represent the EW, the standard deviation in EW measurements, and the weighted mean of the EW values for the respective line, respectively.

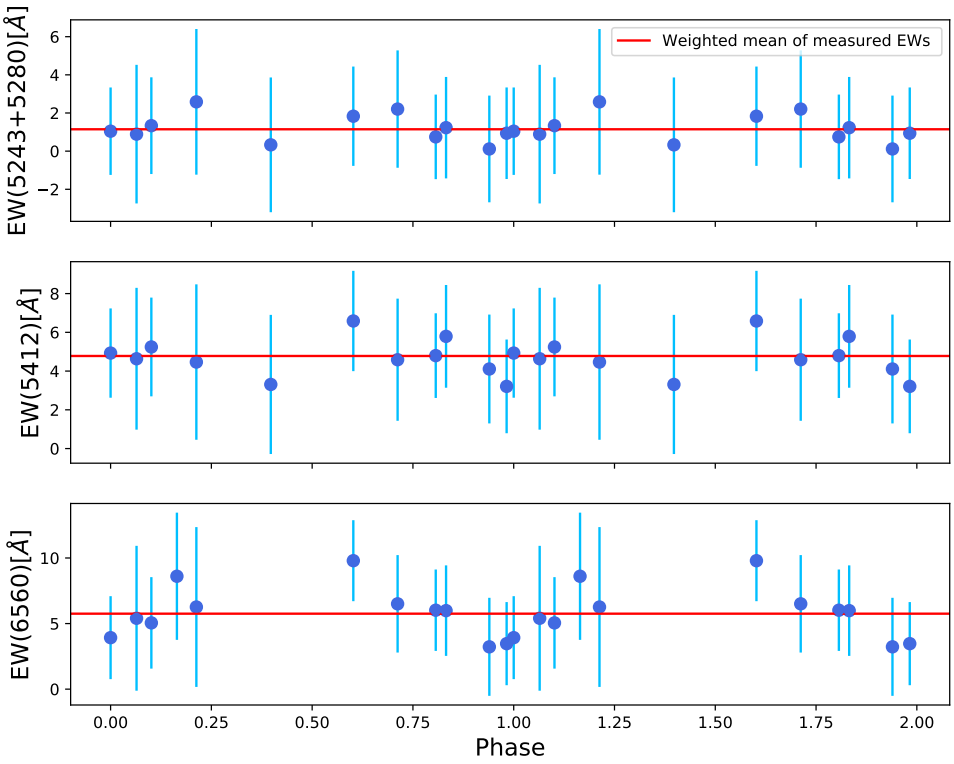

Figure 7.7: EW variations of HS 0158+2335 as a function of photometric phase. Blue dots, light blue lines, and red lines represent the EW, the standard deviation in EW measurements, and the weighted mean of the EW values for the respective line, respectively.

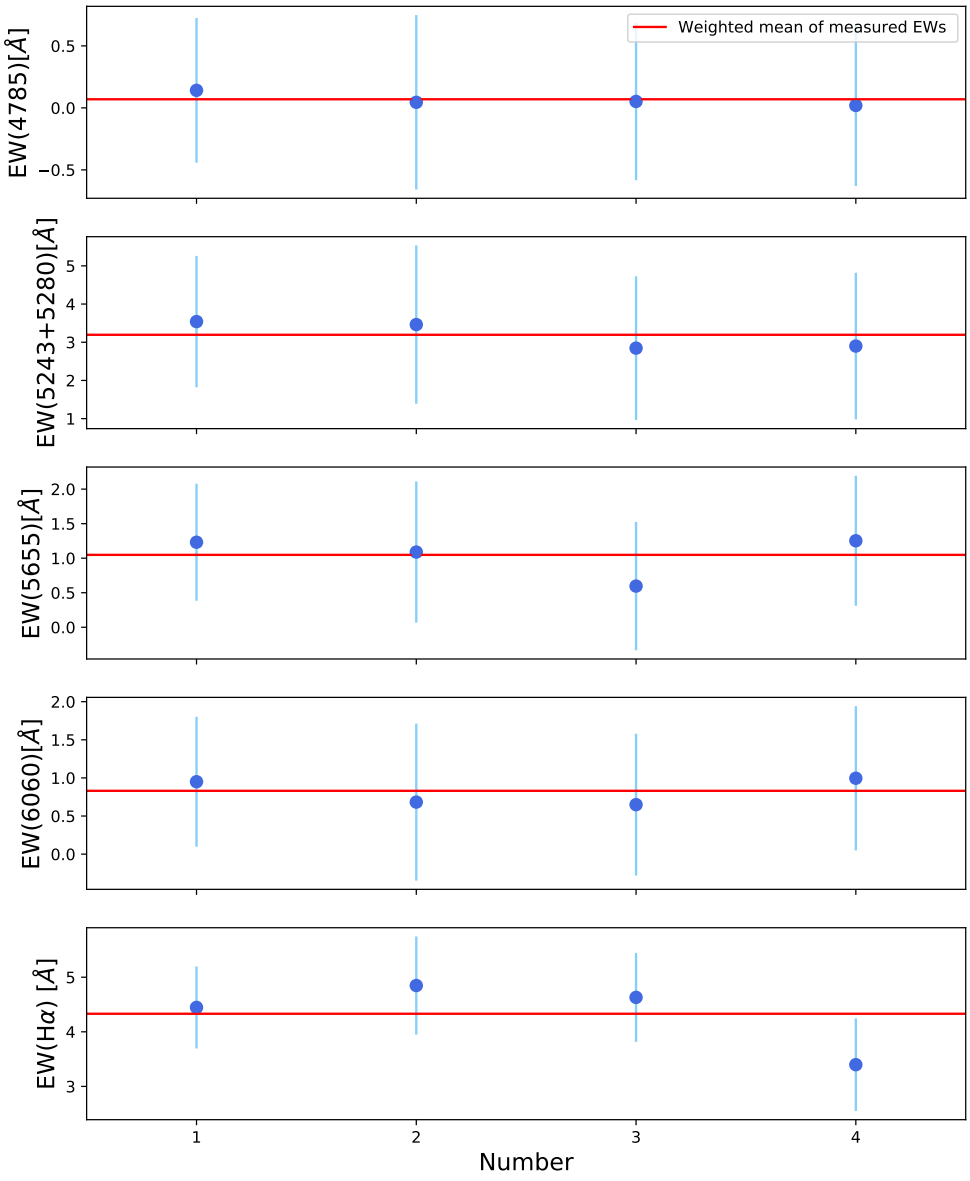

Figure 7.8: EW variations of J0706+6134. Blue dots, light blue lines, and red lines represent the EW, the standard deviation in EW measurements, and the weighted mean of the EW values for the respective line, respectively.

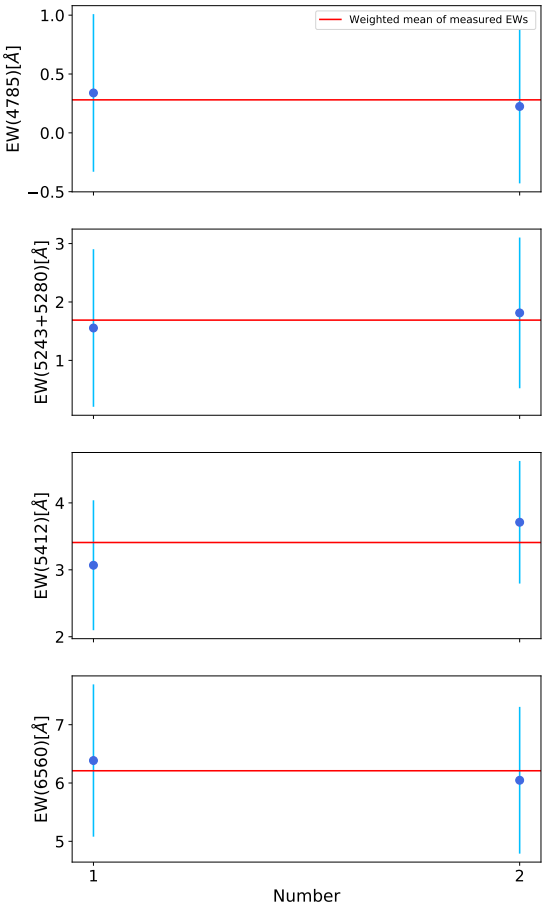

Figure 7.9: EW variations of WD0101-182. Blue dots, light blue lines, and red lines represent the EW, the standard deviation in EW measurements, and the weighted mean of the EW values for the respective line, respectively.

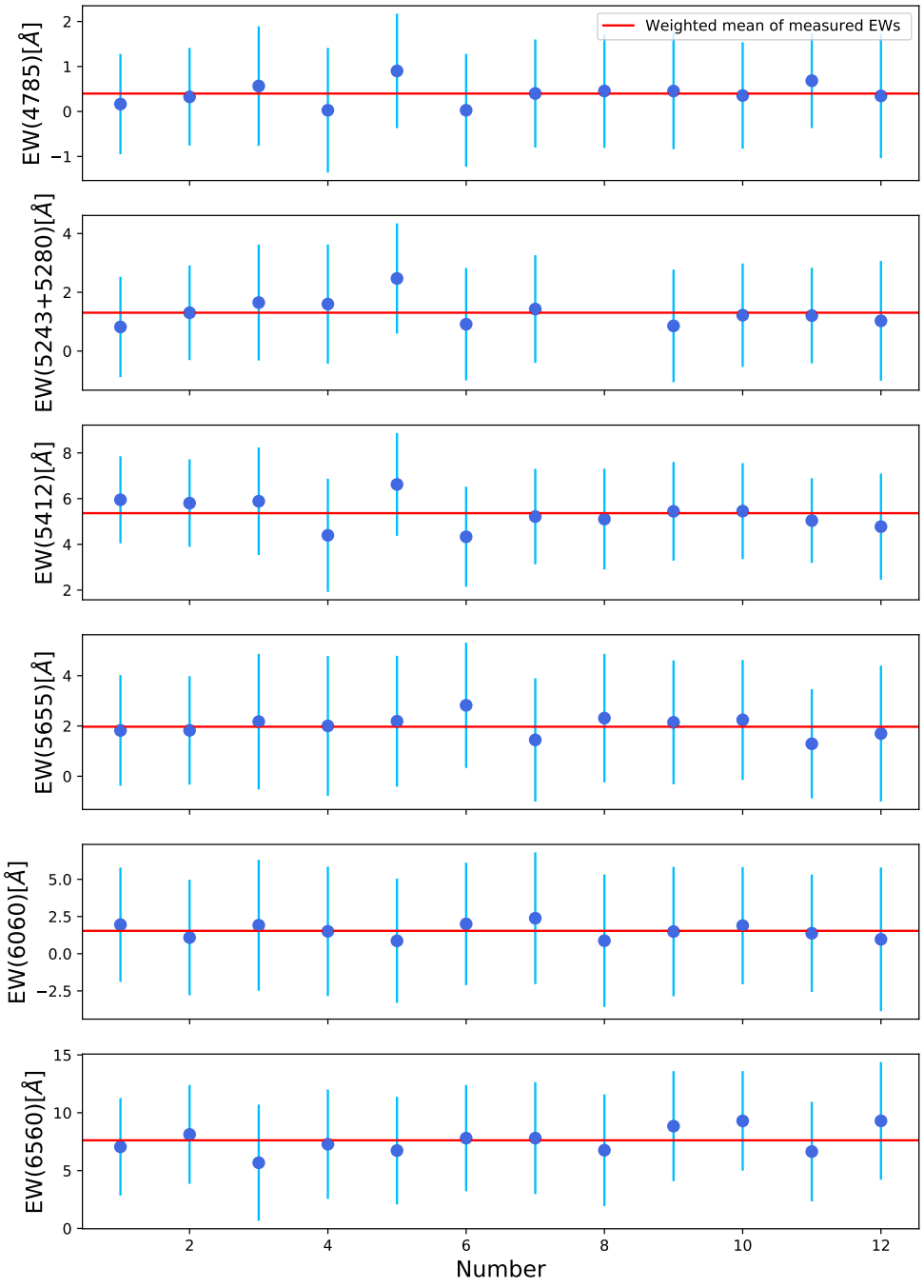

Figure 7.10: EW variations of HS 0742+6520. Blue dots, light blue lines, and red lines represent the EW, the standard deviation in EW measurements, and the weighted mean of the EW values for the respective line, respectively.

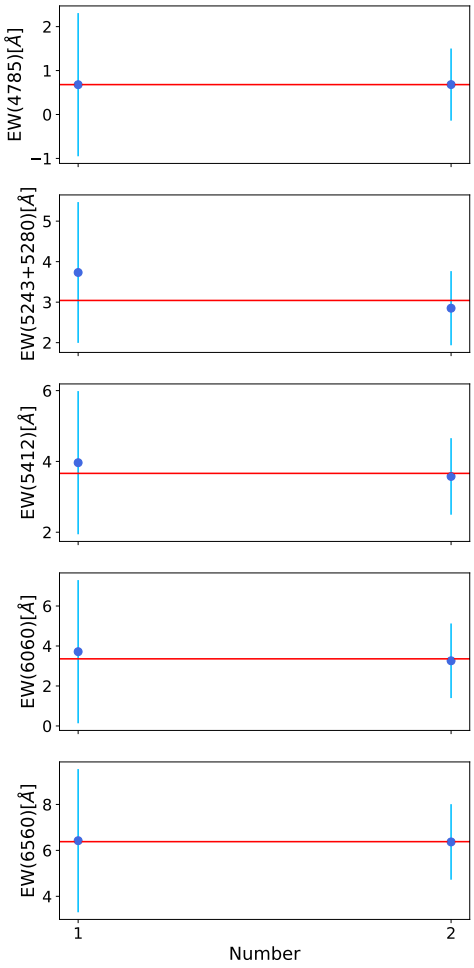

Figure 7.11: EW variations of HE 0504-2408. Blue dots, light blue lines, and red lines represent the EW, the standard deviation in EW measurements, and the weighted mean of the EW values for the respective line, respectively.

8

Radial Velocity Measurements

Stellar spectroscopy provides a mighty analysis method that can confirm stellar multiplicity. By measuring the Doppler shift of a spectral line, the radial velocity (RV) of a star can be determined. If RV changes are observed, then this hints[1] towards binarity. In the case of binarity, almost all spectral lines (other than telluric and interstellar lines) are Doppler shifted in accordance with the star receding from us or coming towards us. This method is commonly utilized in binary star studies as well as finding exoplanets. By fitting a sinusoidal function to the RV curve, the radial velocity semi-amplitude K can be determined. To determine the semi-amplitude, accurately, a homogeneous phase coverage is needed and in particular the maxima and minima of the RV curve should be covered well.

Depending on the visibility of the spectral features of both components, binary stars are categorized as single-lined or double-lined spectroscopic binaries[2]. The mass ratio of a binary star can be calculated only if it is a double-lined spectroscopic binary, since the radial velocity semi-amplitude of the primary and secondary (K_1 and K_2, respectively) can only be determined for this configuration. In our case, none of our stars exhibit spectral features from a secondary, but a freshly born white dwarf can outshine a M dwarf and undoubtedly a sub-stellar companion in the optical band. In fact one of the stars in our sample (HS 0713+3958) was shown to have a companion which was detected with infrared photometry (Napiwotzki, 1997). Later it was revealed with HST/STIS spectroscopy that the companion is a M dwarf (Werner et al., 2018a). However, it has been clarified that this system is not a close binary, since both stars are clearly resolved by Gaia (Reindl et al., 2021).

As mentioned in chapter 5.1.1, the period distribution of our sample is in good agreement with the orbital period distribution of post common envelope binaries, which raises the question whether the photometric variability is caused by close binaries in which case RV variations in the spectra should be detectable. So far only J0146+3236 was examined

[1] Pulsations might also induce RV shifts.

[2] Some binary stars have so small separations that the components can not be resolved visually, yet the spectra exhibit spectral features (e.g. absorption lines) of both stars. These kind of binaries are called double-lined spectroscopic binaries. In some cases, the primary component of the system outshines the secondary and only spectral features of the primary are visible in the spectrum. These are called single-lined spectroscopic binaries.

for RV variations by fitting Voigt profiles (GVPFIT; Bainbridge & Webb, 2017) to the He II lines and no RV shifts larger than 14.2 km/s could be found (Reindl et al., 2019). Moreover, the determination of RVs may also uncover whether the UHE lines originate from a close companion if they shift in antiphase to the He II lines. To test these hypotheses, in this chapter the RV variations of the UHE and He II line problem white dwarfs are explored further.

8.1 Cross-Correlation with *fxcor*

An adequate way of deriving radial velocities is based on fitting a mathematical function to individual lines and measuring the line positions. Then, the shift of the lines reveal RV variations. However, this method has a main drawback that also affects particularly stellar spectra used in this work. Predetermined mathematical functions such as the Gaussian, Lorentzian or Voigt line profiles do not represent UHE lines and too strong He II lines adequately. Therefore, accurately determining the positions of the UHE lines and, hence, the RVs might be affected by the systematic errors. For that reason, in this work RV variations were determined by performing a cross-correlation with *fxcor* (Fitzpatrick, 1993), a radial velocity analysis package in IRAF.

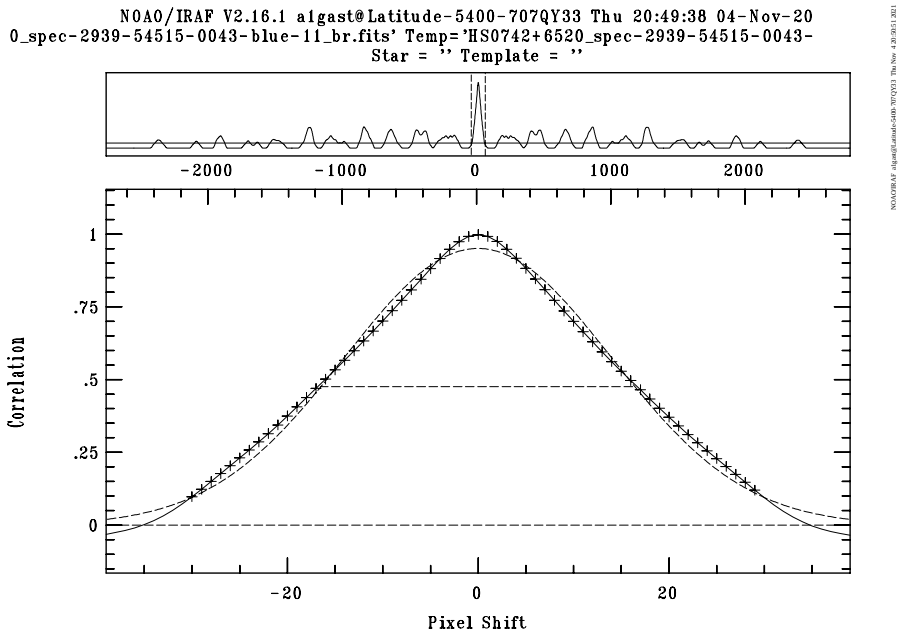

Figure 8.1: An example cross-correlation function generated with IRAF's *fxcor* package. The top panel shows the entire CCF. The bottom panel shows the peak of CCF where a Gaussian (plus symbols) is fitted to the CCF.

fxcor, implementing the method developed by Tonry & Davis (1979), utilizes cross-correlation of a spectrum (mentioned as "object") with a synthetic or an observed spectrum template. As a result the cross-correlation function (CCF) is generated (see Fig. 8.1). To measure relative RVs, shifts between the spectra are determined by fitting a mathematical function to the CCF peak. RV errors are displayed according to the fitted

mathematical function. Care must be taken while choosing cross-correlation regions that inhabit telluric lines or cosmic emissions. These regions must be excluded since they can induce false variations.

By using *fxcor*, the relative RVs and errors of the UHE and He II line problem white dwarfs were determined. Only stars having more than 3 spectra were studied. Each star's chronologically first recorded spectrum was chosen as the template spectrum since most of the spectra do not show significant S/N discrepancies. But in case, the S/N or cosmic contamination of the chosen spectrum did not permit it, the highest S/N spectrum in the individual data set was selected as the template. Before the cross-correlation, the line regions for both the object and the template spectrum were determined (see Fig. 8.2). For the UHE WDs, this step was employed in three different ways; by (*i*) only selecting UHE lines, (*ii*) only selecting He II lines, (*iii*) selecting UHE and He II lines together. Measured relative RVs and errors, are listed in Tables 9.3 and 9.4. Missing RV measurements are due to low quality of the spectra. Also for these objects, the number of UHE lines is not many and some of the lines are really weak so that it is not possible to differentiate between noise and the line. Mainly, the measured RVs lie within the error range for all three measurement types. Furthermore, no significant deviations have been found between RVs measured from UHE lines and RVs measured from He II lines which proves that UHE lines indeed originate from the white dwarf and not from a close companion.

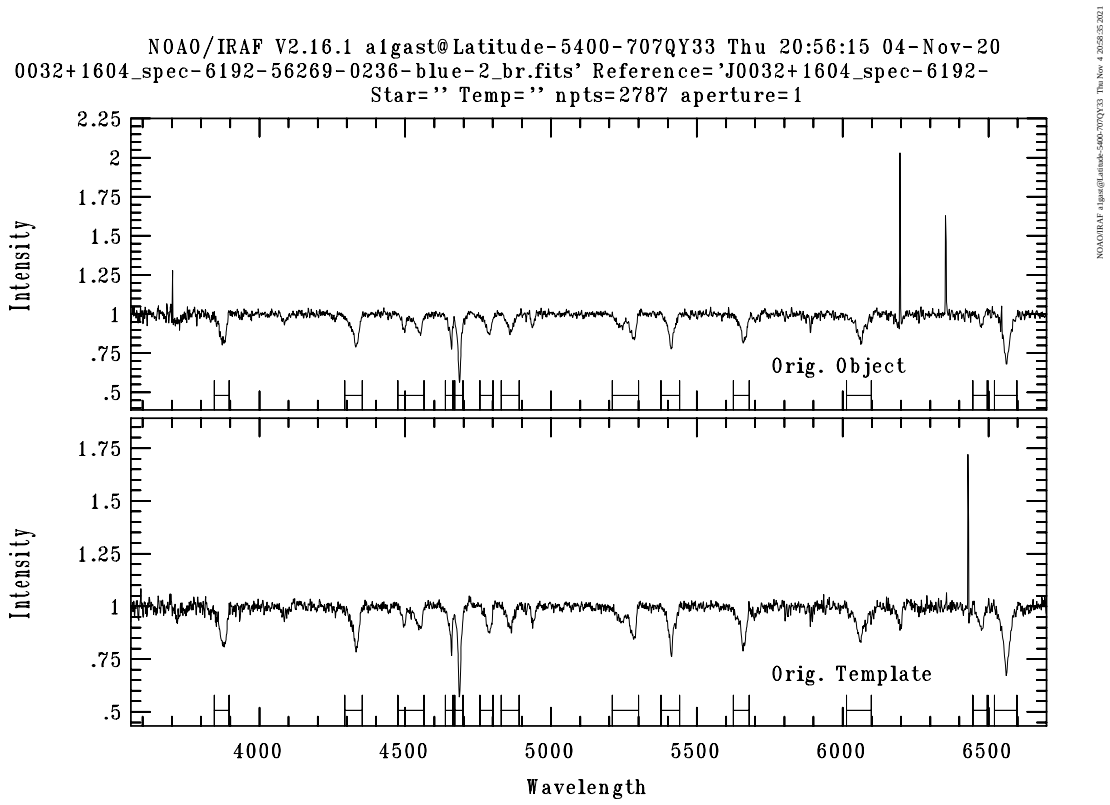

Figure 8.2: An example of region selection to cross-correlate. The top panel shows the object's spectrum and the bottom panel shows the template spectrum. Chosen line regions are displayed in double bars.

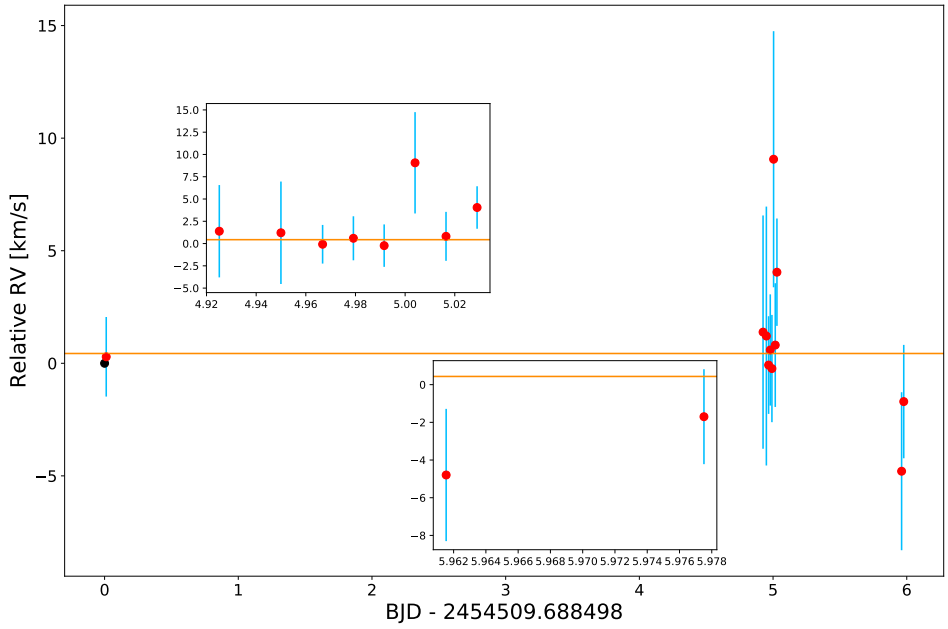

Figure 8.3: RV variation plot of the UHE WD HS 0742+6520 produced by only selecting UHE lines. The black dot represents the RV measurement of the template spectrum and the red dots represent RV measurements of the object spectra. The blue bars and the orange line represent RV errors and the weighted mean of the RV measurements, respectively.

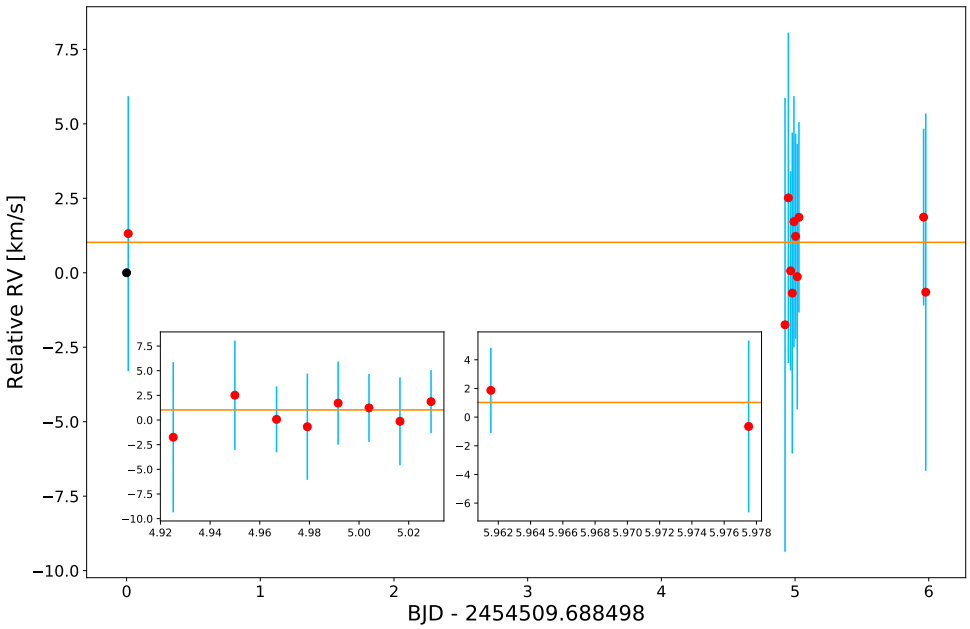

Figure 8.4: RV variation plot of the UHE WD HS 0742+6520 produced by only selecting He II lines.The black dot represents the RV measurement of the template spectrum and the red dots represent RV measurements of the object spectra. The blue bars and the orange line represent RV errors and the weighted mean of the RV measurements, respectively.

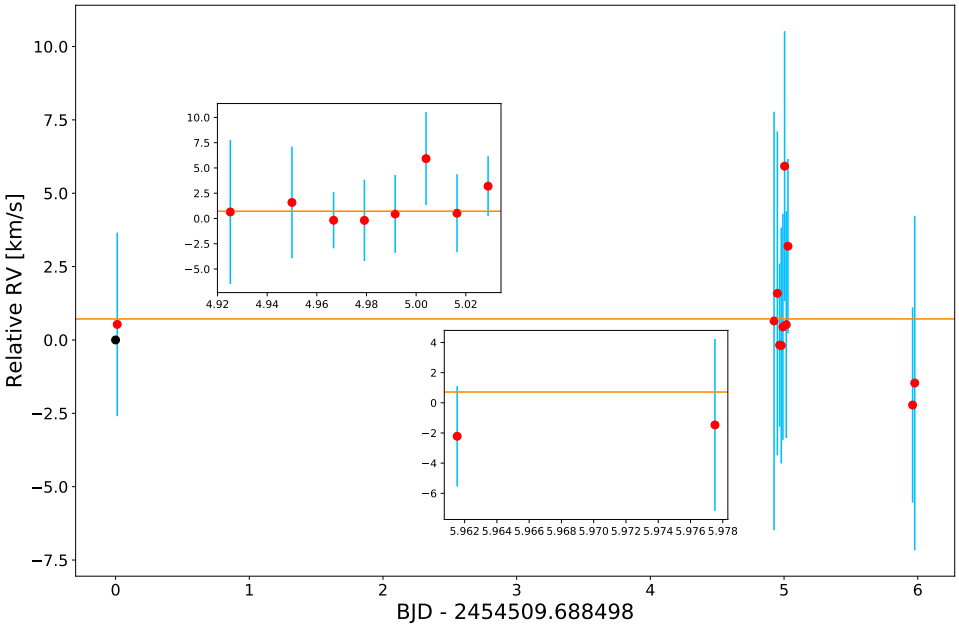

Figure 8.5: RV variation plot of the UHE WD HS 0742+6520 produced by selecting UHE and He II lines together. The black dot represents the RV measurement of the template spectrum and the red dots represent RV measurements of the object spectra. The blue bars and the orange line represent RV errors and the weighted mean of the RV measurements, respectively.

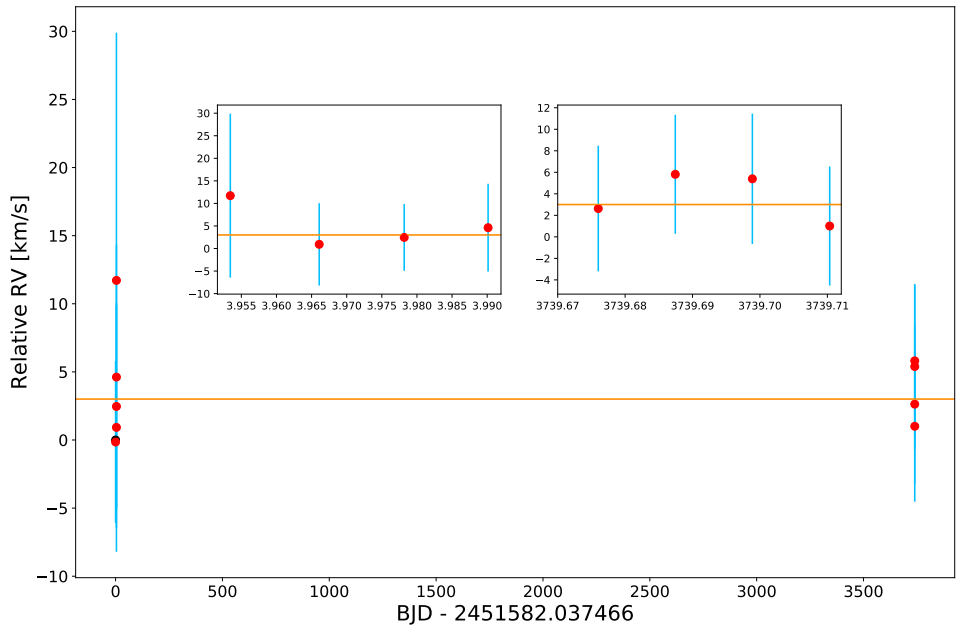

Figure 8.6: RV variation plot of the He II line problem WD HE 1314+0018 produced by selecting He II lines. The black dot represents the RV measurement of the template spectrum and the red dots represent RV measurements of the object spectra. The blue bars and the orange line represent RV errors and the weighted mean of the RV measurements, respectively.

8.2 Statistical Significance of RV Variations

To test the statistical significance of the RV variations, the procedure explained by Maxted et al. (2001) was followed. First, a weighted mean velocity for each star was calculated. Then with the assumption of the calculated mean velocity being constant, the χ^2 was calculated. Here, the χ^2 statistics serves as a test mechanism to confirm how well the calculated weighted mean velocity matches to the RV variations. In addition, for a suitable number of degrees of freedom (N-1, N being number of RV values for each object), the calculated χ^2 values were compared to the χ^2 distribution which permits to calculate the false detection probability (p). Objects with log p < -4, -1.3 > log p > -4.0, and log p > -1.3 are considered as significantly RV variable, candidates for RV variability, and non-detections, respectively. According to the calculated log p values, all of the objects were noted as non-detections and the log p values for each object are listed in Tables 8.1 and 8.2.

8.3 The Upper Limit for the Minimum Companion Mass

The statistical analysis of the RV variations shows that the objects in the sample are not RV variable. However, the RV measurements are not infinitely accurate and the measurement sensitivity in this work is comparable to RV variations only more than a few km/s. Thus, below the presented sensitivity range it would be still possible to encounter sub-stellar companions. Therefore, by using the binary mass function $f(M_{1,2})$,

$$f(M_1, M_2) = \frac{K_{1,2}^3 P}{2\pi G} = \frac{M_{2,1}^3 \sin^3 i}{(M_1 + M_2)^2} \tag{8.1}$$

for each object an upper limit of the minimum companion mass was calculated. Since with separate RV measurements of UHE and He II lines it has been shown that the UHE lines do not stem from a close companion, the objects were considered as single-lined binaries. Consequently, half of the maximum RV shift was selected as maximum radial velocity semi-amplitude of the primary (K_1). The values for the orbital period (P) were selected as photometric periods from Reindl et al. (2021) and for each object an inclination angle (i) of 90°, and a typical white dwarf mass of 0.6 $M_\odot$ was assumed. The maximum RV shifts (ΔRV) and the upper limits for the minimum companion masses for the UHE and He II line problem white dwarfs are listed in Tables 8.1 and 8.2, respectively.

8.4 RV Discussion

As observed in Tables 9.3 and 9.4, the RV errors are high for some of the objects. This might be due to a couple of reasons. First, the cross-correlation technique is more suited for stellar spectra that have many lines which decreases the uncertainty on the measurement (e.g stars with spectral type later than F5V). For these stars, excluding telluric lines in a wider region of the spectra, where many lines are present, is selected in general.

UHE WDs			
Name	Max ΔRV [km/s]	Min Companion Mass [M_{Jup}]	log p
J0146+3236	8.3	9.2	-0.045
HS 0158+2335	5.6	7.7	-0.001
HS 0713+3958	1.6	2.5	-0.005
HS 0742+6520	8.2	-	-0.021
J0032+1604	1.0	1.7	-0.188
J0254+0058	6.7	12.5	-0.008
J0706+6134	2.0	5.0	-0.178
J0900+2343	6.1	-	-0.003
J1059+4043	6.9	14.0	-0.509
J1215+1203	1.1	1.7	-0.049
J1257+4220	10.4	14.3	-0.098
J1510+6106	3.1	-	-0.001

Table 8.1: Maximum ΔRV measured by using UHE + He II lines and the upper limit of minimum companion mass for UHE WDs as well as false detection probability of RV variations. For the objects that are not photometrically variable, the minimum companion mass has not been calculated.

He II Line Problem WDs			
Name	Max ΔRV [km/s]	Min Companion Mass [M_{Jup}]	log p
HE 1314+0018	11.9	17.4	-0.003
J0821+1739	6.7	8.7	-0.190
J0827+5858	1.8	-	-0.269
J0947+1015	23.1	-	-0.023
J1029+2540	4.2	4.9	-0.137
J1512+0651	16.4	18.2	-0.665
J1553+4832	19.6	54.9	-0.721

Table 8.2: Maximum ΔRV and upper limit of minimum companion mass for He II line problem WDs as well as false detection probability of RV variations. For the objects that are not photometrically variable, the minimum companion mass has not been calculated.

However, this is not applicable to our case, since the number of lines is small which might be the first reason for getting large errors compared to shifts. Moreover, broad spectral lines generate a broader CCF that deviates from Gaussian which results in larger RV errors (De Marco et al., 2004). Other mathematical functions within *fxcor* such as *sinc* and *center1d* were also attempted to fit. To test the *sinc* function, the template spectra were cross-correlated with themselves. However, the outcome was RV shifts from 5 to 15 km/s on the contrary to the expected 0 km/s shift. This shows that the RV variations calculated with this function can not be trusted. In addition, the *center1d* function do not give RV errors, therefore this function was also rejected. The low values of the RV shifts and their statistical significance as well as the calculated minimum companion masses imply that companions more massive than brown dwarfs/planets are very unlikely and that the UHE lines originate from the white dwarfs.

Brown dwarf + white dwarf binaries had already been known for a while (Maxted et al., 2006; Burleigh et al., 2006; Casewell et al., 2012; Parsons et al., 2017; Casewell et al., 2018)

and recently exoplanets in close orbits of white dwarfs have been also detected (Gänsicke et al., 2019; Vanderburg et al., 2020). In this work, the calculated minimum companion masses reside within the planet mass range (except for J1553+4832). This raises the question whether it is possible to encounter brown dwarf/exoplanet companions orbiting the objects in our sample.

To date, only 10 (possibly 11) post-common envelope binaries have been confirmed to consist of a white dwarf and a brown dwarf component with orbital periods ranging from 0.048 d to 0.42 d (Casewell et al., 2018, 2020; van Roestel et al., 2021). Moreover, in all of these systems, the sub-stellar companion masses are higher[3] than 50 M_{Jup} which is much larger than the calculated minimum companion masses in our sample. In addition, except one of the aforementioned white dwarf + brown dwarf binaries, all show the signs of an irradiation effect either inferred from the light curves or emission lines in the spectra. The only system that does not show this feature has an orbital period of 9.98 h and the temperature of the white dwarf is 11 500 K (Burleigh et al., 2011). However, this is not surprising for this configuration, since the strength of irradiation effect depends on separation and temperature difference. Even for the largest orbital separations, the irradiation effect should have been encountered in our very hot white dwarf sample.

From the composition of the debris disc and accretion rates, Gänsicke et al. (2019) inferred that a planet with a mass comparable to ice giants is orbiting WD J0914+1914 in 8-10 d. To reach this final orbital configuration and survive the common envelope phase, they argued that the planet's initial mass and separation from the star must have been 1 to 13 M_{Jup} and around 1.5 to 5 AU, respectively. However, none of our objects have periods of more than 2.92 d. The population synthesis studies of precataclysmic variables containing a brown dwarf show that to form such close obits (40 - 63 min) the final companion mass must be $\sim$ 73 M_{Jup} (Nelson et al., 2018). Nonetheless, theoretical predictions show that sub-stellar companions with masses $\sim$ 5 M_{Jup} can a survive common envelope phase given suitable initial conditions (orbital separation, initial mass; Lagos et al., 2021). In fact, Vanderburg et al. (2020) discovered a planet with a mass $\leq$ 14 M_{Jup} transiting a white dwarf every 1.4 d. Even though such objects exist, the frequency that is detected amongst the very hot white dwarfs (UHE sample $\sim$ 10 %) does not match with the occurrence rates of hot Jupiters around white dwarfs ($\leq$ 1.5 %; van Sluijs & Van Eylen, 2018) and white dwarf + brown dwarf binaries (0.5 %; Steele et al., 2011). Therefore, it is unlikely that the white dwarfs in our sample host substellar companions.

[3]Except WD 0837+185b; M $\approx$ 25-30 M_{Jup} (Casewell et al., 2012)

9

Summary & Conclusion

In this work, a photometric and spectroscopic study of UHE and He II line problem white dwarfs is presented. 10 % of all white dwarfs that are on top of the white dwarf cooling sequence show the UHE phenomenon (Reindl et al., 2021). Considering the early stages of white dwarf cooling occurring rapidly, our sample offers a unique playground for the evolutionary studies of the white dwarfs. Furthermore, the improper determination of the stellar parameters (e.g. $T_{\rm eff}$, log g) due to imprecisely fit H/He lines in the UHE and He II line problem white dwarf sample would result in an inadequate evaluation of the mass distribution of white dwarfs (Reindl et al., 2019) which is not only important for stellar astrophysics, but also Galactic studies. Therefore, a better comprehension of these objects is essential.

Considering the fact that the sample's period distribution is consistent with both the orbital period distribution of post-common envelope binaries and the rotational period distribution of magnetic white dwarfs, the two most plausible scenarios as the source of the photometric variability are post-common envelope binaries and weak magnetic fields. For the former scenario increasing amplitudes towards longer wavelengths in the light curves and RV variations in the spectra are expected. For the latter, no significant amplitude variations in the light curves of the different bands and the light curve correlated EW variation of the UHE lines are expected. The data reduction and analysis of the BUSCA light curves presented in this work contributed to the findings of Reindl et al. (2021). Two newly discovered objects (J0702+0514 and J0706+6134) do not show discrepancies in the amplitudes measured in the different bands, which confirms the previous findings.

In this work, EW measurements of the UHE lines were done by integrating the observations. This method was chosen because Voigt profiles only provide a poor fit to the observed line profiles. Reindl et al. (2019) showed that EW variations of UHE lines are correlated to the light curve, but He II lines were shown to be randomly varying. In this work, the EW variations of the UHE lines of J0146+3236 have been confirmed, but, the EW variations of the He II lines found to be constant over the photometric period. The disagreement with the results of Reindl et al. (2019) might be due to utilizing different methods to measure the EWs. For the other objects no significant variations of the the EWs of the UHE or He II lines could be found. Better S/N spectra would be needed to reach a sound conclusion.

For the first time in this work, the RVs of a large sample of UHE and He II line problem white dwarfs have been studied. The statistical significance of RV variations was tested and in accordance, none of the objects in the sample was found to be RV variable. The RV measurements inferred from the He II lines of J0146+3236 obtained with the cross correlation method resulted in smaller errors and confirmed the non-RV variability of the object reported by Reindl et al. (2019) which shows that this method is better suited than utilizing Voigt profiles.

The observed light curve shapes of the sample do not match with (over-)contact binaries and the amplitudes detected from ellipsoidal deformation systems are always smaller than reflection effect systems (see Fig. 4.2). Therefore, the former two binary types can be ruled out. Reflection effect binaries can explain the observed light curve shapes, periods and amplitudes. However, an amplitude increase towards longer wavelengths is not detected in any of the multi-band light curves. In addition, the non-detection of RV variations implies that the photometric variability is most likely not caused by stellar type post-common envelope companions.

The calculated minimum companion masses are comparable to the ones of giant planets and brown dwarfs. However, no signs of the irradiation effect have been encountered in the spectra of our sample, which is a distinguishing characteristic of white dwarfs with brown dwarf companions. Giant planets were discovered closely orbiting white dwarfs and theoretical studies suggest that such planets with a few M_{Jup} masses can survive the common envelope phase. Nevertheless, it is unlikely that the very hot white dwarfs in our sample harbour substellar companions since the occurrence rate of such objects around white dwarfs is expected to be far less than the occurrence rate of the UHE and He II line problem phenomenon.

To reveal the perplexing nature of these objects, further investigations are desirable. In addition to the current RV study, a systematic search for IR excesses will be crucial to dismiss post common envelope binaries as the source of the photometric variability. Moreover, phase resolved high S/N spectra can disclose the correlation between EW variations and light curves for the other objects. Finally, spectro-polarimetric observations can validate the presence of magnetic fields in these stars which would reinforce the magnetosphere model.

Bibliography

Adams, W. S. 1915, PASP, 27, 236

Adams, W. S. 1925, Proceedings of the National Academy of Science, 11, 382

Alam, S., Albareti, F. D., Allende Prieto, C., et al. 2015, ApJS, 219, 12

Althaus, L. G., Córsico, A. H., Isern, J., & García-Berro, E. 2010, A&A Rev., 18, 471

Althaus, L. G., Panei, J. A., Miller Bertolami, M. M., et al. 2009, ApJ, 704, 1605

Babel, J. & Montmerle, T. 1997, A&A, 323, 121

Bainbridge, M. B. & Webb, J. K. 2017, MNRAS, 468, 1639

Bédard, A., Bergeron, P., Brassard, P., & Fontaine, G. 2020, ApJ, 901, 93

Bellinger, E. P., Basu, S., Hekker, S., Christensen-Dalsgaard, J., & Ball, W. H. 2021, ApJ, 915, 100

Bergeron, P., Dufour, P., Fontaine, G., et al. 2019, ApJ, 876, 67

Bern, K. & Wramdemark, S. 1973, Lick Observatory Bulletin, 8, 1

Bloecker, T. 1995, A&A, 299, 755

Bloemen, S., Marsh, T. R., Østensen, R. H., et al. 2011, MNRAS, 410, 1787

Budaj, J. 2011, AJ, 141, 59

Burleigh, M. R., Hogan, E., Dobbie, P. D., Napiwotzki, R., & Maxted, P. F. L. 2006, MNRAS, 373, L55

Burleigh, M. R., Steele, P. R., Dobbie, P. D., et al. 2011, in American Institute of Physics Conference Series, Vol. 1331, Planetary Systems Beyond the Main Sequence, ed. S. Schuh, H. Drechsel, & U. Heber, 262–270

Cantiello, M. & Braithwaite, J. 2011, A&A, 534, A140

Casewell, S. L., Belardi, C., Parsons, S. G., et al. 2020, MNRAS, 497, 3571

Casewell, S. L., Burleigh, M. R., Wynn, G. A., et al. 2012, ApJ, 759, L34

Casewell, S. L., Burleigh, M. R., Wynn, G. A., et al. 2012, 759, L34

Casewell, S. L., Littlefair, S. P., Parsons, S. G., et al. 2018, MNRAS, 481, 5216

Castro, A. I. G. d. 2013, Young Stellar Objects and Protostellar Disks, ed. T. D. Oswalt & M. A. Barstow (Dordrecht: Springer Netherlands), 279–335

Christensen-Dalsgaard, J. 2008

de Boer, K. & Seggewiss, W. 2008, Stars and Stellar Evolution

De Marco, O., Bond, H. E., Harmer, D., & Fleming, A. J. 2004, ApJ, 602, L93

Dekker, H., D'Odorico, S., Kaufer, A., Delabre, B., & Kotzlowski, H. 2000, in Society of Photo-Optical Instrumentation Engineers (SPIE) Conference Series, Vol. 4008, Optical and IR Telescope Instrumentation and Detectors, ed. M. Iye & A. F. Moorwood, 534–545

Dennihy, E., Clemens, J. C., Dunlap, B. H., et al. 2018, ApJ, 854, 40

Dobbie, P. D., Napiwotzki, R., Burleigh, M. R., et al. 2006, MNRAS, 369, 383

Drake, A. J., Graham, M. J., Djorgovski, S. G., et al. 2014, ApJS, 213, 9

Dreizler, S., Heber, U., Napiwotzki, R., & Hagen, H. J. 1995, A&A, 303, L53

Dunlap, B. H. & Clemens, J. C. 2015, in Astronomical Society of the Pacific Conference Series, Vol. 493, 19th European Workshop on White Dwarfs, ed. P. Dufour, P. Bergeron, & G. Fontaine, 547

Eddington, A. S. 1924, Monthly Notices of the Royal Astronomical Society, 84, 308

Eggen, O. J. & Greenstein, J. L. 1965, ApJ, 142, 925

Eggen, O. J. & Greenstein, J. L. 1967, ApJ, 150, 927

Eisenstein, D. J., Liebert, J., Harris, H. C., et al. 2006a, ApJS, 167, 40

Eisenstein, D. J., Liebert, J., Koester, D., et al. 2006b, AJ, 132, 676

Farihi, J., Barstow, M. A., Redfield, S., Dufour, P., & Hambly, N. C. 2010, MNRAS, 404, 2123

Fitzpatrick, M. J. 1993, in Astronomical Society of the Pacific Conference Series, Vol. 52, Astronomical Data Analysis Software and Systems II, ed. R. J. Hanisch, R. J. V. Brissenden, & J. Barnes, 472

Fontaine, G., Brassard, P., & Bergeron, P. 2001, PASP, 113, 409

Gänsicke, B. T., Koester, D., Farihi, J., et al. 2012, MNRAS, 424, 333

Gänsicke, B. T., Koester, D., Girven, J., Marsh, T. R., & Steeghs, D. 2010, Science, 327, 188

Gänsicke, B. T., Schreiber, M. R., Toloza, O., et al. 2019, Nature, 576, 61

Geier, S., Kupfer, T., Heber, U., et al. 2015, in Astronomical Society of the Pacific Conference Series, Vol. 493, 19th European Workshop on White Dwarfs, ed. P. Dufour, P. Bergeron, & G. Fontaine, 475

Geier, S., Nesslinger, S., Heber, U., et al. 2007, A&A, 464, 299

Geier, S., Nesslinger, S., Heber, U., et al. 2008, A&A, 477, L13

Gentile Fusillo, N. P., Tremblay, P. E., Cukanovaite, E., et al. 2021, MNRAS, 508, 3877

Goodwin, S. 2013, Star Formation, ed. T. D. Oswalt & M. A. Barstow (Dordrecht: Springer Netherlands), 243–277

Green, R. F. 1980, ApJ, 238, 685

Greenstein, J. L. 1966, ApJ, 144, 496

Greenstein, J. L. & Sargent, A. I. 1974, ApJS, 28, 157

Hagen, H. J., Engels, D., Groote, D., & Reimers, D. 1994, in Astronomy from Wide-Field Imaging, ed. H. T. MacGillivray, Vol. 161, 729

Hartman, J. D. & Bakos, G. Á. 2016, Astronomy and Computing, 17, 1

Hermes, J. J., Kawaler, S. D., Bischoff-Kim, A., et al. 2017, 835, 277

Herwig, F. 2013, Evolution of Solar and Intermediate-Mass Stars, ed. T. D. Oswalt & M. A. Barstow (Dordrecht: Springer Netherlands), 397–445

Hollands, M. A., Koester, D., Alekseev, V., Herbert, E. L., & Gänsicke, B. T. 2017, MNRAS, 467, 4970

Hügelmeyer, S. D., Dreizler, S., Homeier, D., et al. 2006, A&A, 454, 617

Jura, M. & Young, E. D. 2014, Annual Review of Earth and Planetary Sciences, 42, 45

Kepler, S. O., Koester, D., & Ourique, G. 2016, Science, 352, 67

Kepler, S. O., Koester, D., Pelisoli, I., Romero, A. D., & Ourique, G. 2021, MNRAS, 507, 4646

Kleinman, S. J., Kepler, S. O., Koester, D., et al. 2013, ApJS, 204, 5

Koester, D. 2009, A&A, 498, 517

Koester, D. 2013, White Dwarf Stars, ed. T. D. Oswalt & M. A. Barstow (Dordrecht: Springer Netherlands), 559–612

Koester, D., Kepler, S. O., & Irwin, A. W. 2020, A&A, 635, A103

Koester, D., Weidemann, V., & Zeidler, E. M. 1982, A&A, 116, 147

Krtička, J., Huang, L., Jagelka, M., et al. 2018, Contributions of the Astronomical Observatory Skalnate Pleso, 48, 170

Krtička, J., Kawka, A., Mikulášek, Z., et al. 2020, A&A, 639, A8

Krtička, J. & Kubát, J. 2005, in Astronomical Society of the Pacific Conference Series, Vol. 334, 14th European Workshop on White Dwarfs, ed. D. Koester & S. Moehler, 337

Lagos, F., Schreiber, M. R., Zorotovic, M., et al. 2021, MNRAS, 501, 676

Larson, S., Beshore, E., Hill, R., et al. 2003, in AAS/Division for Planetary Sciences Meeting Abstracts, Vol. 35, AAS/Division for Planetary Sciences Meeting Abstracts #35, 36.04

Liebert, J., Dahn, C. C., & Monet, D. G. 1988, ApJ, 332, 891

Madej, J., Należyty, M., & Althaus, L. G. 2004, A&A, 419, L5

Manser, C. J., Gänsicke, B. T., Koester, D., Marsh, T. R., & Southworth, J. 2016, MNRAS, 462, 1461

Masci, F. J., Laher, R. R., Rusholme, B., et al. 2019, PASP, 131, 018003

Maxted, P. F. L., Heber, U., Marsh, T. R., & North, R. C. 2001, MNRAS, 326, 1391

Maxted, P. F. L., Napiwotzki, R., Dobbie, P. D., & Burleigh, M. R. 2006, Nature, 442, 543

Morton, D. C. 1991, ApJS, 77, 119

Munoz, M. S., Wade, G. A., Nazé, Y., et al. 2020, MNRAS, 492, 1199

Napiwotzki, R. 1993, Acta Astron., 43, 343

Napiwotzki, R. 1997, in The Third Conference on Faint Blue Stars, ed. A. G. D. Philip, J. Liebert, R. Saffer, & D. S. Hayes, Vol. 207

Napiwotzki, R., Christlieb, N., Drechsel, H., et al. 2001, Astronomische Nachrichten, 322, 411

Nelson, L., Schwab, J., Ristic, M., & Rappaport, S. 2018, ApJ, 866, 88

Owocki, S. P., ud-Doula, A., Sundqvist, J. O., et al. 2016, MNRAS, 462, 3830

Parsons, S. G., Gänsicke, B. T., Marsh, T. R., et al. 2017, MNRAS, 470, 4473

Perlmutter, S., Aldering, G., della Valle, M., et al. 1998, Nature, 391, 51

Petit, V., Cohen, D. H., Nazé, Y., et al. 2014, in Magnetic Fields throughout Stellar Evolution, ed. P. Petit, M. Jardine, & H. C. Spruit, Vol. 302, 330–333

Petit, V., Owocki, S. P., Wade, G. A., et al. 2013, MNRAS, 429, 398

Reif, K., Bagschik, K., de Boer, K. S., et al. 1999, in Society of Photo-Optical Instrumentation Engineers (SPIE) Conference Series, Vol. 3649, Sensors, Cameras, and Systems for Scientific/Industrial Applications, ed. M. M. Blouke & G. M. Williams, 109–120

Reindl, N., Bainbridge, M., Przybilla, N., et al. 2019, MNRAS, 482, L93

Reindl, N., Rauch, T., Werner, K., et al. 2014, A&A, 572, A117

Reindl, N., Schaffenroth, V., Filiz, S., et al. 2021, A&A, 647, A184

Ricker, G. R., Winn, J. N., Vanderspek, R., et al. 2015, Journal of Astronomical Telescopes, Instruments, and Systems, 1, 014003

Sandage, A. 1969, ApJ, 158, 1115

Sandage, A. & Luyten, W. J. 1967, ApJ, 148, 767

Schaffenroth, V., Geier, S., Heber, U., et al. 2018, A&A, 614, A77

Schaller, G., Schaerer, D., Meynet, G., & Maeder, A. 1992, A&AS, 96, 269

Sikora, J., David-Uraz, A., Chowdhury, S., et al. 2019, MNRAS, 487, 4695

Sion, E. M. 2011, Hot White Dwarfs, ed. D. W. Hoard, 1–24

Sion, E. M., Greenstein, J. L., Landstreet, J. D., et al. 1983, ApJ, 269, 253

Sion, E. M. & Liebert, J. 1977, ApJ, 213, 468

Smee, S. A., Gunn, J. E., Uomoto, A., et al. 2013, AJ, 146, 32

Steele, P. R., Burleigh, M. R., Dobbie, P. D., et al. 2011, MNRAS, 416, 2768

Strittmatter, P. A. & Wickramasinghe, D. T. 1971, MNRAS, 152, 47

Sundqvist, J. O., ud-Doula, A., Owocki, S. P., et al. 2012, MNRAS, 423, L21

Tonry, J. & Davis, M. 1979, AJ, 84, 1511

Tonry, J. L., Denneau, L., Heinze, A. N., et al. 2018, PASP, 130, 064505

Townsend, R. H. D. & Owocki, S. P. 2005, MNRAS, 357, 251

ud Doula, A. & Nazé, Y. 2016, Advances in Space Research, 58, 680, x-ray Emission from Hot Stars and their Winds

ud Doula, A. & Owocki, S. P. 2002, 576, 413

Ud-Doula, A., Owocki, S. P., & Townsend, R. H. D. 2008, Monthly Notices of the Royal Astronomical Society, 385, 97

ud-Doula, A., Townsend, R. H. D., & Owocki, S. P. 2006, ApJ, 640, L191

Unglaub, K. & Bues, I. 2000, A&A, 359, 1042

van Roestel, J., Kupfer, T., Bell, K. J., et al. 2021, ApJ, 919, L26

van Sluijs, L. & Van Eylen, V. 2018, MNRAS, 474, 4603

Vanderburg, A., Rappaport, S. A., Xu, S., et al. 2020, Nature, 585, 363

Vauclair, G., Vauclair, S., & Greenstein, J. L. 1979, A&A, 80, 79

Vollmann, K. & Eversberg, T. 2006, Astronomische Nachrichten, 327, 862

Wade, G. A., Alecian, E., Bohlender, D. A., et al. 2011, in Active OB Stars: Structure, Evolution, Mass Loss, and Critical Limits, ed. C. Neiner, G. Wade, G. Meynet, & G. Peters, Vol. 272, 118–123

Wade, G. A., Barbá, R. H., Grunhut, J., et al. 2015, Monthly Notices of the Royal Astronomical Society, 447, 2551

Wade, G. A., Maíz Apellániz, J., Martins, F., et al. 2012, MNRAS, 425, 1278

Weinberg, D. H., Mortonson, M. J., Eisenstein, D. J., et al. 2013, Phys. Rep., 530, 87

Wendell, O. C. 1898, Proceedings of the American Academy of Arts and Sciences, 33, 520

Werner, K. 1996, ApJ, 457, L39

Werner, K., Bagschik, K., Rauch, T., & Napiwotzki, R. 1997, A&A, 327, 721

Werner, K., Dreizler, S., Heber, U., et al. 1995, A&A, 293, L75

Werner, K. & Herwig, F. 2006, PASP, 118, 183

Werner, K. & Rauch, T. 2015, A&A, 584, A19

Werner, K., Rauch, T., & Kepler, S. O. 2014, A&A, 564, A53

Werner, K., Rauch, T., & Kruk, J. W. 2018a, A&A, 609, A107

Werner, K., Rauch, T., & Kruk, J. W. 2018b, A&A, 616, A73

Werner, K., Rauch, T., Napiwotzki, R., et al. 2004, A&A, 424, 657

Werner, K., Rauch, T., & Reindl, N. 2019, MNRAS, 483, 5291

Williams, K. A., Kepler, S. O., & Sion, E. M. 2019, Research Notes of the American Astronomical Society, 3, 109

Wilson, R. E. 1990, ApJ, 356, 613

Wilson, R. E. & Vaccaro, T. R. 1997, MNRAS, 291, 54

Wisotzki, L. 1994, in Astronomy from Wide-Field Imaging, ed. H. T. MacGillivray, Vol. 161, 723

Yakut, K., Kalomeni, B., & İbanoğlu, C. 2004, A&A, 417, 725

Zechmeister, M. & Kürster, M. 2009, A&A, 496, 577

Appendix A: Tables

Table 9.1: Spectroscopic observations of UHE white dwarfs with Barycentric Julian Day at mid-exposure, exposure time, and S/N. SDSS spectra consist of a blue and a red part and their respective S/N values are given as B and R.

Name	Dataset	Spectrograph	BJD	Exposure Time (s)	S/N (B, R)
J0032+1604	spec-6192-56269-0236 - 0	SDSS	2456269.548819	900	52, 22
J0032+1604	spec-6192-56269-0236 - 1	SDSS	2456269.560174	900	55, 23
J0032+1604	spec-6192-56269-0236 - 2	SDSS	2456269.571551	900	51, 21
WD0101-182	2000-08-05T09:37:50.147	UVES	2451761.908621	600	84
WD0101-182	2002-09-26T09:22:02.533	UVES	2452543.899842	600	81
J0146+3236	141031-1-0057	TWIN	2456962.363262	1200	68, 64
J0146+3236	141031-2-0060	TWIN	2456962.407462	1200	70, 70
J0146+3236	141031-3-0068	TWIN	2456962.484013	1200	71, 78
J0146+3236	141031-4-0072	TWIN	2456962.526293	1200	58, 60
J0146+3236	141031-5-0079	TWIN	2456962.603423	1200	55, 63
J0146+3236	141101-1-0029	TWIN	2456963.375873	1200	30, 28
J0146+3236	141101-2-0035	TWIN	2456963.429785	1200	54, 53
J0146+3236	141101-3-0039	TWIN	2456963.474252	1200	49, 51
J0146+3236	141101-4-0045	TWIN	2456963.553939	1200	49, 50
J0146+3236	141102-1-0032	TWIN	2456964.336921	1200	50, 41
J0146+3236	141102-2-0040	TWIN	2456964.441735	1200	54, 55
J0146+3236	141102-3-0046	TWIN	2456964.504384	1200	45, 47
J0146+3236	141102-4-0052	TWIN	2456964.575889	1200	40, 46
J0146+3236	141102-5-0056	TWIN	2456964.633341	1200	68, 64
HS 0158+2335	141031-1-0074	TWIN	2456962.550015	1800	37, 38
HS 0158+2335	141101-1-0043	TWIN	2456963.523563	1800	-, 24
HS 0158+2335	141102-1-0048	TWIN	2456964.527861	600	24, -
HS 0158+2335	150107-3-0027	TWIN	2457030.287209	1800	32, 37
HS 0158+2335	150107-4-0031	TWIN	2457030.336625	1800	27, 32
HS 0158+2335	150107-5-0035	TWIN	2457030.390682	1800	32, 35
HS 0158+2335	150107-6-0039	TWIN	2457030.438965	1800	31, 33
HS 0158+2335	150107-7-0043	TWIN	2457030.495128	1800	23, 22
HS 0158+2335	150108-8-0003	TWIN	2457031.278736	1800	39, 39
HS 0158+2335	150108-9-0007	TWIN	2457031.357815	1800	36, 39
HS 0158+2335	150108-10-0011	TWIN	2457031.411189	1800	33, 35
HS 0158+2335	150108-11-0015	TWIN	2457031.461416	1800	21, 20
HS 0158+2335	spec-5114-55883-0700 - 0	SDSS	2455869.832384	900	21, 10
HS 0158+2335	spec-5114-55883-0700 - 1	SDSS	2455869.843773	900	23, 12
HS 0158+2335	spec-5114-55883-0700 - 2	SDSS	2455869.855162	900	22, 11
HS 0158+2335	spec-5114-55883-0700 - 3	SDSS	2455869.866528	900	25, 12

Continued on next page

Table 9.1 – continued from previous page

Name	Dataset	Spectrograph	BJD	Exposure Time (s)	S/N (B, R)
HS 0158+2335	spec-5114-55883-0700 - 4	SDSS	2455883.701771	900	28, 14
HS 0158+2335	spec-5114-55883-0700 - 5	SDSS	2455883.713137	900	28, 13
HS 0158+2335	spec-5114-55883-0700 - 6	SDSS	2455883.724549	900	30, 14
HS 0158+2335	spec-5114-55883-0700 - 7	SDSS	2455883.735914	900	29, 14
J0254+0058	spec-0708-52175-0448 - 0	SDSS	2452173.989210	912	13, 7
J0254+0058	spec-0708-52175-0448 - 1	SDSS	2452174.942978	1211	15, 7
J0254+0058	spec-0708-52175-0448 - 2	SDSS	2452175.897891	1215	11, 6
J0254+0058	spec-0708-52175-0448 - 3	SDSS	2452175.913680	1210	14, 7
J0254+0058	spec-0708-52175-0448 - 4	SDSS	2452175.929381	1212	17, 8
J0254+0058	spec-0708-52175-0448 - 5	SDSS	2452175.945066	1211	17, 8
J0254+0058	spec-0708-52175-0448 - 6	SDSS	2452175.960902	1218	18, 9
J0254+0058	spec-4242-55476-0674 - 0	SDSS	2455458.971956	900	19, 8
J0254+0058	spec-4242-55476-0674 - 1	SDSS	2455475.836053	900	15, 6
J0254+0058	spec-4242-55476-0674 - 2	SDSS	2455475.870162	900	15, 6
J0254+0058	spec-4242-55476-0674 - 3	SDSS	2455475.883194	900	17, 6
J0254+0058	spec-4242-55476-0674 - 4	SDSS	2455475.89456	900	16, 7
J0254+0058	spec-4242-55476-0674 - 5	SDSS	2455475.905926	900	16, 7
J0254+0058	spec-4242-55476-0674 - 6	SDSS	2455476.866655	900	21, 8
J0254+0058	spec-4242-55476-0674 - 7	SDSS	2455476.878021	900	21, 8
J0254+0058	spec-4242-55476-0674 - 8	SDSS	2455476.889387	900	21, 8
HE 0504-2408	2001-12-17T04:33:10.032	UVES	2452260.695397	480	38
HE 0504-2408	2002-02-22T01:07:01.663	UVES	2452327.550633	600	73
HS 0713+3958	spec-3655-55240-0518 - 0	SDSS	2455240.641076	900	22, 7
HS 0713+3958	spec-3655-55240-0518 - 1	SDSS	2455240.652674	901	23, 8
HS 0713+3958	spec-3655-55240-0518 - 2	SDSS	2455240.664294	901	23, 9
HS 0713+3958	spec-3655-55240-0518 - 3	SDSS	2455240.676563	900	25, 9
HS 0713+3958	spec-3655-55240-0518 - 4	SDSS	2455240.688171	900	24, 10
HS 0713+3958	141031-1-0081	TWIN	2456962.623635	1800	51, 52
HS 0713+3958	141031-2-0087	TWIN	2456962.689323	1500	46, 43
HS 0713+3958	141101-1-0051	TWIN	2456963.636721	1800	32, 32
HS 0713+3958	150107-4-0033	TWIN	2457030.368869	1500	30, 32
HS 0713+3958	150107-5-0041	TWIN	2457030.473557	1500	34, 32
HS 0713+3958	150107-6-0049	TWIN	2457030.569285	1500	35, 36
HS 0713+3958	150107-7-0055	TWIN	2457030.634088	1500	38, 38
HS 0713+3958	150108-8-0009	TWIN	2457031.390972	1500	43, 41
HS 0713+3958	150108-9-0017	TWIN	2457031.492430	1500	39, 47
HS 0713+3958	150108-10-0023	TWIN	2457031.557974	1500	39, -
HS 0713+3958	150108-11-0029	TWIN	2457031.635299	1500	33, 33
HS 0727+6003	141031-1-0085	TWIN	2456962.659589	1800	62, 55
HS 0727+6003	141031-2-0089	TWIN	2456962.712694	1500	74, 67
HS 0727+6003	150107-3-0029	TWIN	2457030.317287	1200	40, 35
HS 0727+6003	150107-4-0037	TWIN	2457030.421524	1200	42, 39
HS 0727+6003	150107-5-0045	TWIN	2457030.529844	1200	40, 43
HS 0727+6003	150107-6-0053	TWIN	2457030.613270	1200	42, 46
HS 0727+6003	150108-7-0005	TWIN	2457031.311890	1200	50, 50
HS 0727+6003	150108-8-0013	TWIN	2457031.462618	1200	44, 43
HS 0727+6003	150108-9-0019	TWIN	2457031.515130	1200	45, 44
HS 0727+6003	150108-10-0027	TWIN	2457031.615800	1200	44, 42

Continued on next page

Table 9.1 – continued from previous page

Name	Dataset	Spectrograph	BJD	Exposure Time (s)	S/N (B, R)
HS 0742+6520	spec-2939-54515-0043 - 0	SDSS	2454509.688498	929	36, 21
HS 0742+6520	spec-2939-54515-0043 - 1	SDSS	2454509.700822	929	37, 21
HS 0742+6520	spec-2939-54515-0043 - 2	SDSS	2454514.613650	929	30, 18
HS 0742+6520	spec-2939-54515-0043 - 3	SDSS	2454514.638474	929	29, 19
HS 0742+6520	spec-2939-54515-0043 - 4	SDSS	2454514.655262	928	31, 19
HS 0742+6520	spec-2939-54515-0043 - 5	SDSS	2454514.667664	929	32, 19
HS 0742+6520	spec-2939-54515-0043 - 6	SDSS	2454514.680059	929	33, 18
HS 0742+6520	spec-2939-54515-0043 - 7	SDSS	2454514.692501	929	32, 18
HS 0742+6520	spec-2939-54515-0043 - 8	SDSS	2454514.704973	928	32, 19
HS 0742+6520	spec-2939-54515-0043 - 9	SDSS	2454514.717491	929	34, 21
HS 0742+6520	spec-2939-54515-0043 - 10	SDSS	2454515.650036	1228	38, 21
HS 0742+6520	spec-2939-54515-0043 - 11	SDSS	2454515.666014	1228	30, 17
J0900+2343	spec-2086-53401-0242 - 0	SDSS	2453401.791963	927	6, 3
J0900+2343	spec-2086-53401-0242 - 1	SDSS	2453401.807887	1239	7, 3
J0900+2343	spec-2086-53401-0242 - 2	SDSS	2453401.821641	1049	6, 3
J0900+2343	spec-5776-56010-0610 - 0	SDSS	2456010.599074	900	13, 4
J0900+2343	spec-5776-56010-0610 - 1	SDSS	2456010.610463	900	13, 4
J0900+2343	spec-5776-56010-0610 - 2	SDSS	2456010.621829	900	13, 4
J1059+4043	spec-4624-55654-0162 - 0	SDSS	2455654.608495	900	14, 4
J1059+4043	spec-4624-55654-0162 - 1	SDSS	2455654.619884	900	14, 5
J1059+4043	spec-4624-55654-0162 - 2	SDSS	2455654.631250	900	14, 5
J1215+1203	spec-1612-53149-0045 - 0	SDSS	2453149.657157	927	10, 4
J1215+1203	spec-1612-53149-0045 - 1	SDSS	2453149.669467	927	10, 4
J1215+1203	spec-1612-53149-0045 - 2	SDSS	2453149.681761	926	10, 4
J1257+4220	spec-4703-55617-0946 - 0	SDSS	2455617.890000	900	18, 8
J1257+4220	spec-4703-55617-0946 - 1	SDSS	2455617.901366	900	19, 8
J1257+4220	spec-4703-55617-0946 - 2	SDSS	2455617.912731	900	18, 8
J1257+4220	spec-4703-55617-0946 - 3	SDSS	2455617.924097	900	18, 8
J1257+4220	spec-4703-55617-0946 - 4	SDSS	2455617.935475	900	18, 7
J1510+6106	spec-0611-52055-0070 - 0	SDSS	2452055.821474	911	16, 8
J1510+6106	spec-0611-52055-0070 - 1	SDSS	2452055.843082	1211	20, 10
J1510+6106	spec-0611-52055-0070 - 2	SDSS	2452055.862502	1530	20, 10
WDJ0706+6134	r1555360	IDS	2459261.592637	900	95
WDJ0706+6134	r1555362	IDS	2459261.603910	900	79
WDJ0706+6134	r1555364	IDS	2459261.615147	900	87
WDJ0706+6134	r1555717	IDS	2459263.458669	1100	85
WDJ0702+0514	r1555358	IDS	2459261.545338	1800	7
WDJ0702+0514	r1555724	IDS	2459263.557762	1800	56

Table 9.2: Spectroscopic observations of He II line problem white dwarfs with Barycentric Julian Day at mid-exposure, exposure time, and S/N. SDSS spectra consist of a blue and a red part and their respective S/N values are given as B and R.

Name	Dataset	Spectrograph	BJD	Exposure Time (s)	S/N (B, R)
J0821+1739	spec-4491-55570-0358 - 0	SDSS	2455570.763484	900	8, 3
J0821+1739	spec-4491-55570-0358 - 1	SDSS	2455570.774861	900	8, 3

Continued on next page

Table 9.2 – continued from previous page

Name	Dataset	Spectrograph	BJD	Exposure Time (s)	S/N (B, R)
J0821+1739	spec-4491-55570-0358 - 2	SDSS	2455570.786227	900	8, 3
J0821+1739	spec-4491-55570-0358 - 3	SDSS	2455570.797604	900	9, 3
J0821+1739	spec-4491-55570-0358 - 4	SDSS	2455570.809005	900	8, 3
J0827+5858	spec-1873-54437-0608 - 0	SDSS	2454437.894950	934	16, 11
J0827+5858	spec-1873-54437-0608 - 1	SDSS	2454437.923092	929	17, 11
J0827+5858	spec-1873-54437-0608 - 2	SDSS	2454437.939208	1237	22, 12
J0947+1015	spec-5321-55945-0412 - 0	SDSS	2455945.792813	900	13, 5
J0947+1015	spec-5321-55945-0412 - 1	SDSS	2455945.804294	900	12, 5
J0947+1015	spec-5321-55945-0412 - 2	SDSS	2455945.815671	900	11, 4
J0947+1015	spec-5321-55945-0412 - 3	SDSS	2455945.827130	900	11, 4
J0947+1015	spec-5321-55945-0412 - 4	SDSS	2455945.838495	900	11, 4
J0947+1015	spec-5321-55945-0412 - 5	SDSS	2455945.849861	900	11, 4
J0947+1015	spec-5319-55953-0828 - 0	SDSS	2455953.806863	900	16, 5
J0947+1015	spec-5319-55953-0828 - 1	SDSS	2455953.818229	900	15, 5
J0947+1015	spec-5319-55953-0828 - 2	SDSS	2455953.829606	900	15, 5
J1029+2540	spec-6464-56309-0798 - 0	SDSS	2456309.873275	902	26, 11
J1029+2540	spec-6464-56309-0798 - 1	SDSS	2456309.884653	900	27, 11
J1029+2540	spec-6464-56309-0798 - 2	SDSS	2456309.896030	900	29, 11
J1029+2540	spec-6464-56309-0798 - 3	SDSS	2456309.907396	900	28, 12
J1029+2540	spec-2349-53734-0523 - 0	SDSS	2453732.032494	1592	40, 7
J1029+2540	spec-2349-53734-0523 - 1	SDSS	2453734.036064	926	28, 9
J1029+2540	spec-2349-53734-0523 - 2	SDSS	2453734.884301	925	32, 10
J1029+2540	spec-2349-53734-0523 - 3	SDSS	2453734.898608	1110	33, 10
HE 1314+0018	150107-1-0057	TWIN	2457030.654021	1200	42, 32
HE 1314+0018	150107-2-0061	TWIN	2457030.693933	1200	40, 32
HE 1314+0018	150107-3-0065	TWIN	2457030.732004	1200	42, 42
HE 1314+0018	150108-4-0031	TWIN	2457031.653404	1200	33, 39
HE 1314+0018	150108-5-0035	TWIN	2457031.689623	1200	36, 44
HE 1314+0018	150108-6-0039	TWIN	2457031.725413	1200	43, 45
HE 1314+0018	spec-0295-51585-0632 - 0	SDSS	2451582.037466	900	32, 15
HE 1314+0018	spec-0295-51585-0632 - 1	SDSS	2451582.049649	900	23, 10
HE 1314+0018	spec-0295-51585-0632 - 2	SDSS	2451585.990893	900	27, 12
HE 1314+0018	spec-0295-51585-0632 - 3	SDSS	2451586.003553	900	25, 13
HE 1314+0018	spec-0295-51585-0632 - 4	SDSS	2451586.015655	900	28, 12
HE 1314+0018	spec-0295-51585-0632 - 5	SDSS	2451586.027597	900	26, 12
HE 1314+0018	spec-4004-55321-0198 - 0	SDSS	2455321.713484	900	44, 25
HE 1314+0018	spec-4004-55321-0198 - 1	SDSS	2455321.724907	900	41, 23
HE 1314+0018	spec-4004-55321-0198 - 2	SDSS	2455321.736343	900	42, 24
HE 1314+0018	spec-4004-55321-0198 - 3	SDSS	2455321.747813	900	41, 24
J1512+0651	spec-4878-55710-0648 - 0	SDSS	2455710.732743	900	22, 9
J1512+0651	spec-4878-55710-0648 - 1	SDSS	2455710.744109	900	22, 8
J1512+0651	spec-4878-55710-0648 - 2	SDSS	2455710.755475	900	20, 8
J1512+0651	spec-4878-55710-0648 - 3	SDSS	2455710.766840	900	22, 9
J1512+0651	spec-4878-55710-0648 - 4	SDSS	2455710.778206	900	22, 10
J1512+0651	spec-4878-55710-0648 - 5	SDSS	2455710.789572	900	22, 9
J1512+0651	spec-2902-54629-0302 - 0	SDSS	2454627.737271	1229	19, 10
J1512+0651	spec-2902-54629-0302 - 1	SDSS	2454627.753129	1228	17, 9
J1512+0651	spec-2902-54629-0302 - 2	SDSS	2454628.751172	1528	21, 10

Continued on next page

Table 9.2 – continued from previous page

Name	Dataset	Spectrograph	BJD	Exposure Time (s)	S/N (B, R)
J1512+0651	spec-2902-54629-0302 - 3	SDSS	2454628.770594	1528	18, 9
J1512+0651	spec-2902-54629-0302 - 4	SDSS	2454628.793837	1836	21, 10
J1512+0651	spec-2902-54629-0302 - 5	SDSS	2454629.748037	1528	20, 10
J1512+0651	spec-2724-54616-0315 - 0	SDSS	2454611.846246	1528	20, 10
J1512+0651	spec-2724-54616-0315 - 1	SDSS	2454616.727324	1637	25, 9
J1553+4832	spec-0812-52352-0187 - 0	SDSS	2452352.911961	1229	8, 4
J1553+4832	spec-0812-52352-0187 - 1	SDSS	2452352.926886	916	7, 4
J1553+4832	spec-0812-52352-0187 - 2	SDSS	2452352.939059	912	6, 3
J1553+4832	spec-6730-56425-0756 - 0	SDSS	2456421.928588	900	12, 4
J1553+4832	spec-6730-56425-0756 - 1	SDSS	2456421.939965	900	11, 4
J1553+4832	spec-6730-56425-0756 - 2	SDSS	2456421.951331	900	11, 3
J1553+4832	spec-6730-56425-0756 - 3	SDSS	2456425.925116	900	11, 3

Table 9.3: Measured relative RVs and errors for each UHE WD.

Name	UHE + He II lines [km/s]	UHE lines [km/s]	He II lines [km/s]
J0146+3236	-7.1 ± 4.9	-9.5 ± 5.8	2.1 ± 2.2
	-1.7 ± 1.9	-3.0 ± 1.7	3.4 ± 2.6
	-0.4 ± 2.3	-1.4 ± 1.7	3.9 ± 3.1
	-4.4 ± 5.3	-6.9 ± 5.6	5.6 ± 3.8
	-5.2 ± 3.1	-6.8 ± 2.8	0.9 ± 2.5
	-0.2 ± 2.6	-0.8 ± 2.5	2.1 ± 2.7
	-2.2 ± 3.4	-3.3 ± 3.2	1.7 ± 3.0
	-2.9 ± 4.2	-5.0 ± 2.3	5.1 ± 3.0
	-1.6 ± 2.3	-3.0 ± 1.6	3.9 ± 3.4
	1.2 ± 5.6	-0.1 ± 5.3	6.3 ± 4.2
	-2.7 ± 2.3	-5.2 ± 1.3	6.8 ± 4.3
	-6.4 ± 5.7	-7.7 ± 6.5	-2.1 ± 2.1
HS 0158+2335	-2.3 ± 13.2	-	-1.1 ± 15.1
	-3.4 ± 10.4	-	-3.6 ± 11.8
	-1.1 ± 3.8	-	-1.8 ± 4.0
	2.0 ± 7.7	-	3.8 ± 8.9
	-3.7 ± 11.3	-	-3.2 ± 13.9
	0.2 ± 11.2	-	-0.7 ± 12.
	-0.0 ± 9.7	-	0.7 ± 10.8
HS 0713+3958	1.1 ± 4.5	1.1 ± 2.6	0.1 ± 5.9
	0.0 ± 6.3	0.5 ± 4.6	-0.7 ± 6.0
	-0.4 ± 5.8	-2.1 ± 8.6	2.8 ± 4.2
	-0.5 ± 4.0	-1.1 ± 5.1	0.8 ± 2.5
HS 0742+6520	0.5 ± 3.1	0.3 ± 1.8	1.3 ± 4.6
	0.6 ± 7.1	1.4 ± 5.2	-1.7 ± 7.6
	1.6 ± 5.5	1.2 ± 5.8	2.5 ± 5.5
	-0.2 ± 2.8	-0.1 ± 2.2	0.1 ± 3.3
	-0.2 ± 4.0	0.6 ± 2.5	-0.7 ± 5.4
	0.4 ± 3.9	-0.2 ± 2.4	1.7 ± 4.2
	5.9 ± 4.6	9.1 ± 5.7	1.2 ± 3.4
	0.5 ± 3.9	0.8 ± 2.7	-0.1 ± 4.5

Continued on next page

Table 9.3 – continued from previous page

Name	UHE + He II lines [km/s]	UHE lines [km/s]	He II lines [km/s]
	3.2 ± 3.0	4.0 ± 2.4	1.9 ± 3.2
	-2.2 ± 3.3	-4.8 ± 3.5	1.9 ± 3.0
	-1.5 ± 5.7	-1.7 ± 2.5	-0.7 ± 6.0
J0032+1604	1.0 ± 1.7	0.6 ± 1.9	2.0 ± 1.2
	0.2 ± 3.1	1.0 ± 2.9	-1.4 ± 2.0
J0254+0058	-3.7 ± 8.0	0.3 ± 6.7	-8.2 ± 7.2
	-0.9 ± 5.9	2.9 ± 4.6	-6.3 ± 6.4
	-3.0 ± 6.2	0.5 ± 3.4	-7.2 ± 7.0
	2.4 ± 5.3	6.7 ± 3.9	-4.5 ± 5.3
	1.1 ± 5.7	3.1 ± 3.1	-1.8 ± 5.4
	2.5 ± 5.6	5.2 ± 3.1	-1.6 ± 6.1
	2.3 ± 6.5	3.1 ± 3.8	1.0 ± 7.9
	3.0 ± 6.0	6.1 ± 5.2	-1.8 ± 4.1
J0706+6134	0.1 ± 2.0	1.5 ± 1.3	-1.5 ± 2.8
	0.4 ± 2.2	3.0 ± 1.4	-2.6 ± 2.7
	-1.6 ± 2.7	0.7 ± 0.9	-4.3 ± 4.1
J0900+2343	-1.6 ± 21.8	-	4.1 ± 25.6
	-5.7 ± 13.1	-	-0.7 ± 12.0
	-1.4 ± 14.6	-	-0.1 ± 11.5
	-4.3 ± 7.5	-	-4.5 ± 6.5
	0.4 ± 13.6	-	-2.2 ± 8.8
J1059+4043	6.9 ± 10.0	11.9 ± 10.0	-2.9 ± 6.3
	0.9 ± 5.7	2.6 ± 8.1	-2.6 ± 6.3
J1215+1203	0.8 ± 11.8	-	-1.3 ± 2.9
	-0.3 ± 15.0	-	0.1 ± 7.1
J1257+4220	10.4 ± 9.5	-	11.5 ± 10.6
	9.8 ± 6.7	-	6.3 ± 6.3
	7.1 ± 8.1	-	8.5 ± 6.5
	0.5 ± 11.7	-	-0.5 ± 13.1
J1510+6106	-3.1 ± 9.4	-	-
	-3.1 ± 8.3	-	-

Table 9.4: Measured relative RVs and errors for each He II line problem WD.

Name	RV [km/s]	RV Error [km/s]
HE 1314+0018	-0.1	5.9
	11.7	18.2
	0.9	9.1
	2.5	7.4
	4.6	9.7
	2.6	5.8
	5.8	5.5
	5.4	6.1
	1.0	5.5
J0821+1739	6.7	13.1

Continued on next page

Table 9.4 – continued from previous page

Name	RV [km/s]	RV Error [km/s]
	1.5	19.8
J0827+5858	-1.0	3.9
	0.8	4.5
J0947+1015	1.8	11.0
	-6.6	9.3
	-8.7	24.3
	4.8	18.3
	-18.3	23.5
	-17.0	17.9
	-8.7	19.1
	-12.0	20.3
J1029+2540	4.2	4.9
	0.7	4.7
	3.0	5.2
J1512+0651	1.4	4.2
	-2.7	2.7
	0.1	5.9
	3.0	3.3
	10.6	11.2
	-2.5	5.5
	-5.9	3.5
	-1.1	6.5
	-2.1	5.1
	1.2	3.7
	1.3	3.3
	5.2	2.6
J1553+4832	-1.8	22.2
	0.2	10.9
	-11.1	4.8
	8.4	12.8
	8.5	12.8
	1.9	11.1

Acknowledgements

Joining the Stellar Astrophysics Group in Potsdam was one of the best things that ever happened to me. I'm extremely grateful to my thesis supervisor Prof. Dr. Dr. Stephan Geier for giving me the opportunity to be a part of this group and aiding me throughout my studies. I can not begin to express my gratitude to my immediate supervisor Dr. Nicole Reindl, who never wavered in her unparalleled support and guidance during my best and worst times alike. The completion of my thesis would not have been possible without her. Besides their unprecedented academic support, both of my supervisors broadened my horizons with their admirable view of life and I'll be always thankful for that. A sincere thanks should also go to Dr. Veronika Schaffenroth who always had time to answer my questions with a sincere smile. I'd like to acknowledge the assistance of Tilaksingh Pawar and Matti Dorsch for saving me from IRAF and Python nightmares. Many thanks to my office mates Harry Dawson and Max Pritzkuleit for making the last month of thesis writing more fun. I also wish to thank Mrs. Andrea Brockhaus without whom bureaucratic problems would have been impossible to solve. I had a great pleasure working with all current and former members of our group and I would like to thank each one of you for inspiring me.

Finally, I'm indebted to all my family members and friends who made the roughest times bearable with their presence. Without their unconditional love and support, I couldn't have found the courage to get up every time I fell. Thank you all for making this journey unforgettable!

Statement of Originality

This is to certify that to the best of my knowledge this thesis is a product of my own work and contains no materials previously published, unless where due acknowledgement is made.

Date and Place: November 15, 2021; Potsdam.

Signature: